INTERNAL FLOWS AND FORCE MATRICES IN AXIAL FLOW INDUCERS

Thesis by
Abhijit Bhattacharyya

In Partial Fulfillment of the Requirements
for the Degree of
Doctor of Philosophy

California Institute of Technology
Pasadena, California
1994

(Submitted January 11, 1994)

INTERNAL FLOWS AND FORCE MATRICES IN AXIAL FLOW INDUCERS

Abhijit Bhattacharyya
Division of Engineering and Applied Sciences

1994

Report No. E249.18

To my wife, Lalita Bandyopadhyay

and

my parents , Jatish and Anubha Bhattacharyya

ACKNOWLEDGEMENTS

I would like to express my deepest gratitude and sincere thanks to my advisor, Professor Allan Acosta and to Professor Christopher Brennen for their guidance, encouragement and support throughout my graduate study and the dissertation process. They were available whenever I needed technical assistance and provided me with valuable comments and suggestions throughout the research. I would like to thank Professor Thomas Caughey for his technical insights throughout this work. I would also to thank the other members of my committee, Dr. Richard Murray and Dr. G. Ravichandran for their helpful suggestions.

My colleagues and friends in the laboratory deserve special thanks for providing assistance during the research. In particular, I would like to thank Ron Franz, Adiel Guinzburg, Joe Sivo and Asif Khalak. I would like to express my appreciation and thanks to Cecilia Lin for her assistance with the graphics and her encouragement; and to Jackie Beard and Dana Young for help in the administrative processes.

My thanks go to Marty Gould, Mike Gerfen, Louis Grimaldi and Rodney Rojas for their assistance in the fabrication of some of the components used for the research.

My deepest thanks and gratitude to Lalita (my wife) for her unconditional love and encouragement which has been a source of great strength, confidence and inspiration for me. I would like to thank her for staying up and assisting me during those long hours of dissertation writing. I thank Lalita for rekindling my spirits and for providing reassurance during difficult moments. I would also like to thank my parents and sister in India for their continuous encouragement and support.

Finally I would like to thank NASA George C. Marshall Space Flight Center for sponsoring the current work under grant NAG8-118.

ABSTRACT

Axial flow pump runners known as inducers are subject to complex internal flows and fluid-induced lateral and rotordynamic forces. The internal flows in inducers are three dimensional and are characterized by complicated secondary flows. The current research investigates the boundary layer flows on the blades, hub and housing of unshrouded and shrouded axial flow inducers using flow visualization techniques. Rotordynamic and lateral force data on unshrouded inducers were also obtained under varying conditions of flow and whirl.

Studies on the internal flows showed that the blade boundary layer flow had strong radial components at off-design conditions. The flow remains attached to the blade surface of unshrouded inducers at all flow coefficients tested. The origin of the upstream swirling backflow was found to be at the discharge plane of the inducer. In addition, flow reversal was observed at the suction side blade tip near the leading edge in a shrouded inducer. Re-entry of the hub boundary layer flow (a downstream backflow) into the blade passage area was observed at flow coefficients below design. For unshrouded inducers the radially outward flow near the blade tip mixed with the tip clearance leakage flow to form the upstream backflow. These observations provide a better understanding of the internal flows and the occurrence of upstream backflows in inducers.

The rotordynamic forces acting on an inducer due to an imposed whirl motion was also investigated. It was found that the rotordynamic force data at various whirl frequency ratios does not allow a normal quadratic fit;

consequently the conventional inertial, stiffness and damping coefficients cannot be obtained and a definite whirl ratio describing the instability region does not result. Rotordynamic forces were found to be significantly dependent on the flow coefficient. At flow coefficients below design, these forces are characterized by multiple zero crossings at various whirl frequencies and large destabilizing peaks. Theoretical estimates of the tangential rotordynamic force on a non-whirling inducer using actuator disk theory were significantly different, both in magnitude and direction, from the experimentally measured forces.

The effect of upstream and downstream flow distortions on the rotordynamic and lateral forces on an inducer were studied. It was found that at flow coefficients below design, large lateral forces occurred in the presence of a downstream asymmetry. The reverse flows occurring downstream which consist of high energy fluid are the possible cause of these large forces. The imposition of a uniform downstream condition reduced these forces to near zero values. Results of inlet distortion experiments show that a strong inlet shear causes a significant increase in the lateral force. However, weak inlet shear flows and the flow asymmetry due to a 180° upstream bend did not cause a significant lateral force. It was found that flow distortions upstream or downstream did not cause any significant effect on the rotordynamic forces. Cavitation was found to have important consequences for fluid-induced rotordynamic forces. These forces become destabilizing for both forward and reverse whirl. The magnitudes of the destabilizing forces were found to increase with decreasing cavitation numbers.

TABLE OF CONTENTS

ACKNOWLEDGEMENTS iv
ABSTRACT v
TABLE OF CONTENTS vii
LIST OF FIGURES x
LIST OF TABLES xviii
NOMENCLATURE xix

1. INTRODUCTION 1
  1.1 Statement of the problem 2
  1.2 Inducers and their applications 4
  1.3 Rotor whirl and force matrices 5
  1.4 Literature review 8
    1.4.1 Actuator disk force prediction models 14
    1.4.1a. Turbine blade tip and seal clearance forces 15
    1.4.1b. Forces in axial flow compressors 21
  1.5 Objectives of the research 26

2. EXPERIMENTAL APPARATUS 36
  2.1 The Rotor Force Test Facility 36
    2.1.1 The rotating dynamometer and its calibration 38
    2.1.2 Data acquisition and reduction 40
  2.2 Inducers used for the current research 42
    2.2.1 The 9° unshrouded inducer 43
    2.2.2 The 12° unshrouded inducer 43
    2.2.3 The 12° shrouded inducer 44
  2.3 Flow visualization techniques 44
    2.3.1 Tufts 45
    2.3.2 Paint dot technique 46

2.4 Flow distortion devices 47
    2.4.1 Honeycomb sections 47
    2.4.2 Screens 48
    2.4.3 Upstream bend 49
2.5 Experimental parameters 49

3. INTERNAL FLOWS IN AXIAL FLOW INDUCERS 64
3.1 Unshrouded inducers 64
    3.1.1 Flow on blade surfaces 65
    3.1.2 Flow on hub 67
    3.1.3 Flow on the stationary housing 67
3.2 Shrouded inducer 70
    3.2.1 Flow on the blade surfaces and the hub 71
    3.2.2 Flow on the stationary housing 72

4. EXPERIMENTAL DATA FOR INDUCER ROTORDYNAMIC FORCES 87
4.1 Rotordynamic force data 87
4.2 Steady (lateral) force data 91

5. FLOW DISTORTION EFFECTS 103
5.1 Effect of a downstream asymmetry 103
    5.1.1 Effect of a uniform downstream screen 104
    5.1.1a Lateral forces 104
    5.1.1b Rotordynamic forces 105
5.2 Effect of upstream flow asymmetries 105
    5.2.1 Inlet shear due to honeycomb sections 105
    5.2.2 Inlet shear due to screens 106
    5.2.3 Effect of an upstream bend 108

6. CAVITATION EFFECTS ON INDUCER FORCES 119

6.1 Cavitation performance of inducer VII 120

6.2 Steady forces due to cavitation 120

6.3 Rotordynamic forces due to cavitation 121

9. CONCLUSIONS 137

REFERENCES 140

APPENDIX A 146

APPENDIX B 153

APPENDIX C 159

LIST OF FIGURES

Figure 1.1 Forces acting on a whirling impeller.

Figure 1.2 Internal flow in the blade passage area as postulated by Lakshminarayana (1972).

Figure 1.3 The head flow coefficient of a 9^{o} inducer with and without honeycomb sections at the inlet (from Del Valle et al. 1990).

Figure 1.4 Actuator disk analysis of turbine flow and blade angles (from Martinez-Sanchez and Jaroux 1992).

Figure 1.5 Alford coefficient as a function of whirl frequency ratio ($\alpha_2=70^{o}$, $\beta_2=60^{o}$, solidity=0.756, $\varepsilon/H=0.0113$, ϕ(design)=0.58; from Martinez-Sanchez and Jaroux 1992).

Figure 1.6 Non-dimensionalized normal and tangential forces on a turbine for static offsets of the rotor at $\phi=0.58$ (from Martinez-Sanchez and Jaroux 1992).

Figure 1.7 Actuator disk analysis of flow in axial flow compressors and blade angles (from Colding-Jorgensen 1992).

Figure 1.8a The variation of the cross-coupled stiffness coefficient with flow coefficient (from Colding-Jorgensen 1992).

Figure 1.8b The Alford constant as a function of flow coefficient (from Colding-Jorgensen 1992).

Figure 2.1 Schematic of the Rotor Force Test Facility (RFTF).

Figure 2.2 Inducer installation in the RFTF for force measurements.

Figure 2.3 Downstream discharge asymmetry in the system.

Figure 2.4 Inducer installation for flow visualization experiments.

Figure 2.5a Dry run data showing the dry weight of inducer VII as verification of dynamometer calibration.

Figure 2.5b Angle at which the dry weight of the inducer is recorded.

Figure 2.6 Plot of the non-dimensionalized normal force on inducer VII for a dry run at 3000 rpm, $\varepsilon = 0.0254$ cm.

Figure 2.7 Performance characteristics of the 9^o inducer at 2000 rpm.

Figure 2.8 Performance curves for the 12^o inducers at 2000 rpm.

Figure 2.9a Drawing of inducer IX

Figure 2.9b Photographs showing the machining of inducer IX and the indexing head.

Figure 2.10 Geometry of the honeycomb sections used for the flow distortion experiments.

Figure 2.11a Screen SC1 used for the flow distortion experiments.

Figure 2.11b Screen SC2 used for the flow distortion experiments.

Figure 2.12 The inlet shear flow assembly showing the location of the screen (SC1 or SC2) along with a wire mesh and a uniform honeycomb section.

Figure 2.13 Schematic of the facility with the upstream bend installed.

Figure 3.1 The limiting streamline angle (χ).

Figure 3.2 Photograph showing the paint traces on the suction side of inducer IX at $\phi = 0.041$.

Figure 3.3 Photograph showing the paint traces on the pressure side of inducer IX at $\phi = 0.041$.

Figure 3.4 Photograph showing the paint traces due to downstream re-entry flow on the hub of inducer IX at $\phi = 0.041$.

Figure 3.5 Sketch showing leakage flow, interior of the stationary housing.

Figure 3.6 Photograph of the paint traces showing flow reversal on the housing of inducer VII at a flow coefficient of $\phi = 0.07$ (i.e., with incipient upstream backflow).

Figure 3.7 Photograph of the paint traces showing flow reversal on the suction side blade surface of the shrouded inducer at a flow coefficient of $\phi = 0.041$.

Figure 3.8a Flow traces on the interior of the rotating shroud of the shrouded interior at $\phi = 0.041$.

Figure 3.8b Sketch showing the flow directions for figure 3.8a.

Figure 3.9 Flow on the pressure side of the shrouded inducer at $\phi = 0.041$.

Figure 3.10 Downstream hub re-entry flow in the shrouded inducer at $\phi = 0.041$.

Figure 3.11 The leakage flow on the interior of the stationary housing of the shrouded inducer at $\phi = 0.041$.

Figure 4.1 Non-dimensionalized normal force on inducer VII at various whirl frequency ratios (2000 rpm; $\phi = 0.074$ and $\phi = 0.059$).

Figure 4.2a Non-dimensionalized tangential force on inducer VII at various whirl frequency ratios (2000 rpm; $\phi = 0.074$ and $\phi = 0.059$).

Figure 4.2b Non-dimensionalized tangential force data for inducer VII for a typical repeat run at $\phi = 0.059$ and 2000 rpm.

Figure 4.3 Non-dimensionalized normal force on inducer VII at 2000 rpm; $\phi = 0.037$, $\phi = 0.015$ and $\phi = 0.0$.

Figure 4.4 Non-dimensionalized tangential force on inducer VII at 2000 rpm; $\phi = 0.037$, $\phi = 0.015$ and $\phi = 0.0$.

Figure 4.5 Non-dimensionalized normal force on inducer VII at 3000 rpm; $\phi = 0.074$ and $\phi = 0.059$.

Figure 4.6 Non-dimensionalized tangential force on inducer VII at 3000 rpm; $\phi = 0.074$ and $\phi = 0.059$.

Figure 4.7a Comparison of non-dimensionalized normal force on inducer VII at $\phi = 0.074$ for different rotational speeds.

Figure 4.7b Comparison of non-dimensionalized tangential force on inducer VII at $\phi = 0.074$ for different rotational speeds.

Figure 4.8a Non-dimensionalized lateral force on inducer VII at 2000 rpm; $\phi = 0.074$ and $\phi = 0.059$.

Figure 4.8b Angle of the lateral force shown in figure 4.7a.

Figure 4.9a Non-dimensionalized lateral force on inducer VII at 2000 rpm; $\phi = 0.037$, $\phi = 0.015$ and $\phi = 0.0$.

Figure 4.9b Angle of the lateral force shown in figure 4.8a.

Figure 4.10a Non-dimensionalized lateral force on inducer VII at 2000 rpm; and $\phi = 0.074$ at various locations on the whirl orbit (zero whirl frequency).

Figure 4.10b Angle of the lateral force shown in figure 4.9a.

Figure 5.1a The non-dimensionalized lateral force as a function of flow coefficient in the presence of the downstream asymmetry.

Figure 5.1b Angle of the lateral force shown in figure 5.1a.

Figure 5.2 Performance characteristics of inducer VII due to the downstream screen.
Figure 5.3a Effect of the downstream screen on the non-dimensionalized lateral force on inducer IX.
Figure 5.3b Angle of the lateral force shown in figure 5.3a.
Figure 5.4a Effect of the downstream screen on the non-dimensionalized normal force on inducer VII at 2000 rpm.
Figure 5.4b Effect of the downstream screen on the non-dimensionalized tangential force on inducer VII at 2000 rpm.
Figure 5.5 Axial velocity profile created by the honeycomb sections.
Figure 5.6 Axial velocity profile (upstream) without inlet distortions.
Figure 5.7 Non-dimensionalized lateral force on inducer VII at various rotational speeds and $\phi = 0.041$.
Figure 5.8 Axial velocity profile created by the screens SC1 and SC2.
Figure 5.9a The effect of the inlet distortion screens SC1 and SC2 on the non-dimensionalized lateral force on inducer VII ($\phi = 0.041$).
Figure 5.9b Angle of the lateral force shown in figure 5.9a.
Figure 5.10a The effect of the inlet distortion screens SC1 and SC2 on the non-dimensionalized normal force on inducer VII ($\phi = 0.041$).
Figure 5.10b The effect of the inlet distortion screens SC1 and SC2 on the non-dimensionalized tangential force on inducer VII ($\phi = 0.041$).

Figure 5.11 Axial and swirl velocity profiles created by the upstream bend.

Figure 5.12a Non-dimensionalized lateral force on inducer VII due to the upstream bend (2000 rpm).

Figure 5.12b Angle of the lateral force shown in figure 5.12a.

Figure 6.1 Cavitation performance of inducer VII at 3000 rpm (ϕ = 0.074, and ϕ = 0.049).

Figure 6.2a Non-dimensionalized lateral force on inducer VII at 3000 rpm at various whirl ratios and cavitation numbers (ϕ = 0.074).

Figure 6.2b Angle of the lateral force shown in figure 6.2a.

Figure 6.3a Non-dimensionalized lateral force on inducer VII at 3000 rpm at various whirl ratios and cavitation numbers (ϕ = 0.049).

Figure 6.3b Angle of the lateral force shown in figure 6.3a.

Figure 6.4 Non-dimensionalized tangential force on inducer VII at 3000 rpm at various whirl ratios and cavitation numbers (ϕ = 0.074).

Figure 6.5 Non-dimensionalized tangential force on inducer VII at 3000 rpm at various whirl ratios and cavitation numbers (ϕ = 0.049).

Figure 6.6 Comparison of the non-dimensionalized tangential force on inducer VII at 3000 rpm for the flow coefficients ϕ = 0.074 and ϕ = 0.049 at a cavitation number σ = 0.106.

Figure 6.7 Comparison of the non-dimensionalized tangential force on inducer VII at 3000 rpm for the flow coefficients $\phi = 0.074$ and $\phi = 0.049$ at a cavitation number $\sigma = 0.098$.

Figure 6.8 Non-dimensionalized normal force on inducer VII at 3000 rpm at various whirl ratios and cavitation numbers ($\phi = 0.074$).

Figure 6.9 Non-dimensionalized normal force on inducer VII at 3000 rpm at various whirl ratios and cavitation numbers ($\phi = 0.049$).

Figure 6.10 Comparison of the non-dimensionalized normal force at 3000 rpm for the flow coefficients $\phi = 0.074$ and $\phi = 0.049$ at a cavitation number $\sigma = 0.106$.

Figure 6.11 Comparison of the non-dimensionalized normal force at 3000 rpm for the flow coefficients $\phi = 0.074$ and $\phi = 0.049$ at a cavitation number $\sigma = 0.098$.

Figure A.1 Flow through a screen designed to produce a linear shear flow.

Figure A.2 Two-dimensional flow through a screen with one opening in a pipe.

Figure B.1 Comparison of the normalized tangential force as a function of flow coefficient between experiment and actuator disk theory (from Colding-Jorgensen 1992) for inducer VII.

Figure C.1a The variation of non-dimensionalized downstream static pressure on the housing of inducer VII in the presence of downstream asymmetry.

Figure C.1b The variation of non-dimensionalized downstream static pressure on the housing of inducer VII with the downstream screen installed.

Figure C.2 Comparison of the normalized lateral force on inducer VII at 2000 rpm due to the downstream screen as obtained from the static pressures of figure C.1.

LIST OF TABLES

Table 2.1 Characteristics of the inducers used for the experiments.

Table 3.1A Limiting streamline angles, χ, on the suction surface of the 12^o inducer at $\phi = 0.083$.

Table 3.1B Limiting streamline angles, χ, on the pressure surface of the 12^o inducer at $\phi = 0.083$.

NOMENCLATURE

A	inducer cross-sectional area (πr_2^2)
A_j	area of one hole (opening) in flow distortion screen
$[A]=\begin{bmatrix} A_{xx} & A_{xy} \\ A_{yx} & A_{yy} \end{bmatrix}$	hydrodynamic force matrix, non-dimensionalized by $\rho\pi\omega^2 r_2^2 l$
[B]	matrix of slopes (for dynamometer calibration)
$[C]=\begin{bmatrix} C_{xx} & C_{xy} \\ C_{yx} & C_{yy} \end{bmatrix}$	generalized damping matrix, non-dimensionalized by $\rho\pi\omega r_2^2 l$
c_d	drag coefficient
c_p	specific heat coefficient
c_x	axial velocity
c_{x0}	axial velocity far upstream
c_x', c_y'	perturbation velocities in the x, y directions of actuator disk
D_f	drag force
D_m	mean diameter
D_p	pipe diameter
$F(t)$	instantaneous force on the inducer, non-dimensionalized by $\rho\pi\omega^2 r_2^3 l$
$[F]$	instantaneous force matrix
$F_1(t)$, $F_2(t)$	instantaneous lateral forces on the inducer measured in the rotating dynamometer frame, non-dimensionalized by $\rho\pi\omega^2 r_2^3 l$
F_o	steady lateral force on the inducer, non-dimensionalized by $\rho\pi\omega^2 r_2^3 l$

F_{ox} , F_{oy}	components of the steady lateral force in the (X,Y) reference frame, non-dimensionalized by $\rho\pi\omega^2 r_2^3 l$
$F_x(t)$,$F_y(t)$	components of the instantaneous lateral forces in the (X,Y) reference frame, non-dimensionalized by $\rho\pi\omega^2 r_2^3 l$
F_n, F_t	components of time averaged force on the inducer which are normal and tangential to the whirl orbit respectively and normalized by $\rho\pi\omega^2 r_2^2 l\varepsilon$
f	force per unit tangential length
$f_T{}'$	tangential force on a blade (per unit blade length)
H	blade height
h_{t1}, h_{t3}	total enthalpy at station 1 and 3
I/J	ratio of the whirl speed to the inducer rotational speed
$[K]=\begin{bmatrix} K_{xx} & K_{xy} \\ K_{yx} & K_{yy} \end{bmatrix}$	generalized stiffness matrix, non-dimensionalized by $\rho\pi\omega^2 r_2^2 l$
K'	screen resistance, $K_o[1+\varepsilon'(y)]$
K_o	static pressure coefficient, $\dfrac{(p_u - p_d)}{\frac{1}{2}\rho V^2}$
l	axial blade length of inducer
$[M]=\begin{bmatrix} M_{xx} & M_{xy} \\ M_{yx} & M_{yy} \end{bmatrix}$	generalized inertia matrix, non-dimensionalized by $\rho\pi r_2^2 l$
$\dot{m}$	mass flow rate
NCYC	number of data taking cycles
n	integer; 1,2...
P	power coefficient
P_z	power coefficient for zero leakage

p	mean static pressure
p_u, p_{tu}	static and total pressures, upstream
p_d, p_{td}	static and total pressures, downstream
p_i	static pressure at inducer inlet, $p_{tu} - \frac{1}{2}\rho\left(\frac{Q}{A}\right)^2$
p_v	vapor pressure of water
Δp_t	total pressure rise between upstream and downstream
Q	flow rate
Q'	shear layer strength
q	dimensionless shear layer strength (Q'/c_{x0}^2)
R	mean radius, $D_m/2$
R'	hole radius in flow distorting screen
r_1	inducer hub radius
r_2	inducer tip radius
S	blade spacing, $2\pi r_2$/number of blades
s	solidity (blade chord/spacing ratio)
T	time period
T'	torque
T_{01}	stagnation temperature at station 1
t	time
u_1, u_2	inducer speed at hub (ωr_1) and at tip (ωr_2)
$[V']$	matrix of voltages
V	mean flow velocity
$v(y)$	velocity at each radial location (y) downstream of flow distorting screen
w	work defect coefficient

X, Y	axes of the stationary laboratory frame
x, y	instantaneous coordinates of the inducer center in the fixed reference frame, non-dimensionalized by r_2
$\dot{x}$, $\dot{y}$	time derivatives of x and y, non-dimensionalized by $r_2\omega$
$\ddot{x}$, $\ddot{y}$	acceleration, non-dimensionalized by $r_2\omega^2$

Symbols

α	angle made by the absolute velocity vector with the axial direction
α'	refraction factor for the flow in the tangential direction through screen
β	angle between the relative velocity vector and the axial direction
β_t	blade angle at tip ($\beta_t = 90^o - \beta$)
χ	limiting streamline angle (measured with respect to the tangential direction on the blade surface)
δ	clearance between blade tip and stationary housing
ε	radius of the whirl orbit, non-dimensionalized by r_2
ε'	screen resistance grading factor
ϕ	flow coefficient, $\frac{Q}{u_2 A}$
η	efficiency
Λ	numerical factor, 1-2
λ	overall efficiency change per unit global clearance increase

λ'	fractional flow through clearance gap
λ''	parameter which determines the slope of the linear shear flow
ρ	density of the working fluid (water)
σ	cavitation number, $\frac{(p_i - p_v)}{\frac{1}{2}\rho u_2^2}$
Ω	frequency of whirl motion
ω	inducer rotational frequency
ω_y	vorticity in tangential (y) direction (actuator disk)
ξ	Alford constant
ξ'	fractional blockage area, $(A-A_j)/A$
Ψ	stream function
ψ	head coefficient, $\Delta p_t/(\rho u_2^2)$

Subscript

o	mean value

CHAPTER 1

INTRODUCTION

Axial flow inducers such as those used in high-speed turbopumps are subject to complex internal flows and fluid-induced rotordynamic forces. Internal flows in these axial flow devices are in fact three-dimensional and are characterized by secondary flow effects. The flow patterns are governed by the inducer geometry and the operating conditions, especially the occurrence of reverse flows. It is important to understand the flow reversal and internal flow patterns which could possibly be influencing the performance of the pump and the forces acting on it.

Rotordynamic forces can cause dynamic instabilities in the turbomachine shaft/support system and lateral forces may cause rapid bearing wear or failure. Such forces are aggravated or diminished by various conditions of design and operation. Modern high-speed turbomachines such as those used in the space shuttle main engine operate at very high speeds to obtain the maximum power to weight ratio. While current designs of these turbomachines do succeed in reducing weight and attaining higher power than previous designs, they are also prone to failure caused by rotordynamic instabilities arising out of fluid-induced forces (of a large magnitude due to high-speed operation). The reduction in weight leads to reduced structural strength, thereby making the device susceptible to failure. Hence it is important to identify the operating conditions at which the machine is rotordynamically unstable. It is also important to understand the effects of flow asymmetries and cavitation on these forces. Due to the inadequacies of current analytical techniques in predicting these forces accurately, experimental techniques are used as a starting point to gain a fundamental understanding of these forces.

The present research focuses on these issues, viz., the rotordynamic forces in axial flow inducers, the manner in which these forces are affected by upstream and downstream flow asymmetries, and the effects of operating conditions such as reduced flows and cavitation. The internal flows and flow reversal in these inducers are also investigated in an effort to understand the complexity of these flows and their effects on the forces.

1.1 STATEMENT OF THE PROBLEM

The forces acting on turbomachines that lead to excessive vibration and failure may arise out of mechanical and fluid-induced causes. Among the mechanical causes are the vibrations introduced by mass imbalances leading to the problems of critical speed, cyclical variations of the transverse moment of inertia and due to the lack of adequate stiffness of the support structure. In addition, there are also forces due to purely fluid-induced causes, arising out of the interaction of the working fluid with the physical structure of the turbomachine. These forces are the cause of rotordynamic forces (explained in section 1.3 below) and instabilities and lateral loads. The focus of the research presented in this thesis are the fluid-induced forces (rather than the forces due to mechanical causes) and internal flows in axial flow inducers.

Turbomachines usually operate with a certain amount of deflection of the rotor with respect to the machine centerline. In addition to the rotation of the impeller, the rotor may also tend to whirl around the machine centerline. The forces acting on the impeller may tend to increase this deflection and may also increase the whirl frequency causing rotordynamic instability. The extent of deflection of the shaft is dictated by the radial clearances of the impeller with the housing and the structural constraints of the shaft and supports. Since forces vary as the square of the speed, such effects are especially important in high-speed turbomachinery. The vibrations caused by the forces may be *synchronous* (i.e., the whirl frequency is the same as the shaft rotational frequency) or *asynchronous* (i.e., whirl frequency is not the same as the shaft frequency). These whirling motions are *self-excited* i.e., occurring without an external forcing function, and are generated by fluid forces within the system. Some of the aspects of self-excited vibrations have been studied by Ehrich and Childs (1984) and Alford (1965). Previous studies (e.g., Jery 1986, Franz 1989) have shown the effects of these fluid-induced forces on several designs of centrifugal pumps.

Such fluid-induced forces arise due to flow redistributions that occur due to a displacement of the shaft from the centerline and also due to the presence of flow distorting situations such as an inlet shear flow or asymmetric geometries both upstream and downstream. The forces may also be affected by the phenomenon of cavitation, a condition under which inducers are in fact required to operate. The research presented in this thesis investigates the forces arising out of the presence of upstream and downstream flow asymmetries in the system and the effects of inlet shear flow and a bend in the inlet piping, and the forces caused by the cavitation of the device.

One other aspect that is intimately associated with the forces is the nature of the internal flows and flow reversals that occur at flow coefficients below design. These internal flows are highly complex and three-dimensional and are as yet not completely understood. The current research uses flow visualization techniques to describe the boundary layer flows on the blade passage, hub and housing. The effect of placing a rotating shroud on the inducer blade tip also revealed the flow reversal patterns existing on the outer casing. The results of these experiments will ultimately enable better design and selection of operating conditions of these devices.

1.2 INDUCERS AND THEIR APPLICATIONS

A brief introduction to axial flow inducers is presented in this section. The material presented here is not exhaustive and the reader is referred to the references used in this section for further details. The term "inducer" is derived from supercharger terminology (Acosta 1958) and refers to a device that causes a rise in the inlet head which prevents cavitation in a pump stage following the inducer. Inducers are therefore used at the inlet portion, especially in turbopumps used in liquid rocket engines. They are typically designed to be axial flow devices. Inducers are usually impellers with a high solidity (i.e., ratio of blade chord to spacing) so that long narrow passages result. Cavitation bubbles collapse in these passages before they reach the main pump. Among the first papers dealing with the functions and flows of inducers is by Ross and Banerian (1956) and by Acosta (1958). The reader is also referred to Jakobsen (1971) for a detailed account of inducer design classification. A review of the fluid dynamics of inducers has been presented by Lakshminarayana (1982) and by Acosta (1992). The inducers used for the current research have a meridional cross-section of a cylindrical tip and hub. The helix pitch is held constant and the inducers have a swept back leading edge. A shrouded inducer has also been used in the study of internal flows. The characteristics of these inducers are described in detail in chapter 2.

1.3 ROTOR WHIRL AND FORCE MATRICES

This section introduces the basic concepts of rotor whirl and force matrices associated with whirling pump impellers. A detailed account of these concepts can be found in Jery (1986) and Franz (1989). Due to the limited stiffness of the rotor and the bearings, the rotor axis may be expected to deflect from its centerline position, due to at least the weight of the impeller and due to centrifugal unbalanced loads and possible fluid-induced forces including net unbalance and forces due to the impeller through flow. These various possible forces acting on the impeller which is whirling in an orbit around the undeflected position is shown in figure 1.1. The displacement of the rotor at any time is given by the vector $\varepsilon(t)$ (for a circular whirl orbit, this ε is time independent). Let $F(t)$ be the instantaneous force acting on the impeller. The rotational speed of the inducer is given by ω and that of the whirling motion is denoted by Ω. The force $F(t)$ can be decomposed into two components: $F_n(t)$ and $F_t(t)$, i.e., components normal to and along the tangent at a point on the whirl orbit respectively. In essence, rotordynamics is the study of the unsteady normal and tangential forces and the stability of the whirl motion is determined by whether the direction of $F_n(t)$ and $F_t(t)$ increases the displacement of the whirl orbit or whirl speed.

The instantaneous force matrix $[F]$ can be expressed as the sum of a steady-force matrix $[F_o]$ and a rotordynamic-force matrix $[A]$:

$$\begin{bmatrix} F_x \\ F_y \end{bmatrix} = \begin{bmatrix} F_{ox} \\ F_{oy} \end{bmatrix} + \frac{\varepsilon}{r_2} \begin{bmatrix} A_{xx} & A_{xy} \\ A_{yx} & A_{yy} \end{bmatrix} \begin{bmatrix} \cos\Omega t \\ \sin\Omega t \end{bmatrix} . \qquad (1.1)$$

It has been experimentally proven in closely related systems that the components of the rotordynamic matrix $[A]$ for a circular whirl orbit are such that:

$$A_{xx} = A_{yy}$$

and

$$A_{xy} = -A_{yx}. \qquad (1.2)$$

This condition would also arise due to rotational invariance. Experimental verification of this skew-symmetry of the rotordynamic matrix is obtained from previous studies such as the one reported by Jery (1986) and Franz (1989).

The forces normal to the whirl orbit (F_n) and tangential to the whirl orbit (F_t) can then be expressed as :

$$F_n = \frac{1}{2}(A_{xx} + A_{yy}) = A_{xx} = A_{yy} \qquad (1.3)$$

and

$$F_t = \frac{1}{2}(A_{yx} - A_{xy}) = -A_{xy} = A_{yx}, \qquad (1.4)$$

because of the skew symmetry.

The sign conventions are such that F_n is positive outward and F_t is positive in the direction of rotation. It follows that a *positive* tangential force is destabilizing (in the sense that it tends to increase the whirl speed) when the whirl motion is in the same direction as the shaft rotational motion (i.e., a positive whirl/shaft speed ratio). Conversely, a negative F_t tends to stabilize the whirl motion for a positive whirl/shaft speed ratio. Likewise, a positive F_t would be stabilizing for a *negative* whirl motion. In the case of the normal force, a positive (outward) force could be considered as a destabilizing force in the sense that it tends to increase the radius of the whirl orbit and to act in a direction opposite to its natural stiffness.

Rotordynamicists typically characterize these forces in terms of inertia, stiffness and damping matrices for stability analysis in the following manner:

$$\begin{bmatrix} F_x \\ F_y \end{bmatrix} = \begin{bmatrix} F_{ox} \\ F_{oy} \end{bmatrix} - [K]\begin{bmatrix} x \\ y \end{bmatrix} - [C]\begin{bmatrix} \dot{x} \\ \dot{y} \end{bmatrix} - [M]\begin{bmatrix} \ddot{x} \\ \ddot{y} \end{bmatrix} + \text{higher order terms.} \qquad (1.5)$$

The matrices $[K]$, $[C]$ and $[M]$ are the stiffness, damping and inertia matrices respectively. It can be shown that the components of the rotordynamic force matrix $[A]$ can also be expressed in terms of the components of the stiffness, damping and inertia matrices as:

$$A_{xx} = M_{xx}\left(\frac{\Omega}{\omega}\right)^2 - C_{xy}\left(\frac{\Omega}{\omega}\right) - K_{xx} \qquad (1.6)$$

$$A_{xy} = M_{xy}\left(\frac{\Omega}{\omega}\right)^2 + C_{xx}\left(\frac{\Omega}{\omega}\right) - K_{xy} \qquad (1.7)$$

$$A_{yx} = M_{yx}\left(\frac{\Omega}{\omega}\right)^2 - C_{yy}\left(\frac{\Omega}{\omega}\right) - K_{yx} \qquad (1.8)$$

$$A_{yy} = M_{yx}\left(\frac{\Omega}{\omega}\right)^2 + C_{yx}\left(\frac{\Omega}{\omega}\right) - K_{yy}. \qquad (1.9)$$

The above formulation implies that the coefficients of the stiffness, damping and inertia matrices can be obtained from rotordynamic force data if the forces can be expressed as a quadratic function of Ω/ω. Rotordynamic forces in centrifugal pumps, for example, do indeed show a quadratic variation of the forces with Ω/ω (Jery (1986), Franz (1989)). Recent studies of rotordynamic forces due to leakage flows have also shown such a quadratic relation (Guinzburg 1992). The research presented in this thesis investigates whether the rotordynamic forces on an inducer also show a quadratic behavior with Ω/ω and the manner in which these forces are affected by flow distortions and cavitation.

It should be noted that the data presented in this thesis represents purely fluid-induced forces in the sense that the effects of tare forces (the dry weight of the inducer and the centrifugal forces arising by running the inducer in air) have been subtracted from the total force. The steady and unsteady forces presented are mean values obtained by integration over many cycles of rotation and whirl. The normal force (F_n) and the tangential force (F_t) are normalized by $\rho\pi\omega^2 r_2^2 l\varepsilon$. The steady forces ($F_o$ with components F_{ox} and F_{oy}) are normalized by $\rho\pi\omega^2 r_2^3 l$ where ρ is the density of the fluid, r_2 is the inducer tip speed and l is the axial blading length.

1.4. LITERATURE REVIEW

Internal flows in axial flow inducers have been studied by several researchers, but the complexities of these flows still remain to be fully understood. Acosta (1958) conducted an experimental study on several cavitating inducers. In this study, the non-cavitating flows on a 12^o helical inducer were examined using tufts at various flow coefficients. The occurrence of backflows upstream of the inducer were recorded. It was noted that at the flow coefficients for which strong upstream backflows developed, the suction surface of the blade near the leading edge did not appear to be separated. Acosta (1958) postulates that the strong tip clearance flow at the leading edge may be the agent of the upstream disturbance (backflow). Strong radial flows were observed on the pressure side just downstream of the leading edge and secondary flows were observed on the hub. The flow also appeared to separate about halfway through the impeller. Acosta (1992) provides a more recent review of the flows in inducers and their behavior with cavitation.

Studies on the internal flows inducers have also been conducted by Lakshminarayana (1972, 1982). Visualization studies of flow in a four-bladed helical inducer in air were reported. The results showed that the flows in such devices are highly complex and three-dimensional. The internal flows are characterized by viscous real fluid effects which lead to the predominance of boundary layer flows in the blade passage area. Lakshminarayana (1982) points out that there may be only very small regions where inviscid flow effects are present. The study reported by Lakshminarayana (1972) showed that the reverse flow (in the inducer used for those experiments) on the hub occurred before the upstream reverse flow. Further, the report states that the reverse flow on the hub originated near the blade trailing edge. Radial components of the flow were also noted; the radial velocity increased continuously from the leading edge to the trailing edge of the blade. Limiting streamline angles (i.e., the limiting position of the streamline as the blade surface is approached) were also measured. The study reports that the radial movement inside the blade boundary layer, when encountered by the annulus wall, tend to deflect towards the mid-passage and then radially inward. Based on these observations, a qualitative picture of the flow is postulated and this is reproduced in figure 1.2. Lakshminarayana (1978) states that the radial component of velocity contributes to the energy addition to the fluid through the Coriolis and centrifugal forces in the boundary layers. The radial velocity provides a vehicle for momentum exchange between the fluid and the rotor via the shear stress. This phenomenon has been referred to as the "shear pumping effect" (Lakshminarayana 1978).

Measurements and predictions of the three-dimensional flow fields in an axial flow inducer have been presented by Lakshminarayana and Gorton (1977).

Tanaka (1980) presented an experimental study of the backflow phenomenon in a high specific speed propeller pump. This work shows the dependence of the onset of the upstream and downstream flow reversal on the geometry. For the mixed-flow type pumps investigated, the study concluded that upstream backflow affected the downstream flow condition (by increasing the magnitude of the peripheral velocity component and decreasing the axial velocity component). The study also relates the occurrence of flow reversals with the performance of these pumps.

Howard et al. (1987) have reported the LDA measurements of the internal and upstream velocity fields of an axial flow inducer at off-design conditions, particularly within the flow range of the formation and propagation of tip stall. The measurements imply a radially outward shift in the streamline within the inducer. The near hub axial velocity is seen to fall rapidly with reduction in flow rate, thus contributing to hub stall (Howard et al. 1987). More recently Howard et al. (1993) and Howard and Atif (1993) have provided analytical models and experimental measurements of the flow fields in an axial flow inducer. Boccazzi et al. (1990) have also reported LDV measurements of the flow field within a low solidity inducer. The study inferred that backflow was related to high relative velocities and high local incidence angles occurring on the suction side at the tip because of reduced axial velocities in front of the blade leading edge. The flow configuration was caused partly by the inlet boundary layer at the casing, but mostly by static pressure rise occurring just after the leading edge. The flow field at the outlet was also found to be non-uniform. The axial velocity component decreased considerably near the hub and the casing wall. A reverse flow region was also detected on the hub (Boccazzi et al. 1990). Various aspects of secondary flows in axial flow inducers have also been discussed by Brennen (1994).

The effects of inlet flow disturbances on pump performance have been studied by a few researchers. Early work on this subject includes an experimental and analytical investigation by Katz (1958) on axial flow compressors. A two-dimensional linearized theory was developed to include the effect of losses and leaving angle deviations in the blade. Overall performance measurements and circumferential surveys of total pressures, velocities and flow angles were obtained. It was found that introducing inlet disturbances did not alter the two-dimensional character of the flow through the compressor and that considerable attenuation of disturbances occurred through a single rotor stage. The theory qualitatively described the flow behavior (Katz 1958). Ehrich (1957) performed an actuator disk analysis to determine the effect of a non-uniformity in the circumferential velocity profile entering an axial stage of turbomachinery. The analysis was restricted to incompressible, inviscid flows with a two-dimensional assumption (high hub/tip ratio). Expressions were derived to obtain the velocity disturbance attenuation through the stage, the circumferential shift in the profile, and the fluctuation in the rotor load, as a function of geometry. The study found the regimes of attenuations typical of compressors and turbines and concluded that for compressors, lower reaction staging would lead to better attenuation, while in turbines, a higher reaction stage would result in lower blade load fluctuation (note that compressors are designed for minimizing load fluctuations while turbines are designed for best attenuations of distortions; Ehrich 1957).

More recent work on inlet distortion effects on performance is an experimental investigation of Del Valle et al. (1990) on cavitating inducers. The effects of inlet distortions generated by honeycomb sections were investigated on two cavitating inducers, one is inducer VII (also used for the current work) and the other a model of the low pressure LOX pump in the Space Shuttle Main Engine. Uniform and non-uniform honeycombs were used this study. Non-uniform honeycomb sections of a similar type were also used for preliminary force measurement in the current study (see section 2.4.1 and chapter 5). The study by Del Valle et al. (1990) noted that significant improvement in the performance over a wide range of flow coefficients resulted from the use of either the uniform or the non-uniform honeycomb section. The study showed that the effects on the performance, if any, of the non-uniform honeycomb was much smaller than the change occurring with and without honeycomb inserts. Measurements were also made of the axial and swirl velocity profiles of the inlet flow. The measurements showed that backflows occurred with increased loading at a certain critical flow coefficient and that the extent to which the backflow penetrated upstream increased with reduction in the flow coefficient. Prerotation of the flow only occurred at flow coefficients below the critical flow coefficient. The swirl is not confined to the backflow jet. The vorticity of the backflow jet is diffused inward so that swirl velocities are measured over virtually all of the inflow. The study states that the mechanism of such rapid diffusion of the vorticity must be turbulent convection resulting from the high degree of unsteadiness associated with the flow (Del Valle et al. 1990; Brennen 1994). This study thus provides useful insights into the formation of upstream swirling backflow in these inducers. The performance enhancement was probably due to reduction in the swirl velocities due to the honeycomb sections, but this does not fully explain the enhanced performance over the entire range of flow coefficients (Del Valle et al. 1990). Figure 1.3 shows the performance curves of inducer VII with and without honeycombs for the experiments reported by Del Valle et al. (1990).

It has been recognized for some time that fluid-induced forces (radial and rotordynamic) on pump impellers can cause bearing wear or failure and rotordynamic instability. Alford (1965) addressed the issue of self-excited rotor whirl in axial flow compressors. He postulated that the forces causing rotor whirl may arise due to circumferential variations of static pressure on the surface of the rotor and due to a circumferential variation of the blade-tip clearance. The circumferential variation of the clearance causes a corresponding change in the local efficiency and unbalanced torque. Iverson et al. (1960) and Biheller (1965) studied radial loads on centrifugal pumps. Rosenmann (1965) also experimentally measured radial forces on cavitating inducers. Rotordynamic forces on centrifugal pumps were measured by Domm and Hergt (1970), Hergt and Krieger (1969), Chamieh et al. (1985), Jery (1986), Adkins et al. (1988) and Franz et al. (1989). These studies include those done on centrifugal pump impellers whirled over large whirl frequency ratios at the Rotor Force Test Facility (RFTF) at the California Institute of Technology. The steady bending moments and rotordynamic moments due to fluid flow on centrifugal pump impellers has also been presented by Miskovish and Brennen (1992). Vance (1988) has also dealt with several issues of rotordynamics in turbomachinery.

However, there is a lack of literature on rotordynamic and lateral forces in axial flow inducers, especially on the effects of cavitation and flow distortions on these forces. Some preliminary work on the forces in non-cavitating inducers was conducted by Arndt and Franz (1986) on two inducers and a scaled model of the low pressure oxygen turbopump (LPOTP) of the Space Shuttle Main Engine (SSME). That study had concluded that the lateral and rotordynamic forces on the inducers differed from that of the SSME main impeller. It was also noted that the forces varied strongly with flow coefficient and that the rotordynamic forces on the inducers showed multiple zero crossings when plotted against the whirl frequency ratio (Arndt and Franz 1986). Studies were also conducted to investigate the rotordynamic forces due to cavitation and tip clearance variation on an SEP inducer by Karyeaclis et al. (1989). This study also noted the occurrence of multiple zero crossings of the rotordynamic force and that the effect of cavitation was to increase the magnitude of the forces throughout the range of whirl frequency ratios. Brennen (1994) provides a comprehensive overview of the various aspects of fluid flows, fluid-induced forces and rotordynamic analysis of various types of pump impellers.

1.4.1. ACTUATOR DISK FORCE PREDICTION MODELS

In recent years, there has been a trend to use actuator disk theory in the prediction of flow perturbations and forces in axial flow turbomachinery. An actuator disk is 'an artificial device producing sudden discontinuities in flow properties'; several applications of this theory are mentioned by Horlock (1978). An actuator disk analysis on non-uniform flows in axial flow compressors due to tip clearance variations was presented by Horlock and Greitzer (1983). Calculations were made for configurations in which the tip clearance is stationary as well as for configurations in which the tip clearance rotates with the rotor. The velocity variations associated with a rotating clearance were found to be considerably more severe than with a stationary clearance (Horlock and Greitzer 1983).

1.4.1a TURBINE BLADE TIP AND SEAL CLEARANCE FORCES

A detailed analysis of turbine blade tip and seal clearance excitation forces using actuator disk theory was undertaken at the Gas Turbine Laboratory at the Massachusetts Institute of Technology (Martinez-Sanchez and Jaroux 1992). Since the analysis has its applications for axial flow turbomachinery in general, an overview of the theory by Martinez-Sanchez and Jaroux (1992) is presented in this section. The objective of the analysis was to understand the perturbations in the flow caused by the non-symmetric placement of an offset turbine and the prediction of Alford forces (i.e., cross forces). Actuator disks were used to model the rotor and the stator and an ordering principle, based on proper scaling, was used to sort out the various phenomena associated with the problem.

The three length scales identified for the problem were: (a) the scale of the gap (clearance, δ), which includes the discharge jet, boundary layers on the hub and tip, location of the separation bubble at the gap etc.; (b) the blade scale (H), i.e., radial flows towards the gap, formation of a vortical rolled up structure on the downstream side, flow underturning over the outer blade span etc.; and (c) the radius scale, i.e., azimuthal variations of efficiency, work per blade, pressure non-uniformity, and flow redistribution.

The efficiency (η) of a turbine is empirically observed to decrease linearly with increase in the tip clearance:

$$\eta = \eta_0 - \Lambda\frac{\delta}{H}; \text{ where } \Lambda \text{ is a numerical factor, 1-2.} \qquad (1.10)$$

Using the formulation of Alford (1965) the force per unit tangential length of the turbine also decreases with increase in the clearance as:

$$\frac{f}{f_{ideal}} = \frac{f_o}{f_{ideal}} - \Lambda \frac{\delta}{H}. \tag{1.11}$$

It can then be shown that the net cross force, F_y, on the rotor can be obtained in terms of the ideal torque T'_{ideal}, the factor Λ, and a fixed eccentricity (ε_x) along the horizontal X-axis (figure 1.1) as :

$$F_y = \frac{\Lambda}{2}\left(\frac{T'_{ideal}}{r_2}\right)\left(\frac{\varepsilon_x}{H}\right) \tag{1.12}$$

(where r_2 is the blade radius at tip).

The actuator disk formulation involves the assumption of incompressible, inviscid flow in two dimensions. Uniformity is assumed along the tangential (y) direction. The stage is collapsed in the axial direction to a single plane and smeared in the azimuthal direction. Figure 1.4 shows the formulation and the blade angles associated with the stages (note that the problem is now in the (x,y,z) coordinates, as opposed to the (X,Y,Z) frame used in the force analysis of figure 1.1).

The problem was first solved in the blade scale. The actuator disk was placed at x=0. The upstream flow was irrotational and the flow at $x \geq 0$ had a vorticity $\omega_y(\Psi)$ (= $\nabla^2\Psi$) where $\Psi(x,z)$ is the stream function (to be determined). Using several manipulations on the momentum equations and the Euler equations and assuming no work done by the gap fluid, the equations for the stream function were obtained as:

Upstream: $\nabla^2\Psi = 0$

Downstream: $\begin{Bmatrix} \text{GAP} \\ \text{BLADES} \end{Bmatrix}$

$$\nabla^2\Psi = \begin{Bmatrix} -\tan^2(\alpha_2) \\ -[\frac{u_2}{(c_x)_{x=0}}\tan(\alpha_2)+\tan^2(\beta_3)] \end{Bmatrix} \left(\frac{\partial c_x}{\partial z}\right)_{x=0} + Q'\delta(\Psi-\Psi_{tip}), \quad (1.13)$$

where u_2 is the tip speed and c_x is the axial velocity. The blade angles of the stages 2 and 3 are as defined in figure 1.4. Q' is the strength of the shear layer between the gap and the bladed region and is given by $Q' = \int_{-}^{+} \omega_y d\Psi$ ('+' and '-' represent the gap and the blade regions respectively). 'δ()' represents the Dirac delta function. The boundary conditions for the problem are:

$$\Psi(x, 0) = o;\ \Psi(x, H) = c_{x0}H\ ;$$
$$\Psi(-\infty, z) = c_{x0}z;\ \frac{\partial\Psi}{\partial x}(+\infty, z) = 0;\ (c_{x0} \text{ is the far upstream axial velocity})$$
$$\Psi(0^-, z) = \Psi(0^+, z);\ \frac{\partial\Psi}{\partial x}(0^-, z) = \frac{\partial\Psi}{\partial x}(0^+, z). \quad (1.14)$$

The MIT report states that the axial velocity distribution consists of two constant but different velocity levels: one for the gap and one for the bladed region. This was proved using a result of the linearized actuator disk theory which states that a disturbance at the disk is half that of far downstream (i.e., along a streamline, $\left(\frac{\partial c_x}{\partial z}\right)_{x=\infty} = 2\left(\frac{\partial c_x}{\partial z}\right)_{x=0}$). Using the mathematical techniques of inverse coordinates and linearization, the axial flow velocity (c_x) in the gap and the bladed region, and the fractional flow through the gap λ' are then obtained from the problem formulated for the stream function. The following were the results obtained:

at the gap: $c_x/c_{x0} = 1 + (Q'/2c_x^2)(1-\lambda')$

at the bladed region: $c_x/c_{x0} = 1 - (Q'/2c_x^2)(\lambda')$ (1.15)

and $\lambda' = \dfrac{2(\delta / H)}{\left\{1 - \frac{q}{2} + \sqrt{\left(1 - \frac{q}{2}\right)^2 + 4\left(\frac{\delta}{H}\right)\left(\frac{q}{2}\right)}\right\}}$ where q is a dimensionless shear layer strength, Q'/c_{x0}^2 and c_{x0} is the axial velocity far upstream.

The velocity distributions away from the disk are then obtained from the vorticity equation in inverse coordinates as a Fourier series expansion which shows that the axial scale of near disk potential effects is H/π. The power coefficient (P) extracted by the turbine is obtained by the following equation:

$$P \equiv \frac{1}{\dot{m} u_2^2} \int_0^{\Psi_{tip}} (h_{t1} - h_{t3}) \rho \, d\Psi \tag{1.16}$$

where h_{t1} and h_{t3} are the total enthalpies of stages 1 and 3, $\dot{m}$ is the mass flow rate and Ψ_{tip} is the value of the stream function at the blade tip. Defining P_z as the power coefficient for zero leakage, the work defect coefficient (w) is obtained from:

$$w = \frac{1 + \frac{P_z + 1}{P_z} \frac{1 - \lambda'}{2} q}{1 - \frac{1 - \lambda'}{2} q}. \tag{1.17}$$

The efficiency (η) is obtained from: $\eta = \dfrac{P}{\left(\dfrac{p_{tu} - p_{tmix}}{\rho u_2^2}\right)}$ (1.18)

where p_{tu} and p_{tmix} are the total pressures far upstream and at a "mixed out" downstream station (where the shear layer has dissipated and the conditions are again uniform).

A modified theory has also been presented by Martinez-Sanchez and Jaroux (1992) to include the partial work done by the gap fluid. The tangential velocity of the fluid in the gap was obtained and the final result for the power coefficient was given by:

$$P = P_z - \lambda' \phi(\tan\beta_3 - g)\left(1 + \frac{1-\lambda}{2} q\right), \tag{1.19}$$

where $g = \left(\frac{\cos\theta \sin(\beta_m - \theta)}{\cos\beta_m}\right)$

and β_m is defined as $(\beta_3 - \beta_{2(DES)})/2$ as a average angle of the rotor blades to the axial direction. The subscripts 2,3 refer to the stages and "DES" refers to the design value. The angle "θ" in the above equations is obtained from the dynamics of the rolled up tip vortex in terms of blade lift coefficient as:

$$\theta = \begin{cases} \sqrt{\dfrac{4}{4 + c_L}} & (c_L < 4) \\ \sqrt{\dfrac{c_L}{4 + c_L}} & (c_L > 4) \end{cases} . \tag{1.20}$$

The problem is then solved for the flow perturbations upstream and downstream on a length scale of O(H/π). The details of the analysis is not presented here and the reader is referred to the report (Martinez-Sanchez and Jaroux 1992) for the same. The upstream and downstream perturbed equations of motion (the perturbations being in the azimuthal direction) were evaluated and the connecting conditions at the disk were used to obtain a solution for the perturbation in the far upstream axial flow velocity as a complex quantity, the imaginary part which gives the perturbation velocity in the tangential direction. The analysis was done to include the effect of imposing a circular whirl motion of a frequency (Ω) on the rotor.

The radial forces and Alford force coefficients were then obtained using the flow quantities obtained above. The work per unit length gives the tangential force (f_T)on the blade at a given circumferential location as:

$$f_T = \rho c_{x0} H\left[\lambda'\left(c_{y2}^{gap} - c_{y3}^{gap}\right) + (1-\lambda')\left(c_{y2}^{bladed} - c_{y3}^{bladed}\right)\right] \tag{1.21}$$

where the superscripts indicate the tangential velocity components of the tip gap region and the blade region. The tangential force (f_T) varies in the azimuthal direction and consists of a mean part ($\bar{f}_T$) and a perturbation component (f_T'). Only the perturbation part contributes to the net projected forces. Thus, the normal (F_n) and the tangential (F_t) forces on the rotor are obtained as the integrals of the sine and cosine components of f_T', over the circumferential length ($2\pi r_2$). The Alford coefficients in the normal and tangential direction are then obtained as:

$$\xi_n = \frac{F_n}{\pi r_2 \bar{f}_y (\varepsilon / H)}$$

and

$$\xi_t = \frac{F_t}{\pi r_2 \bar{f}_y (\varepsilon / H)}. \tag{1.22}$$

In the absence of flow redistributions in the azimuthal direction, it can be shown that the Alford constants reduce to zero in the normal direction and to a constant work coefficient in the tangential direction. The theoretical results for the Alford coefficient were also presented for a turbine. The plot of the Alford coefficient as a function of the whirl frequency ratio is reproduced in figure 1.5. However, these results have not been verified experimentally and no experimental dynamic data has been presented in the MIT report (Martinez-Sanchez and Jaroux 1992). Some steady force data (i.e., lateral forces) have been presented in the MIT report for static offsets of the rotor along the horizontal (X) axis. However, the turbine data was obtained at flow coefficients significantly higher than those typical of axial flow inducers and thus a comparison of the turbine force to the current data (see chapter 5) cannot be made. The results of the normal and tangential forces for static offsets of the rotor as reported by Martinez-Sanchez and Jaroux (1992) is presented here in figure 1.6 . The data is normalized in the same manner as the normalization of rotordynamic forces elsewhere in this thesis.

1.4.1b. FORCES IN AXIAL FLOW COMPRESSORS

Using an actuator disk model similar to the one by Horlock and Greitzer (1983), Colding-Jorgensen (1992) presented an analysis of the perturbed flow in an axial flow compressor and a prediction of destabilizing (tangential) forces due to a fixed offset (and zero whirl frequency) of the rotor. The model used has its potential application to axial flow inducers too, in the prediction of these forces. The model predicts the cross-coupling stiffness coefficient associated with an offset rotor. However, it does not provide a means to predict dynamic forces (i.e., those due to a whirling rotor) but does provide a starting point towards an analytical prediction of these forces. The work presented by Colding-Jorgensen (1992) is briefly reviewed in this section.

The postulation of Alford (1965) and Thomas (1958) with respect to the cross force in a turbomachine can be expressed in terms of a cross-coupled stiffness coefficient:

$$K_{XY} = -K_{YX} = \frac{T'\xi}{D_m l} \tag{1.23}$$

where T' is the torque (positive for a compressor), D_m is the mean diameter, l is the blade length and ξ is a constant determined by the change in the thermodynamic efficiency per unit change in clearance. However, for practical applications, this ξ is a "fudge factor" used to provide a match between empirical data and theory. Studies such as the one by Vance and Laudadio (1984) have shown that ξ is not constant and changes in magnitude and sign according to process parameters (and hence changes the sign of the tangential force). Colding-Jorgensen (1992) provides an analytical technique to determine the factor ξ for an axial flow compressor in terms of a function of the overall efficiency change per unit global clearance increase, the flow coefficient (ϕ) and in terms of the blade angles of the rotor and the stator stages. The result was obtained on the basis of an analysis of the flow perturbation in the blade row of a deflected rotor.

An actuator disk similar to the concept used in the MIT turbine theory was used. In the case of a compressor, however, the rotor blade row precedes the stator blade row. The actuator disk model assumes continuity of local axial velocity at the disk and that the flow angles and pressures are discontinuous. A high hub/tip ratio allows a two-dimensional analysis of the problem. A perturbation stream function (Ψ) is introduced to obtain the velocities perturbations as:

$$c_x' = \frac{\partial \Psi}{\partial y} \text{ and } c_y' = -\frac{\partial \Psi}{\partial x} \tag{1.24}$$

where c_x' and c_y' are the velocity perturbations in the axial and tangential directions respectively. The tip clearance variation caused by a small eccentricity

(ε) of the rotor is given by $\delta = \bar{\delta} + \Delta\delta$, where $\Delta\delta = \varepsilon \exp(iy / R)$, y is the tangential direction and R= $D_m/2$. The stream functions used in the analysis were:

Upstream (station 1): $\Psi_1(x,y) = A\exp(iy / R + x / R) \quad \text{for } -\infty < x \leq 0$

Between rotor and stator (station 2):
$$\Psi_2(x,y) = F\exp(iy / R - x / R) + G\exp\left(iy / R - \tan\bar{\alpha}_2\, ix / R\right) \text{ for } x \approx 0$$

Downstream of stator (station 3):
$$\Psi_3(x,y) = B\exp(iy / R - x / R) + D\exp\left(iy / R - \tan\bar{\alpha}_3\, ix / R\right) \text{ for } 0 \leq x < \infty \quad (1.25)$$

where $\bar{\alpha}_2$ and $\bar{\alpha}_3$ are the mean absolute flow angles shown in figure 1.7. *A, B, D, F* and *G* are constants to be determined. The upstream flow is assumed to be irrotational and the downstream flow is rotational. The blade rows and the spacing between them are assumed to be infinitely thin so that x=0 can be used to specify the location of each blade row. The following matching conditions were then used at each blade row:

(a) continuity of axial velocity: $c'_{x1} = c'_{x2} = c'_{x3}$

(b) perfect guidance of fluid at each blade row:

$$\frac{\partial \Psi_2}{\partial y}(0,\ y)\tan\beta_2 = -\frac{\partial \Psi_2}{\partial x}(0,\ y)$$

and $$\frac{\partial \Psi_3}{\partial y}(0,\ y)\tan\bar{\alpha}_3 = -\frac{\partial \Psi_3}{\partial x}(0,\ y) \qquad (1.26)$$

The local variation of the efficiency due to local changes in the clearance is postulated to be the same as the overall efficiency resulting from similar global changes in clearance. The total to static compressor efficiency can be written as:

$$\eta = \frac{c_p T_{01}\left(\left(\frac{p_3}{p_{01}}\right)^{(\gamma-1)/\gamma} - 1\right)}{\left(c_{y2} - c_{y1}\right)u_2} \tag{1.27}$$

where c_p is the specific heat coefficient at constant pressure, T_{01} is the stagnation temperature at inlet, p refers to the mean static pressure at a given station, and c_{y1} and c_{y2} refer to the tangential velocities at stations 1 and 2 respectively.

A third condition can be expressed by the following manipulation:

$$\frac{\partial \eta}{\partial y} = \frac{\partial \eta}{\partial \delta}\frac{\partial \delta}{\partial y} \tag{1.28}$$

where $\frac{\partial \eta}{\partial \delta} = -\lambda$ is taken as the overall efficiency change per unit global clearance increase. The momentum balance in the tangential direction is expressed as:

$$\frac{\partial p}{\partial y} = -\rho\left(\bar{c}_x \frac{\partial c_y'}{\partial x} + \bar{c}_y \frac{\partial c_y'}{\partial y}\right) \tag{1.29}$$

where $\bar{c}_x$ and $\bar{c}_y$ refer to the mean axial and tangential velocities. The expression for the efficiency is perturbed to the first order in y and inserted into the momentum equation. The matching conditions are used to obtain the constants *B*, *F* and *G* in terms of *A*. These are then inserted into the perturbation equation to obtain an expression for *A*:

$$A = \frac{R\lambda\varepsilon Q_1}{u_2 \bar{\eta}^2 \left(1 + i\tan\beta_2\right)} \tag{1.30}$$

where $Q_1 = c_p T_{01}\left(\left(\frac{\bar{p}_3}{\bar{p}_{01}}\right)^{(\gamma-1)/\gamma} - 1\right)$.

The axial velocity perturbation is then obtained as:

$$c_x'(x=0)=\frac{\partial \Psi_1'}{\partial y}=\frac{iA}{R}\exp(iy/R). \tag{1.31}$$

Finally, the tangential force on the rotor blade is obtained from the Euler turbine equation (momentum balance on a control volume around the blade passage) and the expressions for the perturbed axial and tangential velocities are substituted. The tangential force, f_T', on a blade is then obtained as:

$$f_T' = \rho l c_{x1}'(x=0)\left(u_2 + 2\bar{c}_x\left(\tan\beta_2 - \tan\alpha_1\right)\right). \tag{1.32}$$

The net tangential force on the rotor, F_T, is obtained by integrating f_T' around the rotor. Thus,

$$F_T = \frac{\frac{\lambda Q_1 \pi \varepsilon}{2}}{u_2 \bar{\eta}} R\rho l \sin\beta_2\left(U + \bar{c}_x\left(2\tan\beta_2 + \cot\beta_2 - \tan\bar{\alpha}_1\right)\right). \tag{1.33}$$

The cross-coupled stiffness coefficient is then given by:

$$K_{XY} = \frac{\partial F_T}{\partial \varepsilon}. \tag{1.34}$$

Forward and backward whirl of the rotor will be excited depending on whether K_{XY} is positive or negative respectively. The results have been presented by Colding-Jorgensen (1992) as a plot of a non-dimensional cross-coupled stiffness coefficient:

$$\left(\frac{K_{XY}}{\lambda \pi \rho L U^2 R\sqrt{\eta}}\right)$$

as a function of the flow coefficient. An example of these results is shown in figure 1.7a for no inlet swirl and $\beta_2 = -60^{\circ}$. The value of the Alford constant (ξ)

can now be determined from the Alford expression upon substituting for the torque, not as a constant but as the following function:

$$\xi = \frac{\lambda \sin\beta_2}{\bar{\eta}}\left(1/\phi + 2\tan\beta_2 + \cot\beta_2 - \tan\bar{\alpha}_1\right). \qquad (1.35)$$

Figure 1.7b shows a plot of ξ against various values of ϕ for the case of no inlet swirl and $\beta_2 = -60^{\circ}$.

Colding-Jorgensen (1992) reports that the current analysis when compared with the experimental results of Vance and Laudadio (1984) for an axial blower showed an agreement in the behavior of the constant ξ.

In summary, the work presented by Colding-Jorgensen (1992) shows that the destabilizing force is not simply proportional to stage torque, but is instead a function of flow rate and blade angles. The theory predicts destabilization of forward whirl within the normal operation range of both axial compressors and turbines and predicts backward whirl for a stalling compressor. The results are in better agreement with experimental results than the Alford-Thomas formula.

1.5. OBJECTIVES OF THE RESEARCH

The above sections have stated the importance and the need for understanding the internal flows and forces on axial flow inducers. The literature survey has shown that the complicated internal flows, particularly the occurrence of reverse flow has not been completely understood. In particular, there is a lack of literature on the internal flows in shrouded inducers. Analytical techniques have not yet developed to the extent of completely modeling these flows. There is thus a need for further experimentation to obtain benchmark data. The research presented in this thesis is a step in that direction. Specifically, with respect to internal flows, the following were the research goals:

(i) to develop and use an effective technique to study the (non-cavitating) boundary layer flows on the blades, hub and housing;

(ii) to study these flows in both unshrouded and shrouded inducers;

(iii) to visualize the upstream flow reversals on the housing wall, and determine whether these flows are due to tip clearance leakage;

(iv) to determine the origin of reverse flows in both unshrouded and shrouded inducers.

The literature also revealed the lack of experimental data on the force matrices (i.e., lateral and rotordynamic forces) of axial flow inducers. Analytical work in this area (such as the previously reported research using actuator disk theory, section 1.4.1 above) has made important strides, but is, as yet, unable to predict these forces with accuracy. An experimental investigation was therefore conducted to understand these forces in axial flow inducers. The effect of varying flow conditions, such flow distortions upstream and downstream, and cavitation have also been investigated. In particular, the objectives of the research on the force matrices in axial flow inducers were the following:

(i) to investigate the rotordynamic and steady forces in whirling and non-whirling unshrouded inducers. Force data was to be obtained for various flow coefficients and various whirl frequency ratios, including both forward and reverse whirl;

(ii) to investigate the effect of a downstream asymmetry inherent to the system on the lateral and rotordynamic forces on an inducer. It will also be determined whether the imposition of a uniform downstream condition reduces any forces due the system asymmetry. The experiments were conducted under non-cavitating conditions of the inducers.

(iii) to investigate the effects of inlet flow modification on the lateral and rotordynamic forces on a non-cavitating inducer. In particular, the effects of inlet shear flows will be studied. The effect, on the lateral force, due to a 180° bend upstream of the inducer will also be investigated.

(iv) to study the effect of cavitation on inducer rotordynamic forces for various cavitation numbers and flow coefficients.

The results of the various experiments conducted to achieve these goals are presented in subsequent chapters.

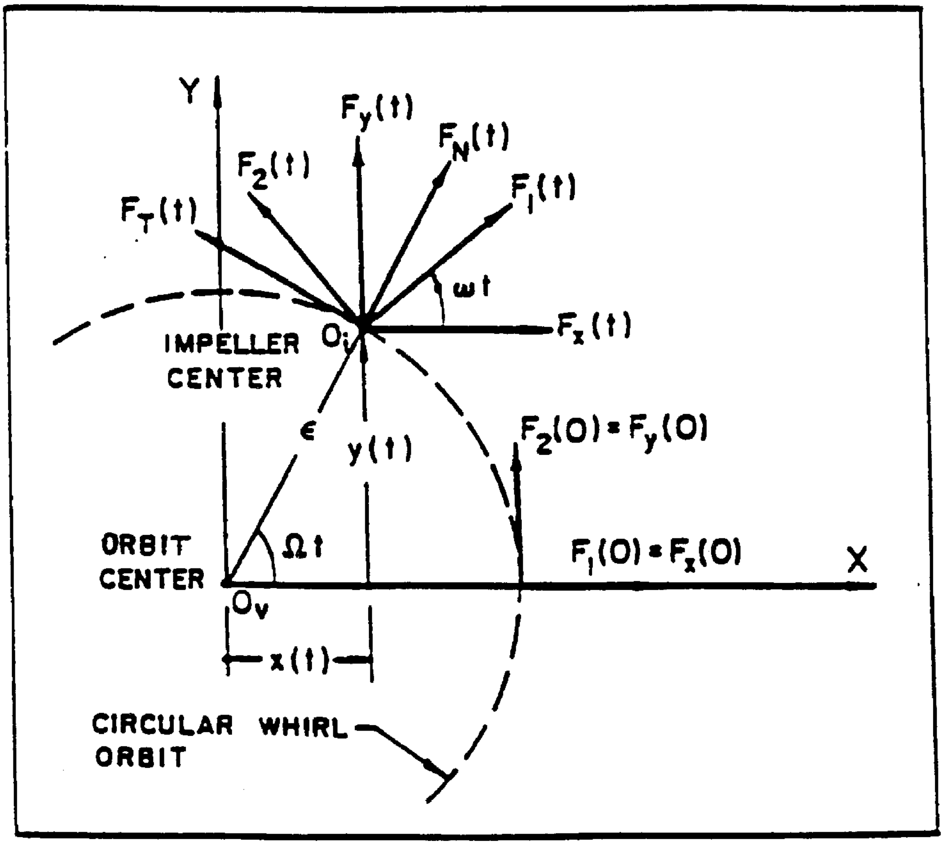

Figure 1.1 Schematic representation of the inducer forces in the rotating dynamometer frame (as F_1, F_2), in the laboratory frame (as F_x, F_y) and in the local polar coordinate frame (as Fn, Ft).

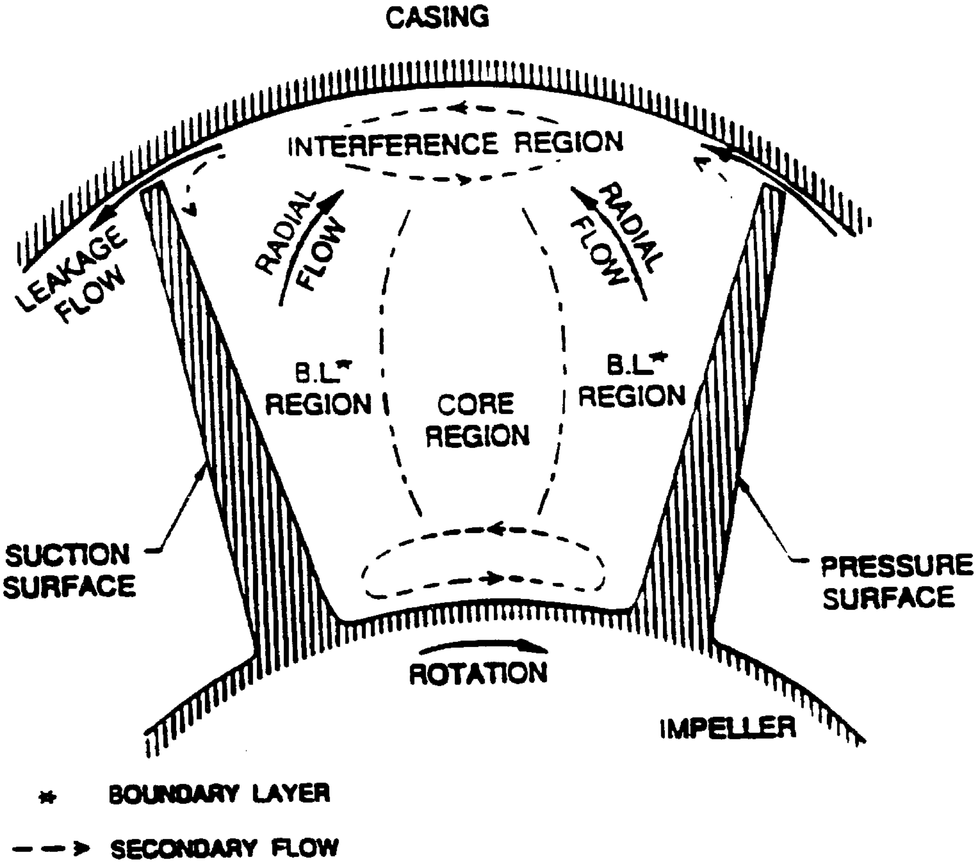

Figure 1.2 Internal flow in the blade passage area as postulated by Lakshminarayana (1972, 1981).

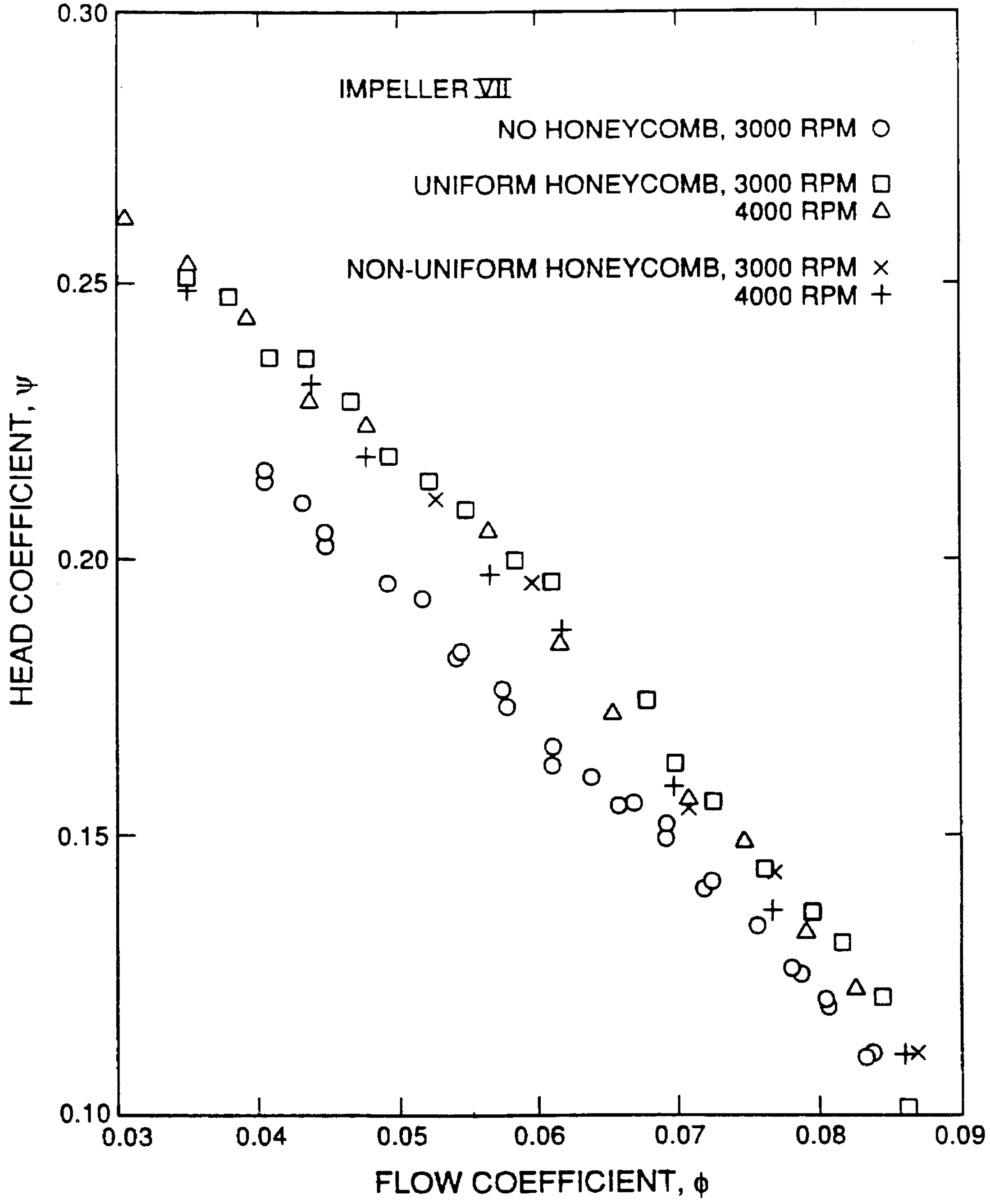

Figure 1.3 The head-flow coefficients of a 9^{o} inducer with and without honeycomb sections at the inlet (from Del Valle et al. 1990).

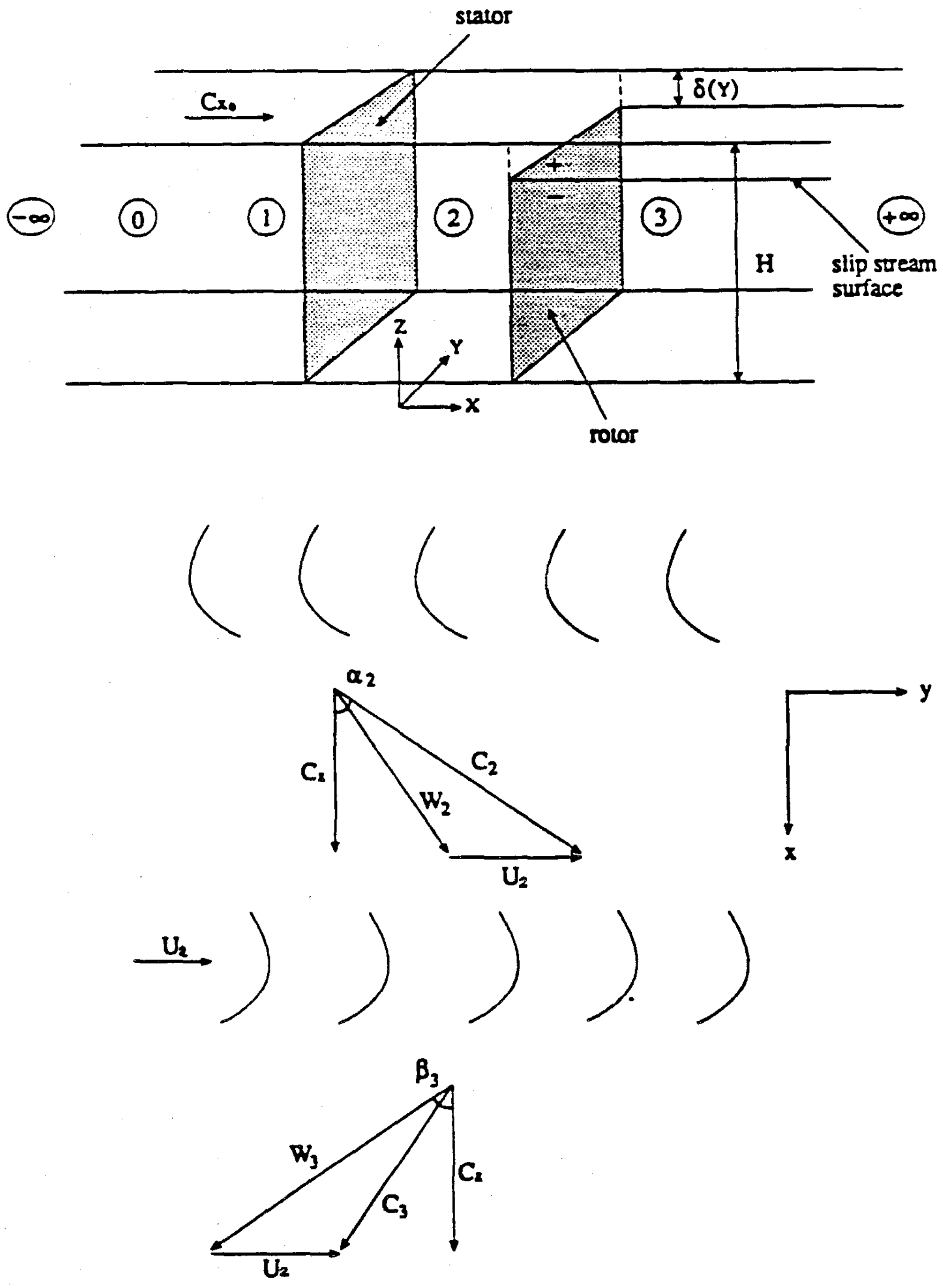

Figure 1.4 Actuator disk analysis of turbine flow and blade angles (From Martinez-Sanchez and Jaroux 1992).

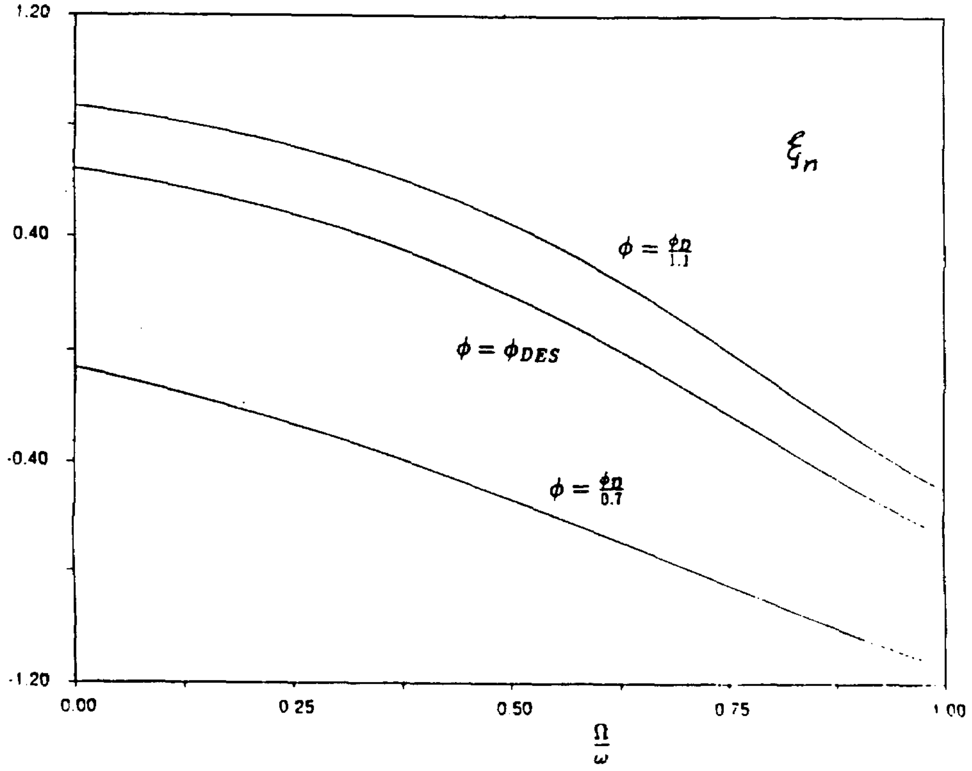

Figure 1.5. Alford coefficient as a function of whirl frequency ratio (α_2=70°, β_2=60°, solidity=0.756, ε/H=0.0113, ϕ(design)=0.58; from Martinez-Sanchez and Jaroux 1992).

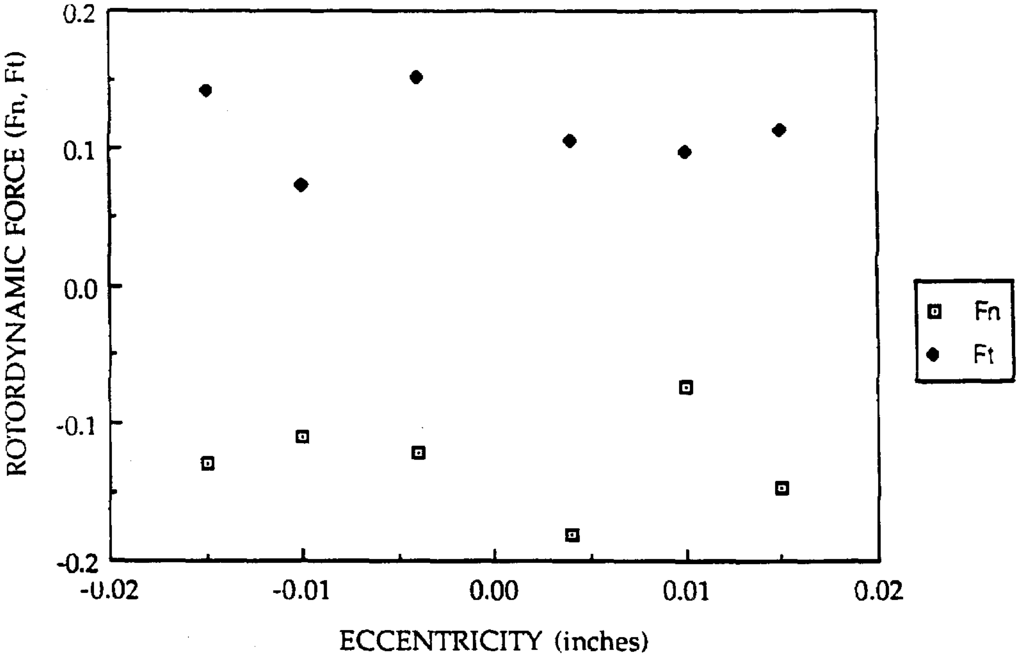

Figure 1.6. Non-dimensionalized normal and tangential forces on a turbine for static offsets of the rotor at ϕ=0.58 (from Martinez-Sanchez and Jaroux 1992).

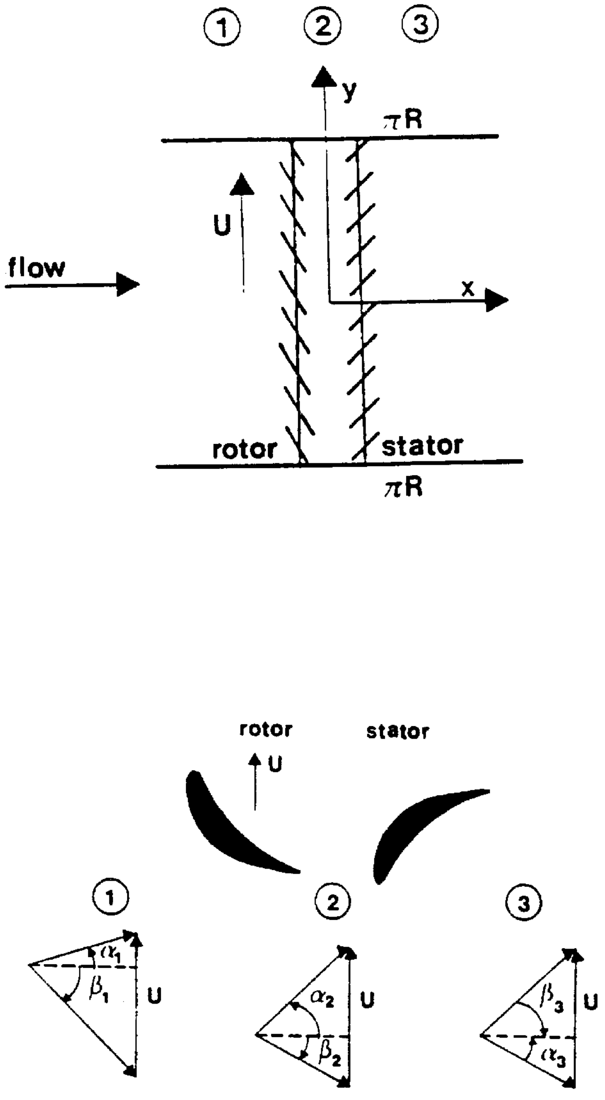

Figure 1.7. Actuator disk analysis of flow in axial flow compressors and blade angles (from Colding-Jorgensen 1992).

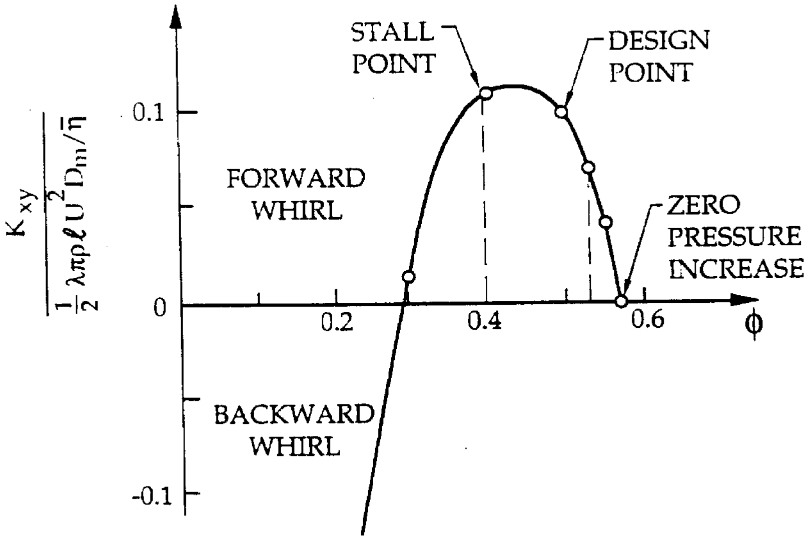

Figure 1.8a The variation of the cross-coupled stiffness coefficient with flow coefficient (from Colding-Jorgensen 1992).

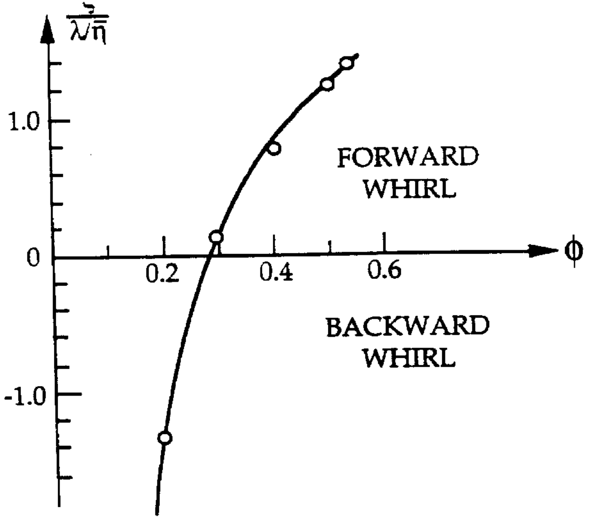

Figure 1.8b The Alford constant as a function of flow coefficient (from Colding-Jorgensen 1992).

CHAPTER 2

EXPERIMENTAL APPARATUS

2.1 THE ROTOR FORCE TEST FACILITY

The experimental work described in this thesis was conducted at the Rotor Force Test Facility (RFTF) at the California Institute of Technology. This section briefly outlines the main components and features of the facility. Further details of the facility can be obtained from Jery (1986) and Franz (1989). A schematic of the facility is shown in figure 2.1. This facility is primarily a pump loop that is closed to the atmosphere and uses water as the working fluid. The facility is equipped with various devices useful in the testing of pumps, but for the purposes of the current work only the relevant components are explained. The pump impeller (or in this case the inducer) is mounted within the loop and is the primary source of the recirculating flow in the loop. Secondary boosting of flow can also be achieved by including a boost pump in the system (the boost pump used for some of the experiments is a Byron-Jackson pump; details of the pump characteristics can be found in Karyeaclis et al. 1989). The impeller is mounted on a force dynamometer (described below), which in turn is mounted on an eccentric drive mechanism. This eccentric drive mechanism is the key component in the system that allows the impeller to be mounted eccentric to the centerline of the system. It also allows the eccentric impeller to whirl in a circular orbit. The impeller rotation and the circular motion in the whirl orbit are achieved using separate DC motors.

The inducer installation in the system is shown in figure 2.2. The inducer is mounted on a rotating flow deflector, which in turn is mounted on a spindle.

The spindle is mounted on the rotating force dynamometer. The inducer housing (stationary) was made of aluminum and hard anodized. This stationary housing was mounted on the front cover plate of the test section. The average clearance between the housing and the inducer tip was maintained at 0.0508 cm (.020 in.). At the downstream end of the inducer, a cylindrical screen with a 30 percent opening was placed around the rotating flow deflector in order to impose a uniform boundary condition. This arrangement for the inducer installation was used for the rotordynamic force measurements. The rotordynamic force measurements were conducted with the eccentricity set to 0.0254 cm. As a result of this eccentricity the clearance between the inducer blade tip and the housing varies between 0.028 cm. and 0.079 cm. The downstream screen was removed for testing the effects of asymmetric downstream conditions on the inducer forces. The downstream asymmetry, inherent to the system, is shown in figure 2.3.

The inducer installation configuration was changed slightly for flow visualization experiments described in chapter 3. An extended hub and flow deflector made of aluminum was used for this purpose. This allowed the inducer to be placed inside a transparent lucite housing. The inducer installation for flow visualization experiments is shown in figure 2.4.

A modified lucite housing was made for the flow visualization experiments. The housing was polished to achieve a high degree of transparency, thereby allowing flow visualization on the inducer. The eccentricity of the whirl orbit was maintained at zero for the flow visualization experiments and the average clearance between the housing and the inducer tip was 0.0305 cm.

The flow rate in the system was varied using either a butterfly valve (see figure 2.1) or a "silent throttle valve". The latter valve uses a hydraulic servo-control mechanism to pressurize an elastomer with oil that throttles the flow through the "holes" in the elastomer. This valve was used mainly for cavitation experiments since the butterfly valve would cause unnecessary cavitation in the system. The system pressure was regulated by pressurizing the air bladder in the system (placed adjacent to the heat exchanger). The air bladder could also be used to create a partial vacuum in the system by lowering the pressure in the bladder to below atmospheric levels by connecting a vacuum pump. The pressure in the system could also be lowered to levels below atmospheric (for cavitation experiments) by connecting a vacuum pump to the system. The technique most effective in creating these low pressures was to apply suction from the vacuum pump to the top of the heat exchanger tank after creating a free surface inside the tank. It may be added that there also exists a de-aeration system in use that could reduce the air content in the water to about 3 ppm. Further details of this system has been documented by Franz (1989).

2.1.1 THE ROTATING DYNAMOMETER AND ITS CALIBRATION

A rotating force dynamometer is used in the RFTF to measure the dynamic forces acting on the inducers in a rotating frame. The details of the construction of the dynamometer can be found in Jery (1986). The dynamometer essentially consists of four posts on which 36 strain gages are mounted. The strain gages are arranged in nine wheatstone bridge configurations in such a manner as to measure all the six components of a generalized force matrix (i.e., the three components of forces and moments). At the start of the present research, two of these strain gages were damaged and were replaced by similar gages. The dynamometer was calibrated before force measurements were taken and the calibration was checked periodically. The dynamometer was first calibrated using a series of static weights along each generalized force component. Thus, corresponding to each generalized force matrix [F], a matrix of voltages [V'] was recorded. The force-voltage relationship was checked for linearity and the slope matrix [B] in the equation: [V'] = [B][F] was obtained. The inverse of the slope matrix, $[B]^{-1}$, was then obtained as the calibration matrix. Thus, the forces acting on the inducer were obtained from the product of the calibration matrix and the voltage signals from the dynamometer.

The dynamic calibration of the dynamometer was verified by dry runs of the inducer. When the inducer is rotated in air without whirl, the steady force measured by the dynamometer must equate the dry weight of the inducer. Furthermore, the recorded weight should not change with the rotational speed. Such a check was performed and the results are shown in figure 2.5a. The dry weight must be recorded as acting vertically downward (i.e., at an angle of -90^{o} in figure 1.1). This verification is shown in figure 2.5b. In addition, if the inducer is also whirled in an eccentric orbit, the normal force recorded (minus the dry weight) must equate the centrifugal force on the inducer. This check was also performed to verify the calibration and the results are shown in figure 2.6. Finally, the impeller-dynamometer combinations were found to have natural frequencies higher than 145 Hz in previous tests conducted (Franz 1989; Zhuang 1989; Guinzburg 1992). The shaft frequencies used for the current experiments were much lower. After the satisfactory completion of the static and dynamic calibration of the dynamometer, force data was obtained for the various experiments described in this thesis.

2.1.2 DATA ACQUISITION AND REDUCTION

The fundamental principles and equations representing the rotordynamic forces and coefficients were presented in section 1.3. In this section, the manner in which data is obtained from the dynamometer and processed is briefly presented. Further details can be obtained from Franz (1989). Figure 1.1 shows the various force components on a whirling impeller. The forces $F_1(t)$ and $F_2(t)$ are detected by the rotating dynamometer in a rotating frame. The dynamometer frame rotates at the shaft frequency, ω. The voltage signals from the force dynamometer are sent to an analog-to-digital (A/D) converter through a rack of signal conditioning amplifiers. The output from the A/D converter is recorded and processed on a personal computer. The uncertainty in the force data (obtained from repeated runs of the experiment) presented in this thesis is approximately ten percent. The data reduction process consists of expressing the forces in the dynamometer frame in terms of the fixed reference frame (X,Y) and obtaining the lateral force and rotordynamic force components.

With reference to figure 1.1 the forces in the fixed reference frame can be obtained as:

$$F_x(t) = F_1(t)\cos(\omega t) - F_2(t)\sin(\omega t)$$

$$F_y(t) = F_1(t)\sin(\omega t) + F_2(t)\cos(\omega t). \qquad (2.1)$$

The expressions for $F_x(t)$ and $F_y(t)$ are then substituted in the equation (1.1):

$$\begin{bmatrix} F_x \\ F_y \end{bmatrix} = \begin{bmatrix} F_{ox} \\ F_{oy} \end{bmatrix} + \frac{\varepsilon}{r_2} \begin{bmatrix} A_{xx} & A_{xy} \\ A_{yx} & A_{yy} \end{bmatrix} \begin{bmatrix} \cos(\Omega t) \\ \sin(\Omega t) \end{bmatrix}$$

to yield:

$$F_1(t)\cos(\omega t) - F_2(t)\sin(\omega t) = F_{ox} + \frac{\varepsilon}{r_2}\left(A_{xx}\cos(\Omega t) + A_{xy}\sin(\Omega t)\right)$$

$$F_1(t)\sin(\omega t) + F_2(t)\cos(\omega t) = F_{oy} + \frac{\varepsilon}{r_2}\left(A_{yx}\cos(\Omega t) + A_{yy}\sin(\Omega t)\right). \quad (2.2)$$

The components of the steady force are obtaining by time averaging over several cycles of a reference frequency, ω/J. The electronic motor controls enable the main motor to rotate at J × ω/J and the whirl motor rotates at I × ω/J. I and J are integers and can be varied to generate various whirl frequency ratios (I/J). If NCYC represents the number of cycles over which data is taken (typically NCYC=256), then the total time period is denoted by T = NCYC × J/ω. The components of the steady force are therefore obtained as:

$$F_{ox} = \frac{1}{T}\int_0^T \left\{F_1(t)\cos(\omega t) - F_2(t)\sin(\omega t)\right\}dt$$

and $$F_{oy} = \frac{1}{T}\int_0^T \left\{F_1(t)\sin(\omega t) + F_2(t)\cos(\omega t)\right\}dt. \quad (2.3)$$

The components of the hydrodynamic force matrix $[A]$ are obtained by multiplying equations (2.2) by cos(Ωt) or sin(Ωt) and averaging over time as follows:

$$\begin{aligned} A_{xx}\frac{\varepsilon}{r_2} &= \frac{2}{T}\int_0^T \left\{F_1(t)\cos(\omega t)\cos(\Omega t) - F_2(t)\sin(\omega t)\cos(\Omega t)\right\}dt \\ &= \frac{2}{T}\int_0^T \frac{1}{2}\{F_1(t)\cos(\omega - \Omega)t + F_1(t)\cos(\omega + \Omega)t \\ &\qquad - F_2(t)\sin(\omega + \Omega)t - F_2(t)\sin(\omega - \Omega)t\}dt \end{aligned} \quad (2.4a)$$

$$A_{yx}\frac{\varepsilon}{r_2} = \frac{2}{T}\int_0^T \left\{F_1(t)\sin(\omega t)\cos(\Omega t) + F_2(t)\cos(\omega t)\cos(\Omega t)\right\}dt$$

$$= \frac{2}{T}\int_0^T \frac{1}{2}\{F_1(t)\sin(\omega+\Omega)t + F_1(t)\sin(\omega-\Omega)t$$

$$+F_2(t)\cos(\omega-\Omega)t + F_2(t)\cos(\omega+\Omega)t\}dt \qquad (2.4b)$$

$$A_{xy}\frac{\varepsilon}{r_2} = \frac{2}{T}\int_0^T \{F_1(t)\cos(\omega t)\sin(\Omega t) - F_2(t)\sin(\omega t)\sin(\Omega t)\}dt$$

$$= \frac{2}{T}\int_0^T \frac{1}{2}\{F_1(t)\sin(\omega+\Omega)t - F_1(t)\sin(\omega-\Omega)t$$

$$-F_2(t)\cos(\omega-\Omega)t + F_2(t)\cos(\omega+\Omega)t\}dt \qquad (2.4c)$$

$$A_{yy}\frac{\varepsilon}{r_2} = \frac{2}{T}\int_0^T \{F_1(t)\sin(\omega t)\sin(\Omega t) + F_2(t)\cos(\omega t)\sin(\Omega t)\}dt$$

$$= \frac{2}{T}\int_0^T \frac{1}{2}\{F_1(t)\cos(\omega-\Omega)t - F_1(t)\cos(\omega+\Omega)t$$

$$+F_2(t)\sin(\omega+\Omega)t - F_2(t)\sin(\omega-\Omega)t\}dt. \qquad (2.4d)$$

Thus, the net lateral force on the inducer are obtained from the components *Fox* and *Foy* while the rotordynamic normal and tangential forces are obtained from the components of the matrix $[A]$ as described in equations 1.3 and 1.4.

2.2 INDUCERS USED FOR THE RESEARCH

Three inducers were used for the current research. Two of these were unshrouded and one was a shrouded inducer. These inducers were of a simple helical design, with swept back leading edges. The blade angle at the tip (β_t) of the unshrouded inducers were 9^o and 12^o and will be referred throughout this text as **inducer VII** and **inducer IX** respectively. The shrouded inducer was designed with a β_t of 12°. The typical blade profile of these inducers is shown in figure 2.7.

2.2.1 THE 9° UNSHROUDED INDUCER

Inducer VII has been used earlier such as in the tests reported by Arndt and Franz (1986) and by Del Valle et al. (1992). This inducer is made of stainless steel and is three-bladed, with a constant pitch of 15.42 cm per revolution. The blade angle (9°) is the angle between the relative velocity vector and the tangential direction. The tip radius, r_2, of this inducer is 5.06 cm (1.99 in.). The solidity (s), defined as the ratio of the blade chord to the circumferential blade spacing, for this inducer is 1.45. (The blade spacing (S) used here is defined as $2\pi r_2$/no. of blades). The hub/tip ratio is 0.4 and the sweep-back angle of the leading edge is 69°. The axial blade length of this inducer is 2.41 cm. The performance characteristics of this inducer (without a downstream screen described in chapter 5) is shown in figure 2.7. This inducer has been used for flow visualization experiments and for the measurement of rotordynamic forces (due to flow distortions and cavitation).

2.2.2 THE 12° UNSHROUDED INDUCER

Inducer IX was designed and fabricated for the current research for studying the effects of changing the blade angle on the inducer forces and the internal boundary layer flows. The essential characteristics of this inducer are the same as that of inducer VII except that the blade angle is 12°. The solidity was increased to 1.75 and the helix lead was changed to 6.76 cm per revolution. The axial length of this inducer is 3.86 cm. The other physical characteristics of this inducer are the same as inducer VII. The performance characteristics of this inducer is shown in figure 2.8. The inducer was made of aluminum and was machined at the Mechanical Engineering machine shop at Caltech. A drawing of this inducer is shown in figure 2.9a. The inducer was machined using a milling machine. The aluminum stock was mounted on an indexing head mechanism designed to produced the given lead. Figure 2.9b shows the machining process and the indexing head. This inducer was used in the flow visualization experiments and in some measurements of the lateral forces on inducers.

2.2.3 THE 12° SHROUDED INDUCER

The shrouded inducer was used to study the tip clearance leakage flows in inducers and the generation of upstream swirling backflows. The design of the shrouded inducer was essentially the same as that of inducer IX except that the tip radius was decreased to 4.855 cm (3.83 in.) in order to accommodate a shroud of thickness 0.19 cm. The shroud was made of lucite and polished to a desired transparency to allow flow visualization. The shroud length was 5.18 cm. The hub/tip ratio for the shrouded inducer was changed to 0.42, while the solidity was kept constant. The other physical characteristics of this inducer are the same as inducer IX. The performance of shrouded inducer is compared to that of the unshrouded inducer in figure 2.8. The shrouded inducer was also machined at the Mechanical Engineering machine shop at Caltech using a procedure similar to that used for machining inducer IX. The shrouded inducer was used only for the purposes of flow visualization and not for force measurements. Table 2.1 summarizes the characteristics of these inducers.

2.3 FLOW VISUALIZATION TECHNIQUES

The boundary layer flows on the inducer blade surfaces and the hub were studied using flow visualization. The boundary layer flows on the rotating shroud of the shrouded inducer and the stationary housing used (both for shrouded and unshrouded inducers) were also studied. The flow visualization methods used are described below.

2.3.1 TUFTS

Tufts used for flow visualization were made of cotton thread about 1-1.5 cm. in length. The tufts were glued to the surfaces using epoxy resin and checked to ensure motion in all directions. The tufts along the inducer blade surfaces were placed about 1 cm. apart in both the radial and the tangential directions. The first set of tufts near the leading edge were placed 0.45 cm from the edge on both the suction and pressure sides. On the stationary lucite housing, tufts were placed at three axial locations upstream; the first set at 2.47 cm., the second set at 6.8 cm. and the third set at 10 cm from the inducer inlet plane. Each of these sets consisted of tufts placed circumferentially at 90° intervals. These tufts were used in determining the onset of the upstream swirling backflow. Tufts were also mounted on the hub at various axial locations along the blade passages, and a minimum separation of 1 cm. was maintained in order to prevent the tufts from getting entangled.

The inducer was run at various flow coefficients at a constant rotational speed (2000 rpm). The boost pump was used in the system to achieve flow coefficients above design. A stroboscope was used to observe the direction of the tufts on the blade surfaces by synchronizing it with the shaft rotation. The results of these tests were recorded using a video camera synchronized with the shaft rotation and also by still photographs. These results are described in chapter 3.

Although tufts provide a fairly effective means of visualizing the relative flow, there are also some drawbacks of this method. The tufts are usually unsteady because of the flow and do not clearly indicate whether the flows remain attached to the blade surfaces because the tuft size and stiffness affects their alignment. In addition, to get a continuous picture of the flow over the entire surface, several tufts must be used which in turn can cause them to get entangled. In order to overcome these problems, a paint dot method was used to visualize the flow and is described below.

2.3.2 PAINT DOT TECHNIQUE

This technique uses drops of oil paint mixed with linseed oil, placed at various locations (about 5 mm apart) on the surfaces of the blade, hub and housing. The paint-linseed oil mixture is made to obtain a desired consistency such that the paint (i) does not come off the surface when in stationary water, and (ii) does not move due to the rotation of the inducer in air at 2000 rpm. The paint-oil mixture moves on the surface only due to the shear stress caused by the boundary layer motion of the fluid over the surface. The experiments were conducted for one flow coefficient at a time. After the results were recorded, the surfaces were cleaned and the experiment repeated for other flow coefficients.

After the paint dots were placed on the surfaces, the system was filled with water. The inducer was then brought up to speed (2000 rpm) using the open loop electrical motor control. By doing so, it was assured that the flow coefficient was held constant. The boost pump was not used in these experiments to avoid any sudden change in flow rate. In fact the boost pump was altogether removed from the system for these experiments in order to decrease the system resistance (and thus achieve higher flow coefficients close to design). When the speed of 2000 rpm was reached, the inducer was kept running for about 5 minutes. This allowed the paint to flow on the surfaces in the direction of the relative flow. The inducer speed was then slowly brought down to shut off. The system was then drained and the paint streaks clearly showed the imprints of the boundary layer flow on the surfaces. As the results (discussed in chapter 3) show, the paint dot technique turned out to be a very effective means of studying the boundary layer flows in inducers.

2.4 FLOW DISTORTION DEVICES

Flow distortion devices were used to study the effects of upstream disturbances on the lateral and rotordynamic forces in inducers. These devices are described in this section.

2.4.1 HONEYCOMB SECTIONS

Preliminary experiments on flow distortion effects on inducer lateral forces were conducted using two honeycomb screens placed about $2^1/_2$ inducer diameters upstream. The honeycomb sections had a linear variation of axial thickness (from 5.08 cm. at the bottom to 0.95 cm. at the top, figure 2.10). The two screens were placed with the vertical sides facing each other but separated by a distance of 2.54 cm. (see figure 2.10). The velocity profile created by the honeycomb is shown in figure 5.4. The honeycomb sections generated a shear flow, which, however, was not adequately strong to create any significant impact on the forces (detailed in chapter 5). This lead to the necessity of creating a stronger shear flow using screens, explained in the section below.

2.4.2 SCREENS

In order to create a stronger linear shear flow than the one produced by the honeycomb sections, a potential flow theory was used to design shear flow producing screens. The theory was adapted from a similar work done by Owen and Zienkiewicz (1957) to produce a uniform shear flow in a wind tunnel where a grid was design assuming a drag coefficient of one. For the current work, the actual drag coefficient was used and the details of the theory and the modifications are presented in appendix A. The screens consist of a distribution of holes (see figures 2.11a and 2.11b). The hole diameters are constant along each row but vary gradually along the vertical direction. The important parameters of the screen are given by the static pressure coefficient

$$K_o = \frac{p_u - p_d}{\frac{1}{2}\rho V^2}$$

(where p_u and p_d are the static pressures upstream and downstream of the screen and V is the mean velocity of the flow through the screen) and the parameter λ''. The parameter λ'' determines the slope of the linear shear flow through the equation: $v(y) = V + \lambda''(y-D_p/2)$ where D_p is the pipe diameter, v(y) is the velocity at each location (y) downstream of the screen.

Two screens were designed for the purposes of the current experimentation. Screen SC1 was designed with $K_o = 10.0$ and $\lambda'' D_p/V = 1.55$. Screen SC2 was designed with $K_o = 5.0$ and $\lambda'' D_p/V = 1.0$. The velocity profiles due to the screens are presented in chapter 5 (figure 5.7). Theoretically, SC1 was designed such that $v(D) = 7.3\ v(0)$ and SC2 was designed to obtain $v(D) = 3\ v(0)$.

The screens were mounted in the inlet ducting of the inducer at a distance of approximately $2^1/_2$ inducer diameters upstream. A stainless steel wire cloth ($\approx$48% opening; 18 openings per inch) and a uniform honeycomb section were placed downstream of the screen to prevent mixing (which would reduce the velocity differences). The arrangement is shown in figure 2.12.

2.4.3 UPSTREAM BEND

An upstream was also used as a flow distortion device for the current experiments. Two 90° bends were placed approximately 4.3 inducer diameters upstream in a horizontal plane (i.e., along the -X axis; see figure 2.13). The bend was constructed using straight PVC piping and 4 "elbows". The approximate dimensions of the bend are also shown in figure 2.13. The velocity profile due to the bend and the forces on the inducer are presented in chapter 5.

2.5. EXPERIMENTAL PARAMETERS

The experimental variables for the flow visualization were the flow coefficients and inducer geometry (shrouded and unshrouded). The flow distortion experiments used various kinds of flow distortion devices and consequently various inlet velocity profiles. The effect of varying the flow coefficient and the inducer rotational speed on the lateral forces was also investigated. For rotordynamic force measurements, the whirl frequency ratio and the flow coefficient were the important variables. In addition, for cavitation experiments, the cavitation number was also an important variable.

TABLE 2.1. CHARACTERISTICS OF INDUCERS USED FOR THE EXPERIMENTS

	UNSHROUDED INDUCERS		SHROUDED INDUCER
	VII	IX	
Blade angle at tip	9°	12°	12°
Blade tip dia.	10.12 cm	10.12 cm	9.71 cm
Hub/Tip ratio	0.4	0.4	0.42
No. of blades	3	3	3
Solidity	1.45	1.75	1.75
Blade chord	15.42 cm	18.57 cm	17.81 cm
Helix lead	5.04 cm/rev	6.76 cm/rev	6.76 cm/rev
Blade thickness	0.15 cm (tip) 0.2 cm (root)	0.15 cm (tip) 0.2 cm (root)	0.15 cm (tip) 0.2 cm (root)
Shroud thickness	—	—	0.19 cm
Shroud length	—	—	5.18 cm
Sweep back angle of leading edge (hub to tip)	69°	69°	69°

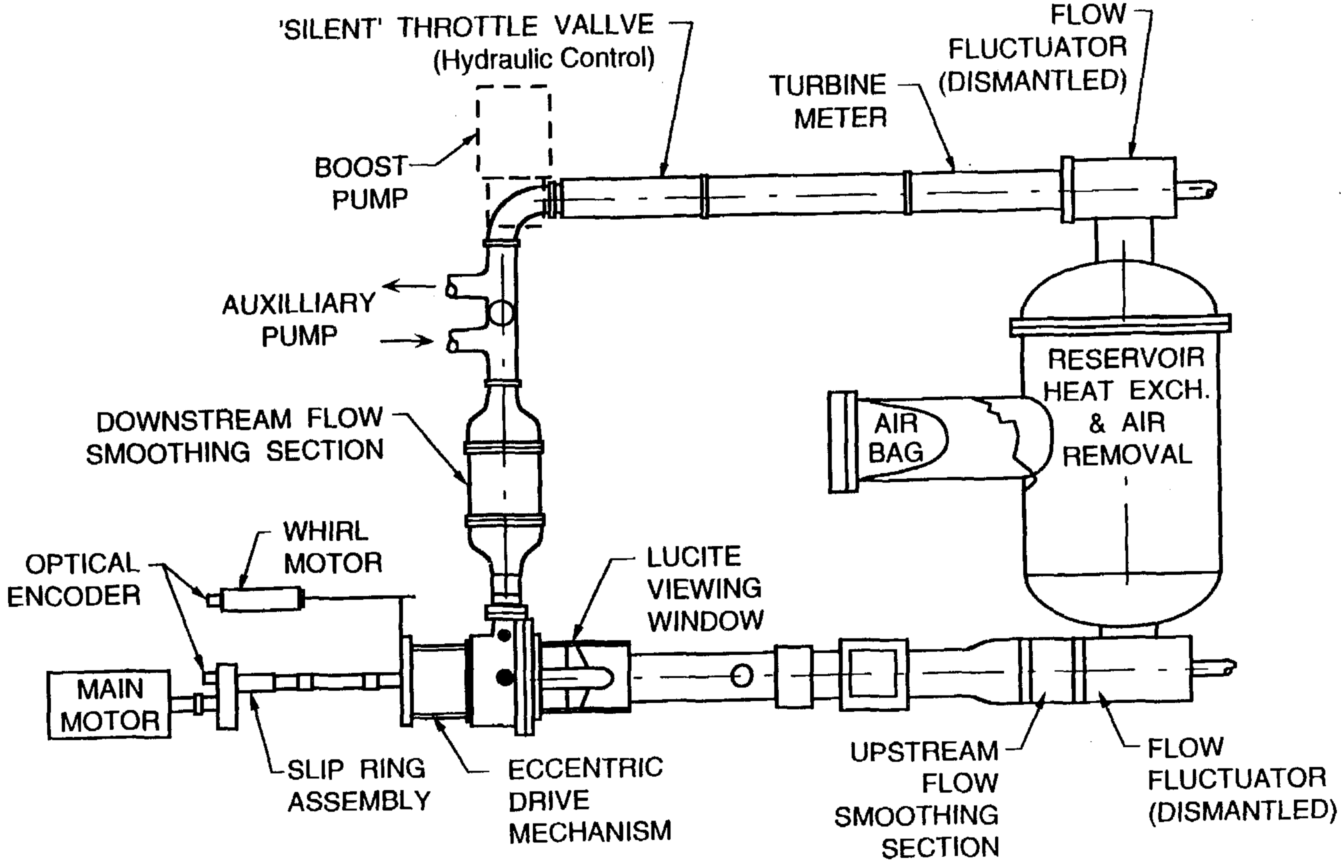

Figure 2.1 Schematic of the Rotor Force Test Facility

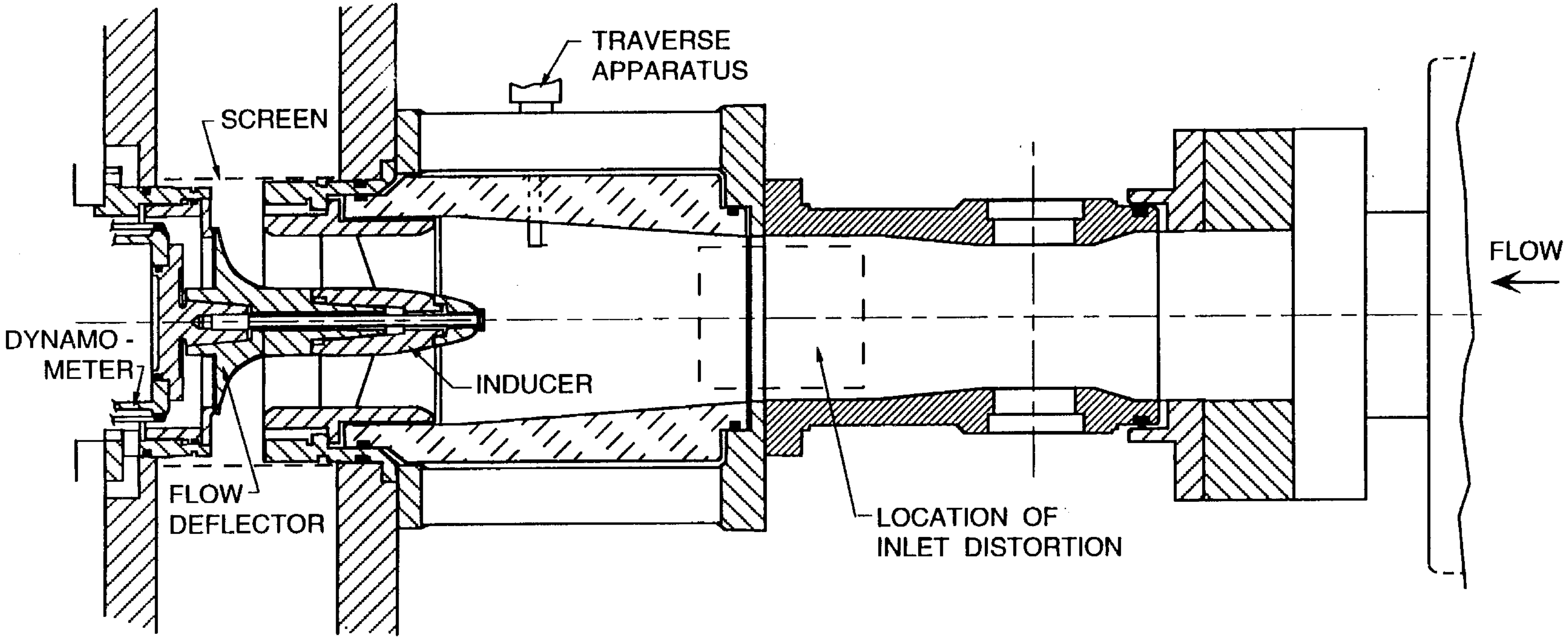

Figure 2.2 Inducer installation in the RFTF for force measurements

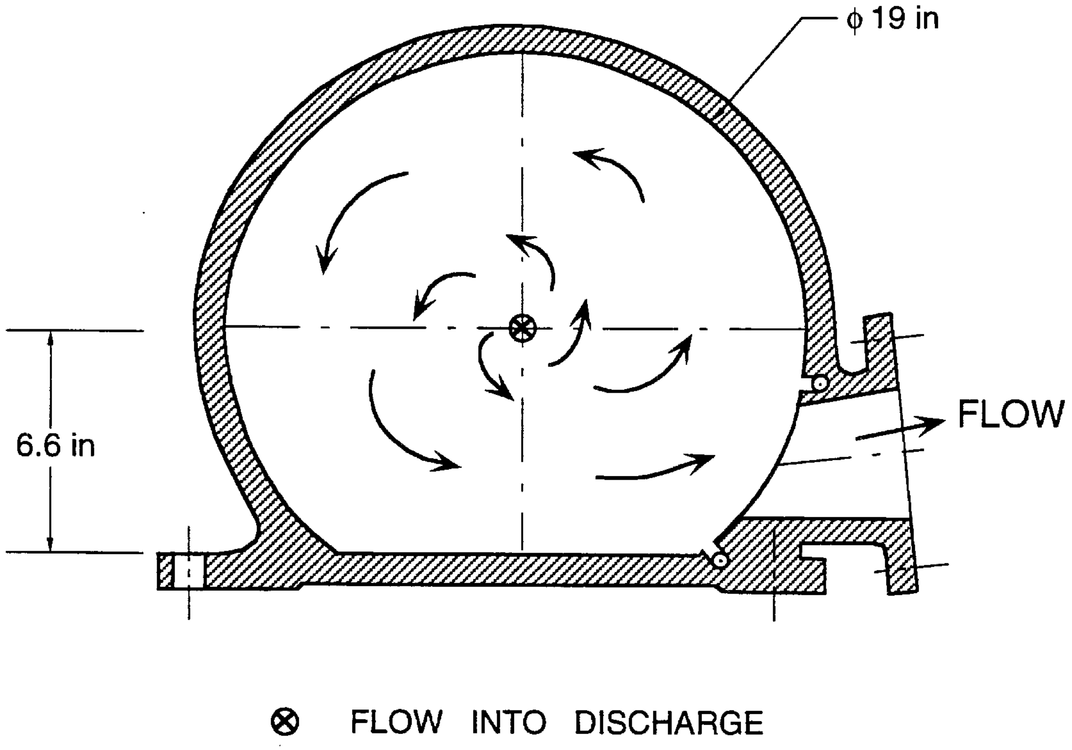

Figure 2.3 Downstream discharge asymmetry in the system

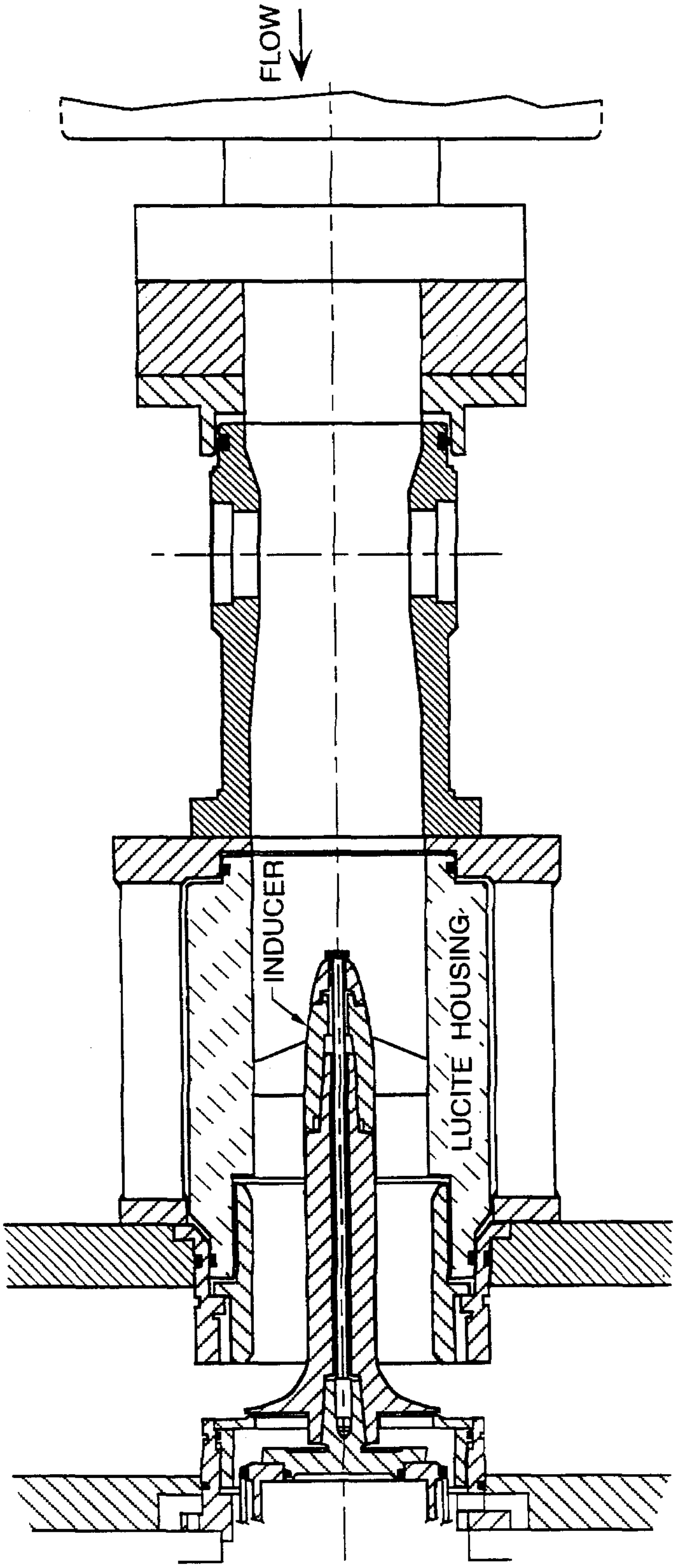

Figure 2.4 Inducer installation for flow visualization experiments

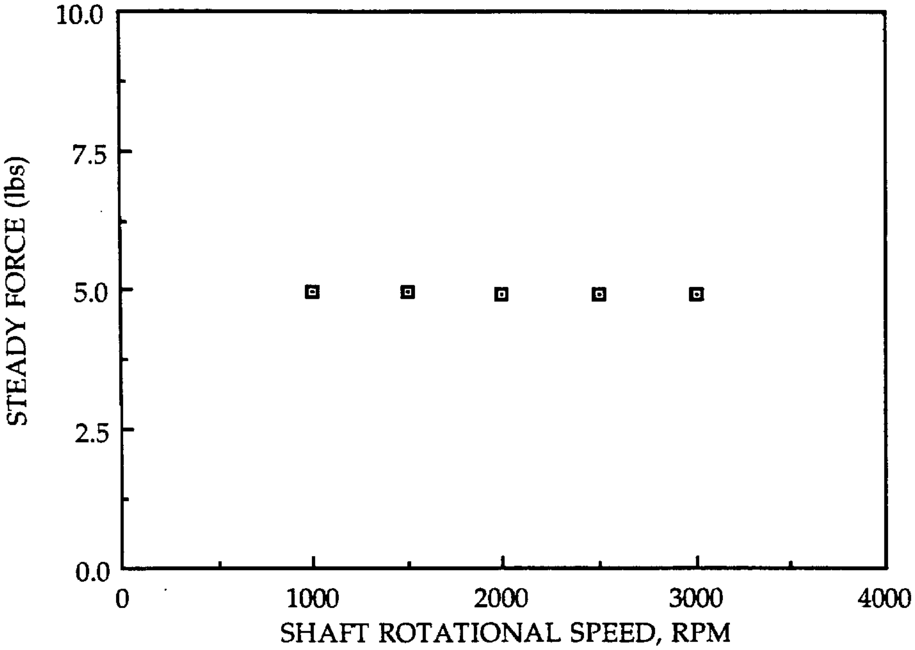

Figure 2.5a. Dry run data showing the dry weight of inducer VII as verification of dynamometer calibration.

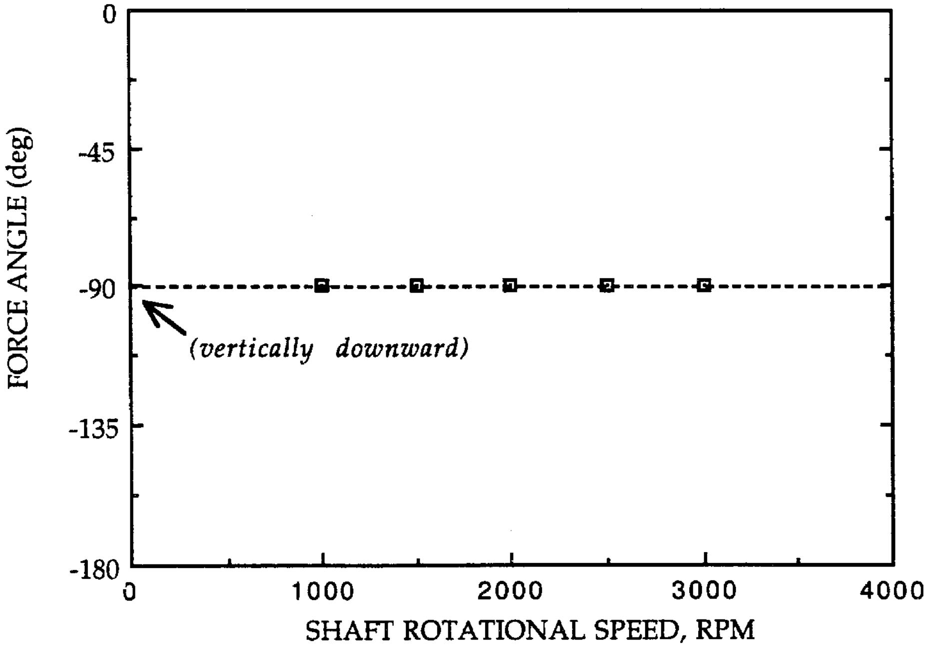

Figure 2.5b. Angle at which the dry weight of the inducer is recorded.

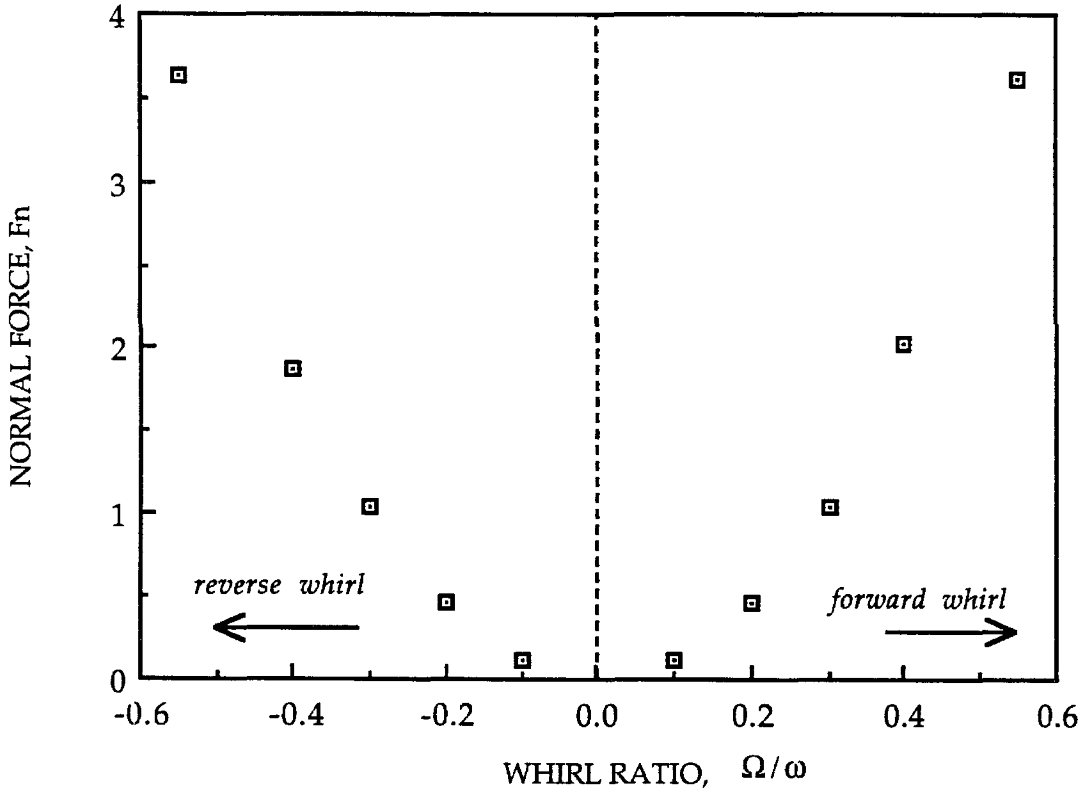

Figure 2.6. Plot of the non-dimensionalized normal force on inducer VII for a dry run at 3000 rpm, $\varepsilon = 0.0254$ cm.

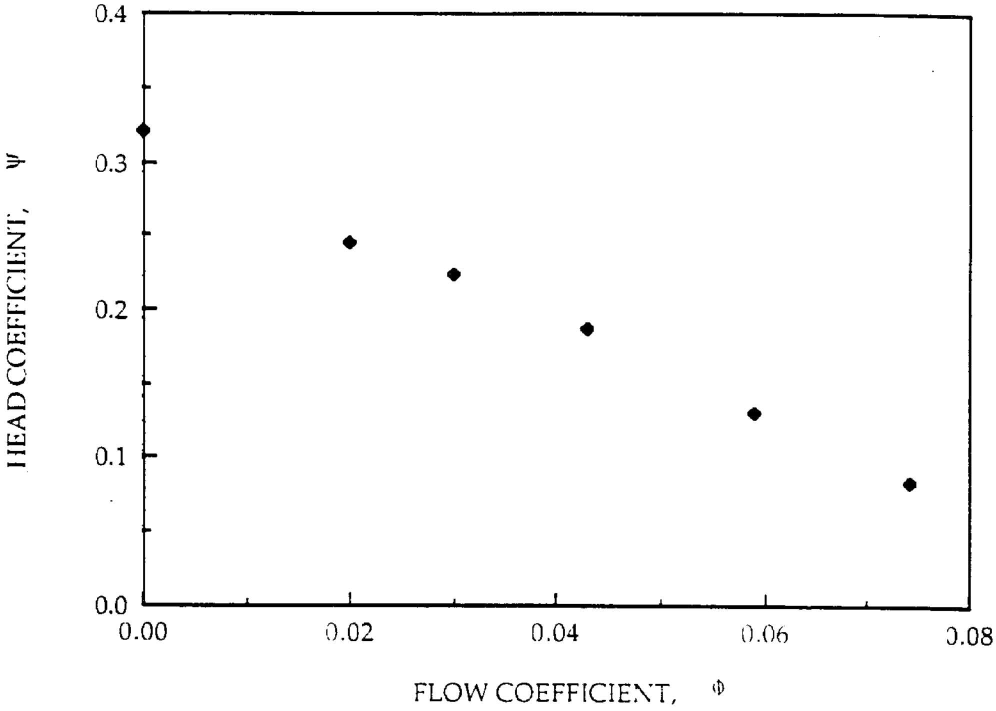

Figure 2.7. Performance characteristics of the 9° inducer at 2000 rpm.

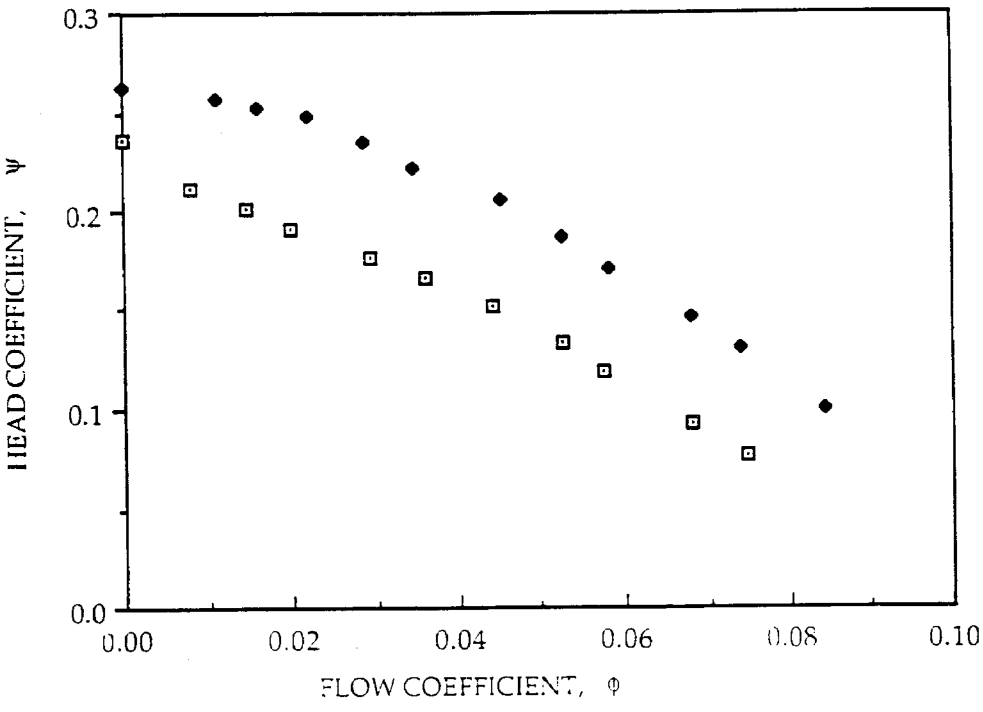

Figure 2.8. Performance curves for the 12° inducers at 2000 rpm
(▣ - shrouded; ◆ - unshrouded).

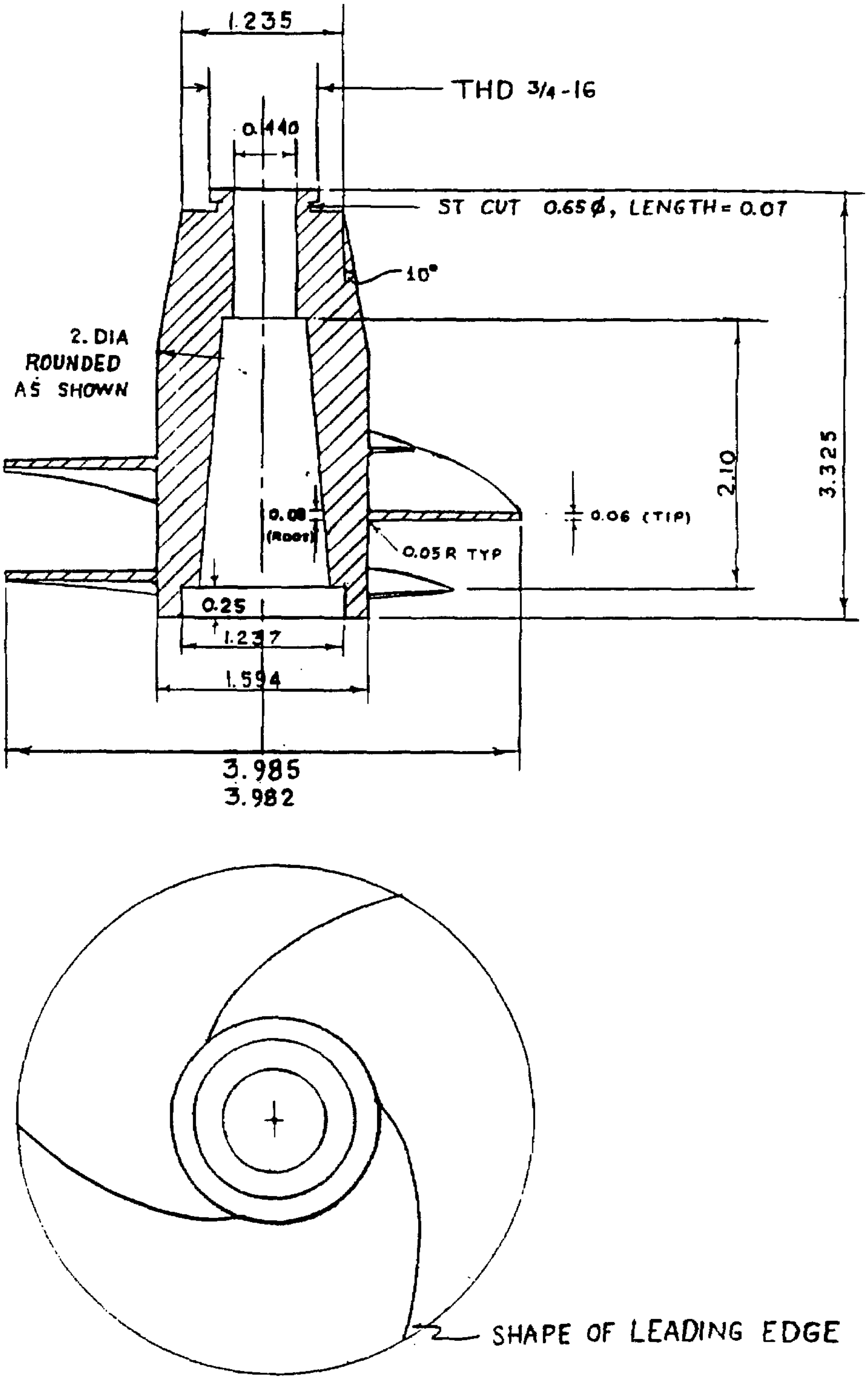

Figure 2.9a Drawing of inducer IX

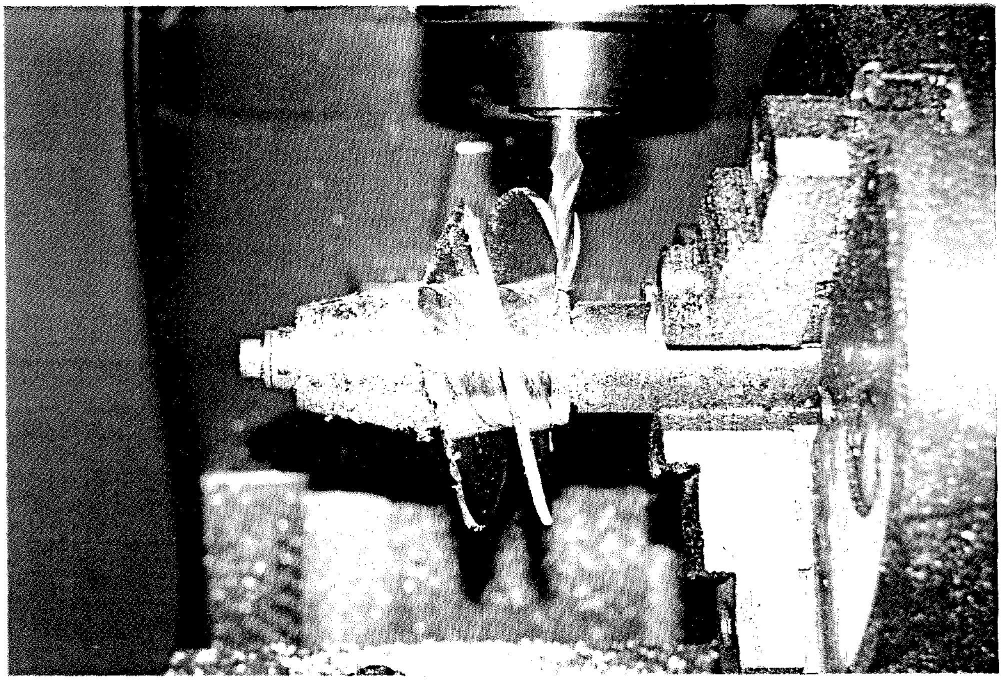

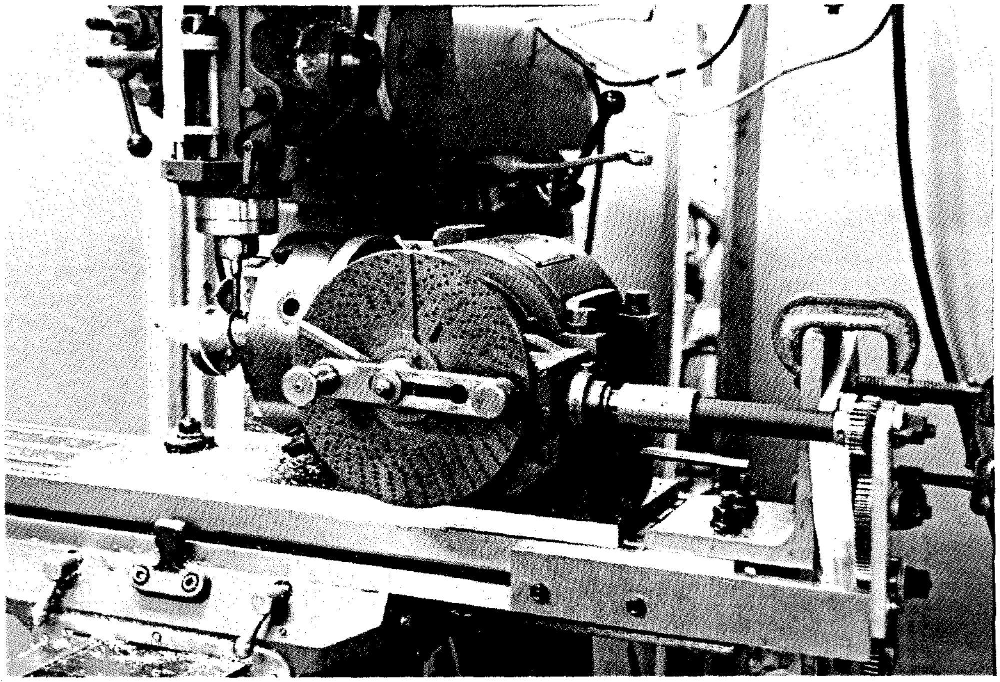

Figure 2.9b Photographs showing the machining of inducer IX and the indexing head.

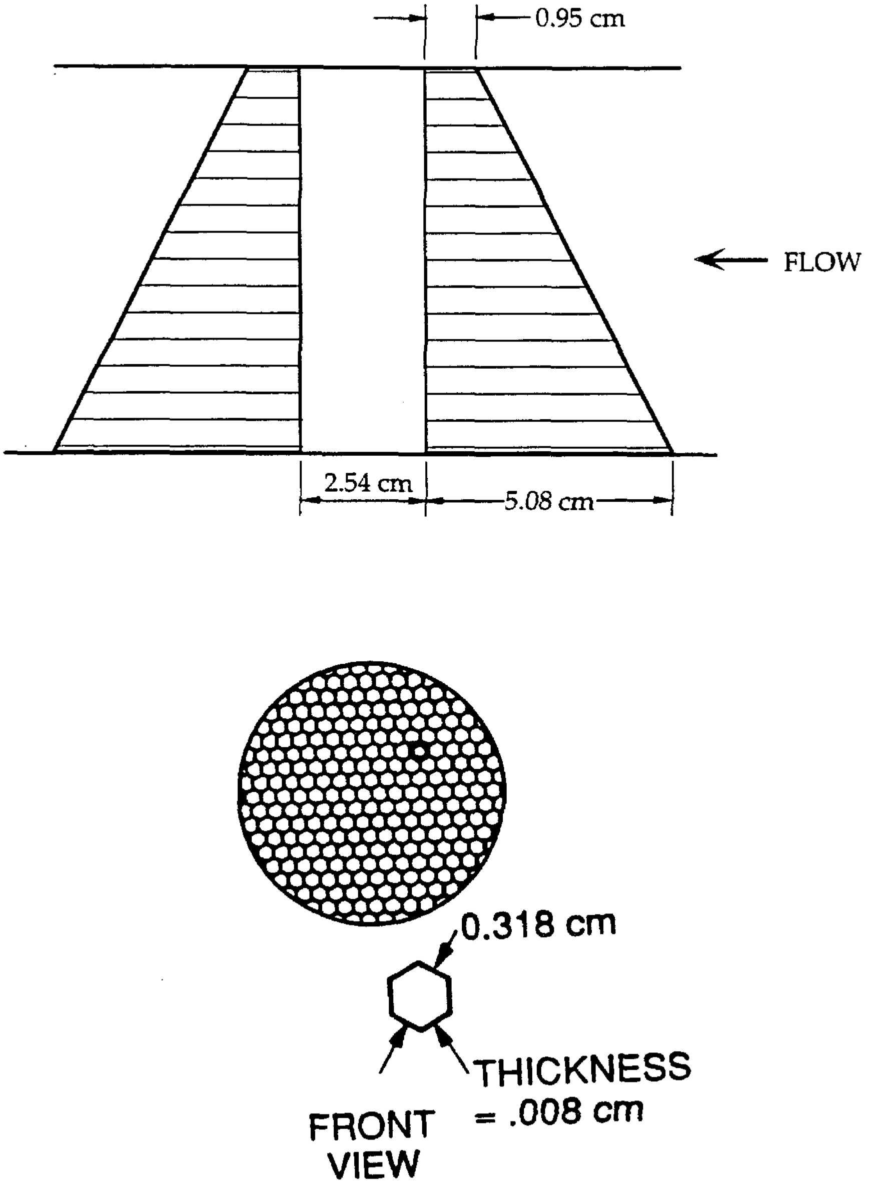

Figure 2.10 Geometry of the honeycomb sections used for the flow distortion experiments.

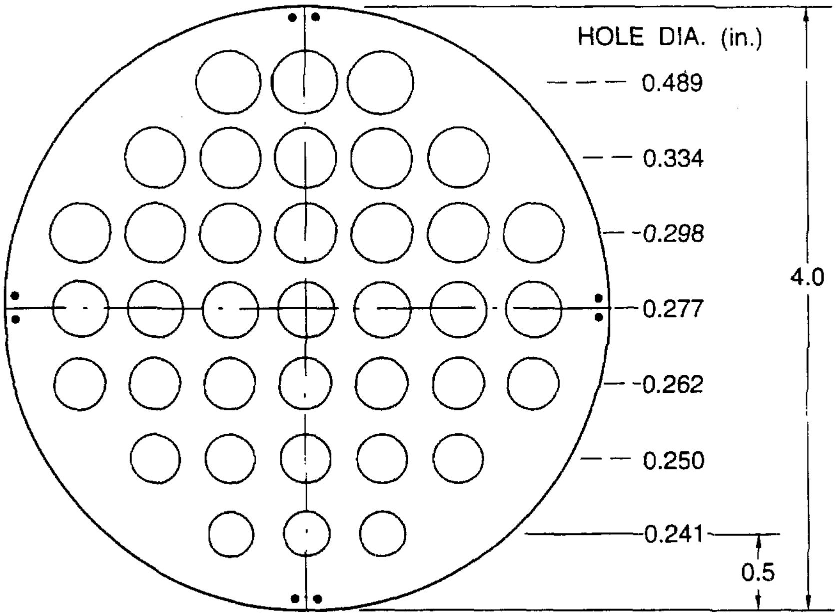

Figure 2.11a Screen SC1 used for the flow distortion experiments

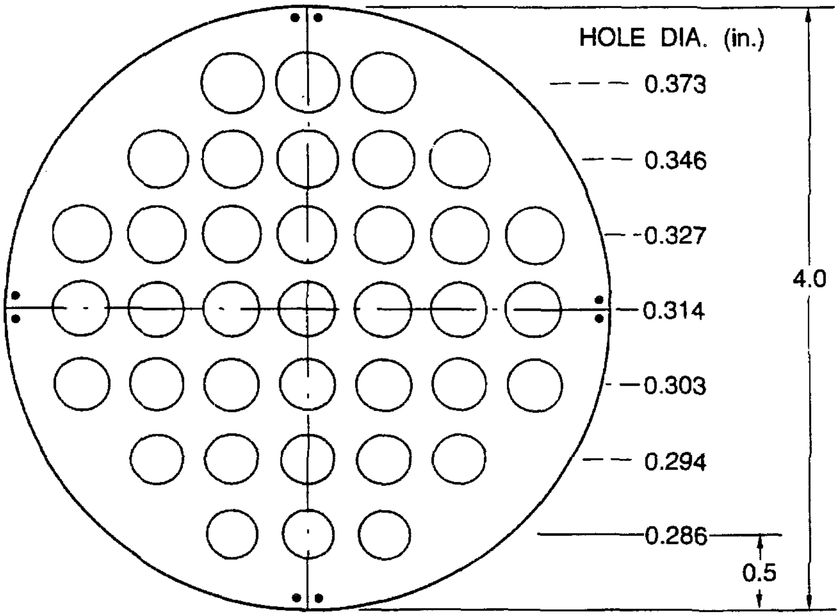

Figure 2.11b Screen SC2 used for the flow distortion experiments

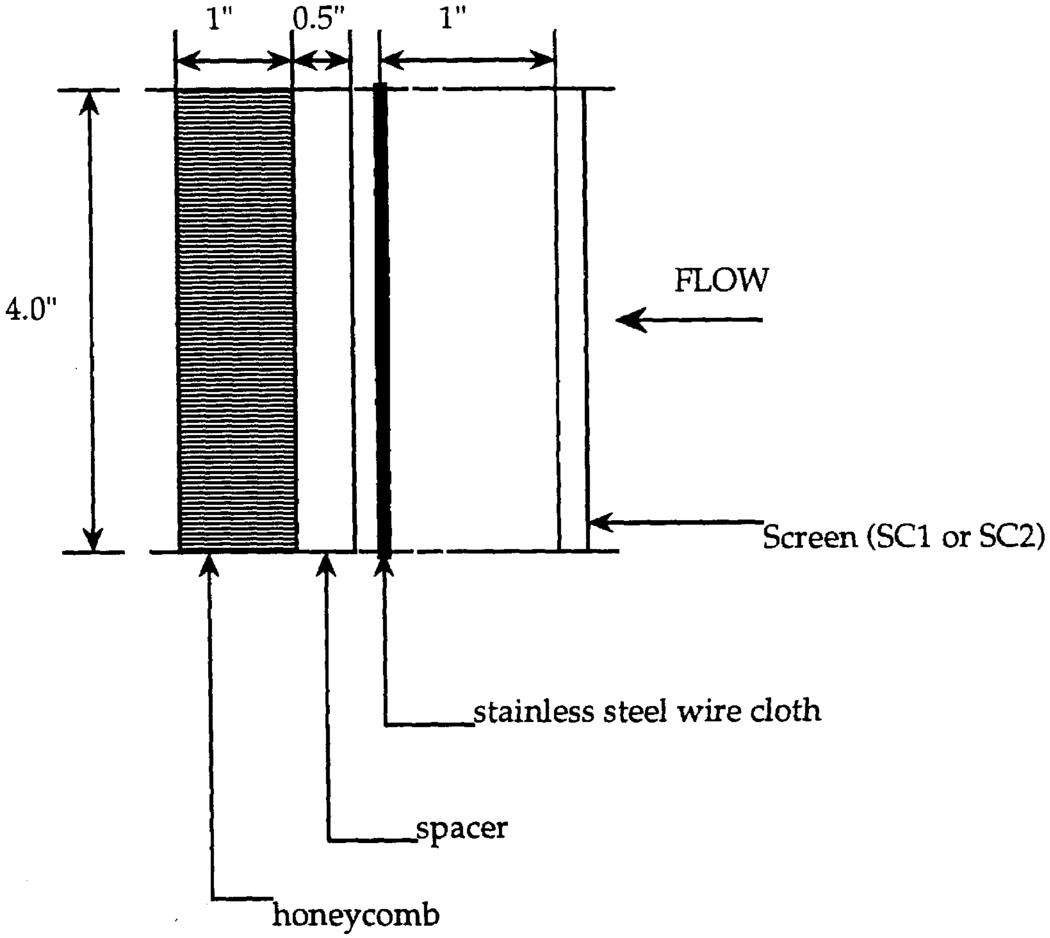

Figure 2.12. The inlet shear flow assembly showing the location of the screen (SC1 or SC2) along with a wire mesh and a uniform honeycomb section.

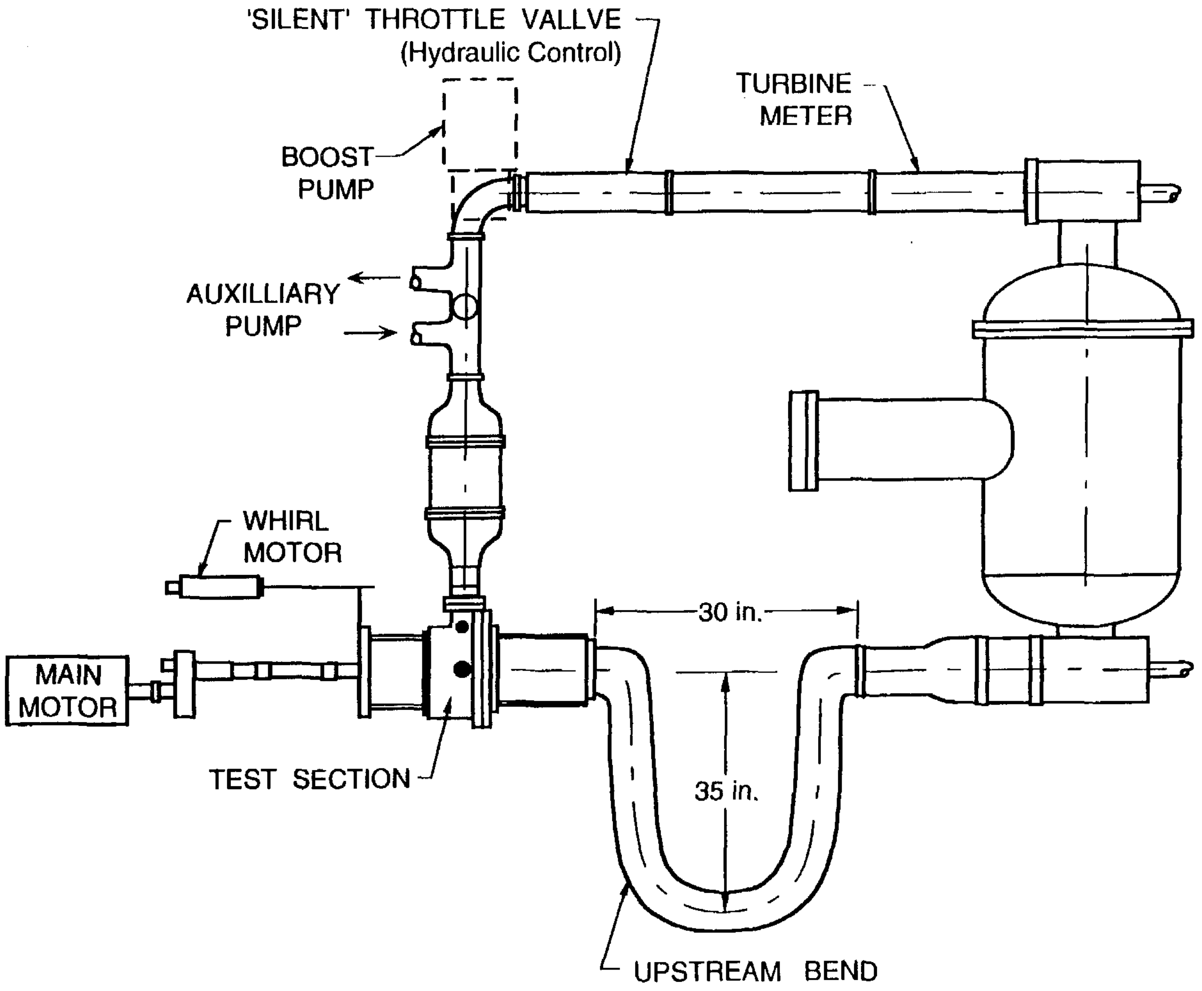

Figure 2.13 Schematic of the facility with the upstream bend installed.

CHAPTER 3

INTERNAL FLOWS IN AXIAL FLOW INDUCERS

Flow visualization techniques have been used to study the boundary layer flows on the blades, hub and housing of both unshrouded and shrouded inducers. The boundary layer flows were visualized using tufts and a paint dot technique which have been described in section 2.3. In this chapter, the results of these experiments are presented. The results not only show the boundary layer flows, but can also be used to infer the nature of the internal blade passage flows.

3.1 UNSHROUDED INDUCERS

The boundary layer flows on the blade surfaces, hub and housing of unshrouded inducers were visualized using tufts and paint traces. In the case of unshrouded inducers of the type used for the current experiments (i.e., three-bladed, helical inducers of constant pitch such as inducer VII and inducer IX), it was observed that the inception of upstream swirling backflow occurred at ~70% of the design flow (the nominal design flow of inducer VII is $\phi \approx 0.1$ and $\psi \approx 0.1$). This reversal was observed when the set of tufts nearest to the leading edge of the inducer changed direction (due to the influence of the upstream swirling backflow; at flow coefficients near design, these tufts were oriented in the direction of the mean flow, i.e., flowing downstream). As the flow coefficient was reduced further from the design value, it was observed that the tufts mounted on the hub downstream of the inducer also reversed direction. This reversal of flow downstream of the unshrouded inducers occurred at ~60% of the design flow. Tufts were thus useful in determining the flow coefficients at which flow reversals occur both upstream and downstream of the inducer. A more detailed description of these reverse flows were obtained from the paint dot technique, the particulars of which are given below in this section.

3.1.1 FLOW ON BLADE SURFACES

Tufts and paint dots on the blade surfaces (viz., the suction and the pressure surfaces) were useful in visualizing the directions of the relative flow. Experiments with the tufts indicated that the flow directions on the blade surfaces were approximately tangential for flow coefficients at the design value and higher. The tufts appeared to be well lined up in these cases. However, when the flow coefficient was gradually reduced below design, the tufts began to show the presence of a radial component in the flow. This occurred initially with the tufts nearest to the blade tip, then the tufts nearest to the hub and finally all across the blade surface (especially on the suction side) when the flow coefficient was continuously reduced. It was also observed that when the upstream swirling backflow developed, the tufts nearest to the blade tip reversed direction and were oriented in the direction of the tip clearance leakage flow. It was also noticed that the radial component of the flow on the suction side near the hub also increased with the inception of reverse flow downstream on the hub.

The observations of an increased radial component with decreasing flow rates is an important feature of the internal flows in these inducers. Similar observations were also reported by other researchers (e.g., Lakshminarayana 1972). The radial flows are associated with the three-dimensionality and the complexity of the internal flows. Experiments with paint traces have also yielded similar results. At flow coefficients below design, increased radial boundary layer flows have been observed by the paint traces. The extent to which the blade surface flows display a radial component can be measured by a limiting streamline angle (χ) made by the observed streamline on the blade surface relative to the tangential direction (Lakshminarayana 1972) and is indicated in figure 3.1. The paint traces left on the blade surfaces make it convenient to measure these angles for the inducers. Figure 3.2 shows a photograph of the paint traces showing the flow on the suction side of inducer IX at $\phi = 0.041$. The flow on the pressure side is shown in figure 3.3.

A typical measurement of these angles is shown in tables 3.1A and 3.1B at a flow coefficient $\phi = 0.083$ for the 12° inducer (inducer IX). At this flow coefficient, in addition to the upstream backflow, flow reversal downstream on the hub was also observed. The results show that the limiting streamline angles increase in magnitude from the leading edge to the trailing edge near the hub on the suction side. The value of χ at the blade tip is largest at the leading edge and is lower at the mid-chord and trailing edge (in fact χ is approximately constant from mid-chord to trailing edge at the tip) on both the suction and the pressure sides. At the mid-radius location, χ decreases gradually from the leading edge to the trailing edge on both the suction and the pressure sides. It is also seen that the value of χ from the mid-chord to the trailing edge are high near the hub (suction side). The paint dots also showed that there was a sharp decrease (about 40°) in χ near the trailing edge (suction side) at ~43% blade height. The large values of the limiting streamline angles close to the trailing edge are observed when re-entry of flow occurs in the blade passage area.

Visualization on the pressure side also shows large radial boundary layer flows. The values of χ are lower than those on the suction side (as also reported by Lakshminarayana 1972). However, the current results do not show much variation along the blade chord or along the radius except at the leading edge (where the radial component is large $\chi \approx 70^{\circ}$).

3.1.2 FLOW ON THE HUB

The paint dot technique was also used to examine the flow on the hub of the inducer especially in the blade passage region. The flow reverses downstream on the hub and it re-enters the blade passage region as seen by the traces on the hub surface (figure 3.4). This re-entrant flow continues on the hub until about mid-chord where it meets the fluid from upstream. This interaction causes the hub boundary layer flow to separate in the blade passage area. The paint traces of the re-entrant flow on the hub are also seen to move toward the suction side of the blade.

3.1.3 FLOW ON THE STATIONARY HOUSING

The flow on the stationary casing around the inducer was also studied using paint dots and tufts. Experiments using tufts confirmed that no leakage flow occurs when the inducer is operated at design or higher flow coefficients. At lower flow rates the tufts reversed direction indicating the presence of leakage flow. The paint traces on the housing represent the time-averaged absolute flow. The experiments revealed that downstream of the discharge plane of the inducer blades, the flow (on the housing) moved downstream along with a tangential component (in the direction of rotation; see figure 3.5) whereas upstream of this plane the flow moved upstream. This upstream component, in fact, is the reverse flow on the inducer. These experiments revealed the origin of the leakage flow in these axial flow impellers. This aspect is discussed below. Figure 3.6 is a photograph of the paint traces showing flow reversal on the housing of inducer VII at a flow coefficient of $\phi = 0.07$ (i.e. with incipient upstream backflow).

These experiments have confirmed that the leakage flow between the blades and the housing is indeed the agent of the upstream swirling backflow which was speculated by Acosta (1958) and Del Valle et al. (1991). The LDA measurements of Howard et al. (1987) in the blade passage area of an inducer at off-design do not show the presence of reversed flows within the blade passage area. It may be deduced from their results that leakage flows (between blade tip and housing) are the cause of the upstream backflow. The current experiments have found that the origin of this leakage flow is the discharge plane of the impeller. As the flow rate is reduced, the discharge pressure rises, until at a certain flow rate the adverse pressure gradient causes the low energy radial flow from blade passage to reverse direction in the tip clearance region. That this pressure gradient is indeed the major cause of the leakage flow is verified by the shrouded inducer. Thus the radial component of the velocity at the tip, in the case of unshrouded inducers, promotes this leakage flow. The radial flow may not necessarily be the cause for the leakage flow as has been suggested by Janigro and Ferrini (1973).

The onset of the downstream flow reversal does not seem to be coupled with the upstream reversal as mentioned by Acosta (1992). Acosta (1992) points out the dependence of the onset of upstream and downstream flow reversal on impeller geometry. The work reported by Tanaka (1980), for example, shows this to be true for mixed flow impellers also. Howard et al. (1987) have shown through their LDA measurements that the near hub axial velocity falls rapidly as the flow rate is reduced, contributing to hub stall. The current observations show that this can occur on the hub close to the trailing edge. The reduction of the axial velocity on the hub at the blade trailing edge together with the strong radial component could create an adverse pressure gradient at the discharge end causing the flow to reverse on the hub and re-enter the blade passage area. The re-entrant flow causes the flow coming from upstream along the hub to separate. This interaction may also be the cause of the secondary vortices in the axial direction observed by Lakshminarayana (1972) by smoke traces near the trailing edge of the inducer.

The existence of the radial component of flow on the blade surface at off-design flows is a well known fact to researchers in this area. Lakshminarayana (1972) has presented visualization studies indicating the existence of the radial component of the flow on the blades. Furthermore, Lakshminarayana (1978) has demonstrated the "shear pumping effect", due to the additional head rise caused by the tangential acceleration of the fluid as it moves in a radial path. This shows the importance of including centrifugal and Coriolis forces in the analysis of flows in inducers. Lakshminarayana (1978) states that the boundary layers cover the entire passage width and hence radial velocity occurs across the entire passage width.

The current experiments confirm that the flow on the suction side of the blade remains attached (at all off-design flow coefficients). In other words, the separation of flow as reported by investigators (Tanaka 1980) is not observed by us in axial flow inducers. The limiting streamline angles at the tip of the blade do not vary much along the blade (from leading edge to trailing edge) due to the interaction of the blade boundary layer with the boundary layer flow on the stationary housing. There is a strong radial component of the blade boundary layer flow near the hub close to the trailing edge. It may be speculated that this radial flow causes the downstream re-entry flow on the hub. The radial component decreases at about mid-blade height due to the interaction with fluid at larger radial locations and due to the effect of the stationary housing.

The interaction of the boundary layers on the blade surfaces, the hub and the housing all together determine the internal flow on the inducer at off-design conditions. From the current observations and the above discussion, we may infer that the blade passage area consists of secondary vortices in axial and tangential directions. Near the tip clearance region, the radial flows mix with the strong leakage flow and there may not occur radially inward flow in the blade passage area particularly near the tip.

3.2 SHROUDED INDUCER

A 12^o shrouded inducer was also used to visualize internal flow to further investigate the origin of upstream backflow. It also happened that the shroud affected the internal flow to some degree. For example, flow reversal was observed on the suction side of the blade near the tip causing upstream backflow to develop within the inducer (described below). The upstream backflow in shrouded inducers therefore consists of two components: (a) the discharge-to-suction leakage flow exterior to the shroud and (b) the backflow developed within the inducer.

3.2.1 FLOW ON THE BLADE SURFACES AND THE HUB

The boundary layer flow on the suction side and the pressure side of the blades showed pronounced radial flows in much the same way as in the unshrouded inducers. While the limiting streamline angles could not be measured accurately all across the blade (due to the presence of the shroud), they displayed the same characteristics as the unshrouded inducer, except that at the tip of the blade the values of the limiting streamline angles were close to zero (due to the presence of the shroud). However it was noticed that on the suction side of the blade near the tip, there existed a chordwise location where the flow reversed direction and started moving upstream near the tip (figure 3.7).

The reversed flow remains attached to the blade and shroud until it interacts with the fluid from upstream, when it leaves the blade and flows upstream along the interior of the shroud. Upon exiting the shroud, the fluid mixes with the leakage flow exterior to the shroud and forms part of the upstream swirling backflow. Figures 3.8a and 3.8b show the show on the interior of the rotating shroud for $\phi = 0.041$ (i.e., with strong upstream backflow and downstream re-entry flow).

The reversal point on the suction side of the blade depends on the extent to which backflow has developed and moves closer to the leading edge with decreasing flow rate and increasing backflow. The flow downstream (chordwise) of the reversal point continues to flow downstream. There is no other separation of flow on the blade. The leading edge flow remains attached to the blade surface under all conditions and has a large radial component (as in the case of the unshrouded inducer).

The flow on the pressure side also exhibits a radial component at off-design flow in much the same way as the unshrouded inducer. The radial component of velocity becomes small close to the shroud and is smaller than that on the suction side. Close to the leading edge the flow has a strong radial component of velocity (as in the unshrouded case). The flow on the pressure side of the blade of the shrouded inducer is shown in figure 3.9 for $\phi = 0.041$.

The flow on the hub is similar to that observed for unshrouded inducers. The downstream reverse flow on the hub re-enters the blade passage area and interacts with the upstream flow in the same way as in unshrouded inducers (figure 3.10).

3.2.2 FLOW ON THE STATIONARY HOUSING

The leakage flow exterior to the shroud is observed to originate at the discharge end of the rotating shroud. Downstream of this discharge plane, the flow moves downstream and upstream of this plane the flow moves upstream. This upstream component is the discharge-to-suction leakage flow exterior to the rotating shroud. The leakage flow also displays a tangential absolute velocity component in the direction of rotation of the inducer. In addition it is observed that when this leakage flow interacts with the reverse flow generated within the inducer, it results in an increase in the tangential velocity component of the upstream leakage flow. The leakage flow on the stationary housing of the shrouded inducer is shown in figure 3.11 at $\phi = 0.041$.

As described above the test results indicate that the upstream backflow observed in the case of a shrouded inducer at off-design flows consists of two components: (a) the discharge-to-suction leakage flow, and (b) separation of flow on the suction surface of the blade. While the leakage flow may be attributed to the adverse pressure gradient exterior to the shroud, the separation at the blades is not due to a change in the angle of attack at off-design flows as has been suggested by Toyokura and Kubota (1968). While the authors do point out that backflow originates inside the flow passage between two blades, they also state that the "slip of flow" to the pressure side of the blades can be regarded as a phenomenon similar to the separation of flow due to a large increase in the angle of attack. The current observations on the shrouded inducer indicate that the flow on the blade surface is attached on the entire suction surface; the flow reversal at a certain location (along the blade chord) and its subsequent interaction with the upstream flow at blade tip causes the flow to leave the blade surface at the tip and move along the interior of the shroud. This is not a "classical" separation, but a an attached three-dimensional boundary layer phenomenon.

The cause for the flow reversal that occurs on the suction surface of the blade near the tip may be speculated upon. The reversal occurs in a region close to the rotating shroud and is influenced by the shroud boundary layer. Shear forces due to the rotating shroud boundary layer act in a direction opposite to that of the flow in the presence of an adverse pressure gradient. When these shear forces combined with the adverse pressure gradient become larger than the momentum of the fluid (from the shear pumping effect), the flow reverses direction. The flow on the shroud boundary layer within the blade passage area also reverses direction and finally moves upstream.

The internal flow in the shrouded inducer consists of radially outward flows except near the shroud. On the trailing edge the flows near the hub reverse and the blade passage area flow has tangential and axial vorticity components (similar to unshrouded inducers).

TABLE 3.1A. LIMITING STREAMLINE ANGLES, χ, ON THE SUCTION SURFACE OF THE 12° INDUCER AT $\phi = 0.083$.

Radial location	Leading edge	Mid-chord	Trailing edge
Hub	48^o	50^o	$\sim 70^o$
Mid-radius	40^o	35^o	$\sim 30^o$
Tip	45^o	29^o	29^o

TABLE 3.1B. LIMITING STREAMLINE ANGLES, χ, ON THE PRESSURE SURFACE OF THE 12° INDUCER AT $\phi = 0.083$.

Radial location	Leading edge	Mid-chord	Trailing edge
Hub	45^o	35^o	30^o
Mid-radius	35^o	20^o	25^o
Tip	30^o	25^o	25^o

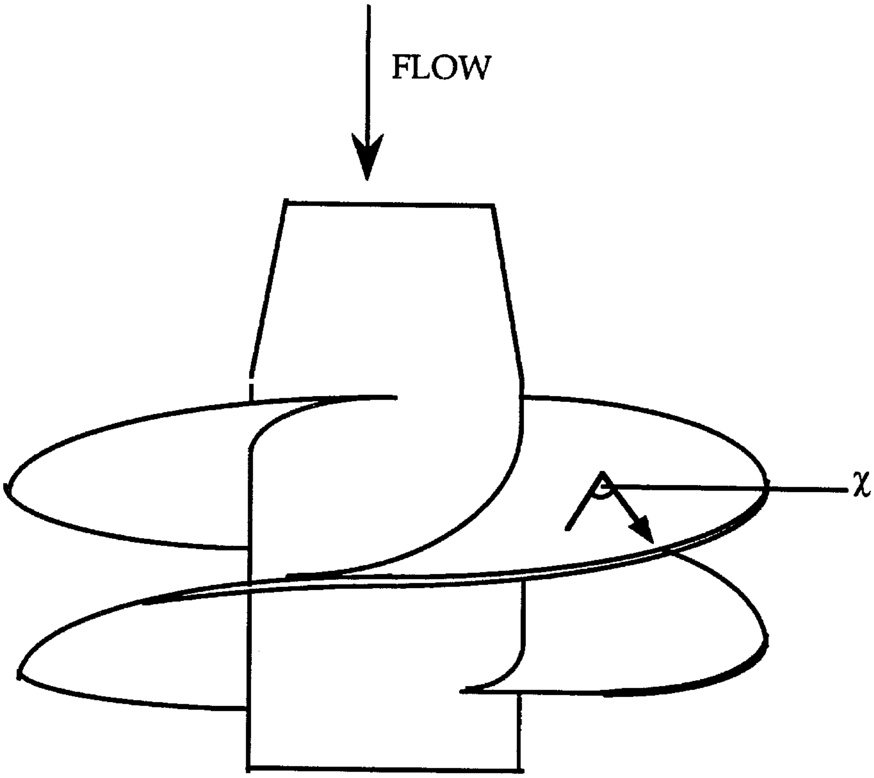

Figure 3.1 Typical inducer blade profile showing the limiting streamline angle (χ).

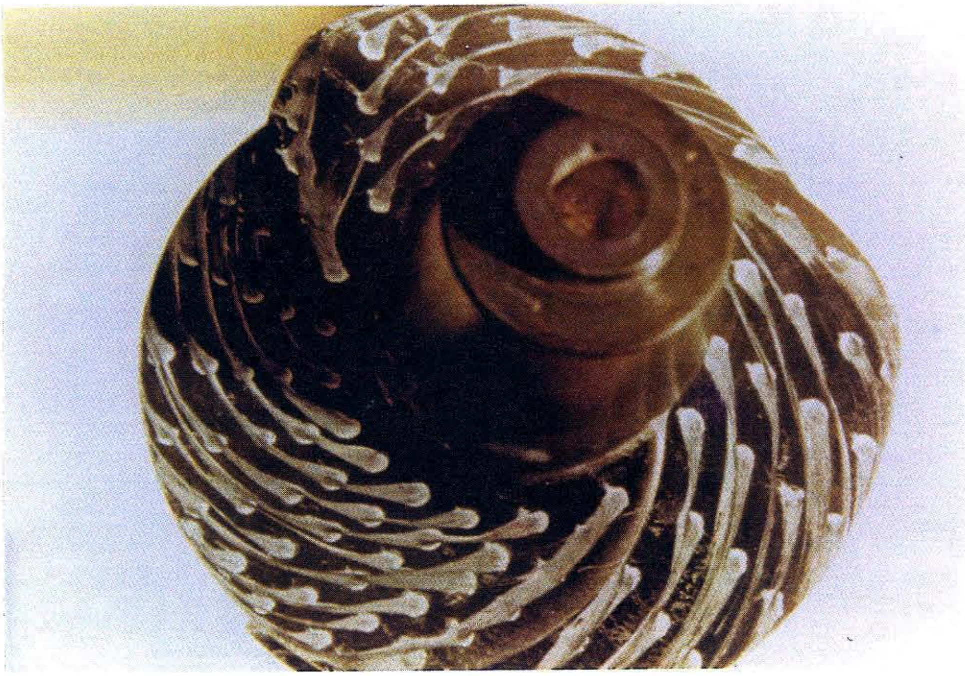

Figure 3.2. Photograph showing the paint traces on the suction side of inducer IX at $\phi = 0.041$.

Figure 3.3. Photograph showing the paint traces on the pressure side of inducer IX at $\phi = 0.041$.

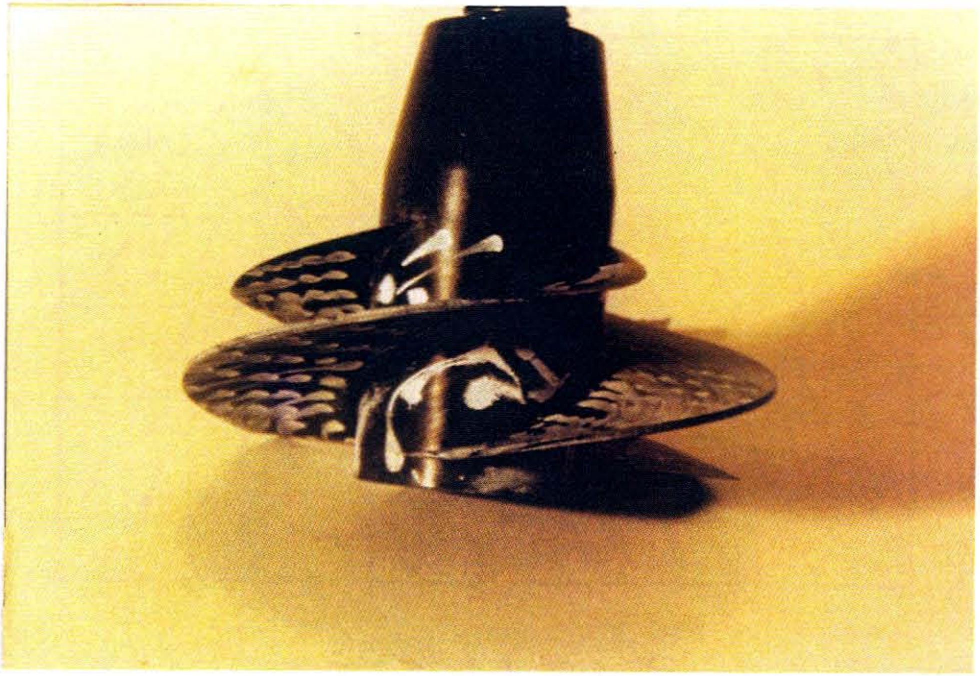

Figure 3.4. Photograph showing the paint traces due to downstream re-entry flow on the hub of inducer IX at $\phi = 0.041$.

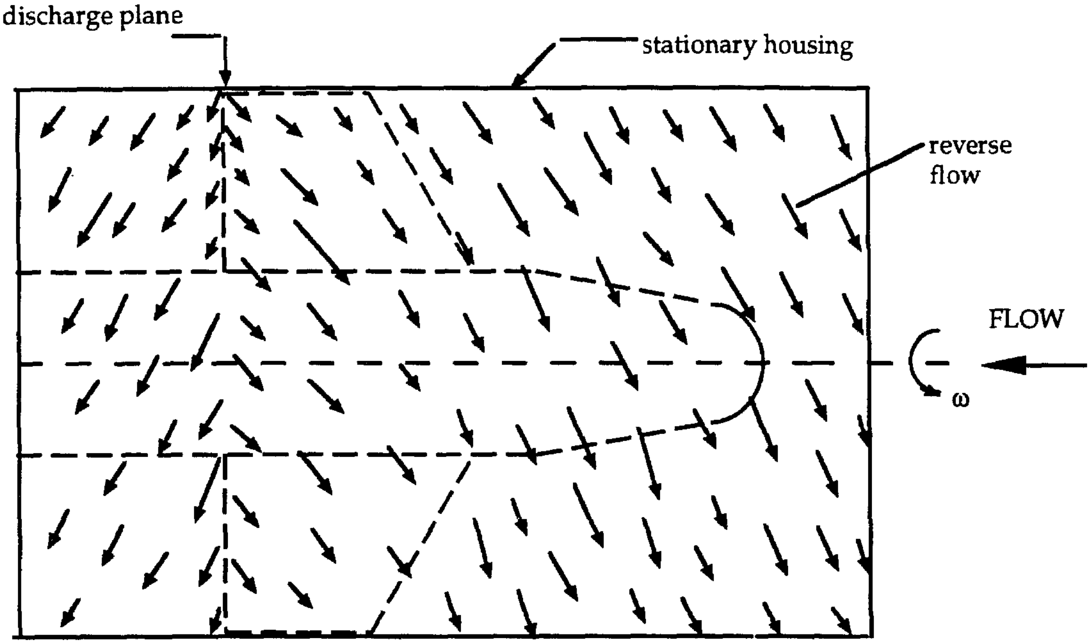

Figure 3.5. Sketch showing leakage flow, interior of the stationary housing of an unshrouded inducer.

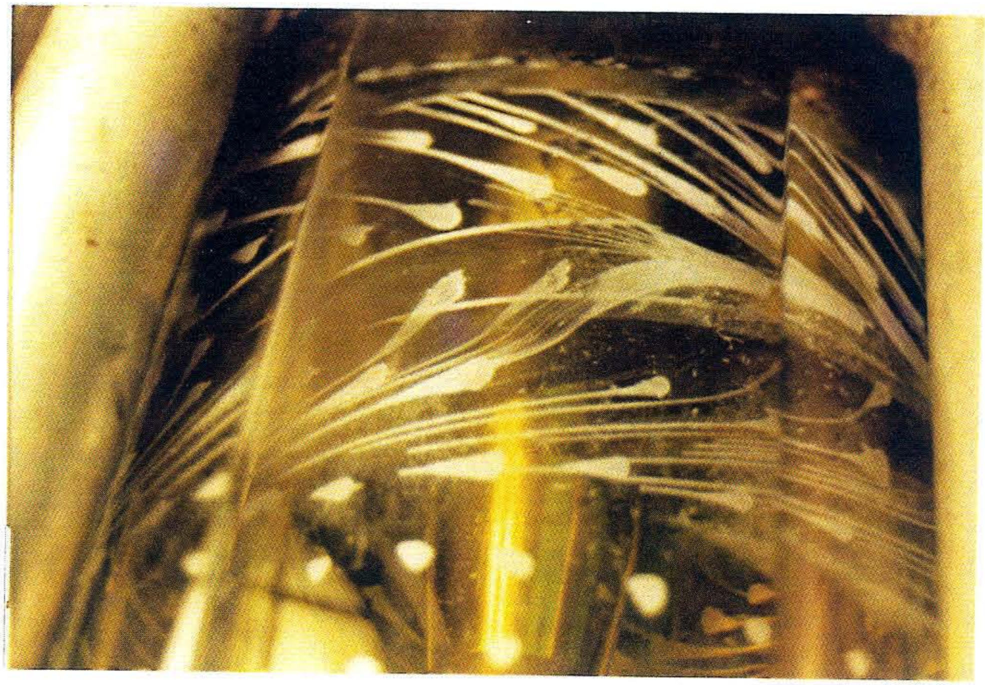

Figure 3.6. Photograph of the paint traces showing flow reversal on the housing of inducer VII at a flow coefficient $\phi = 0.07$ (i.e. with incipient upstream backflow). The inducer rotates from right to left and the flow direction is upwards.

Figure 3.7. Photograph showing the paint traces showing flow reversal on the suction side blade surface of the shrouded inducer at $\phi = 0.041$.

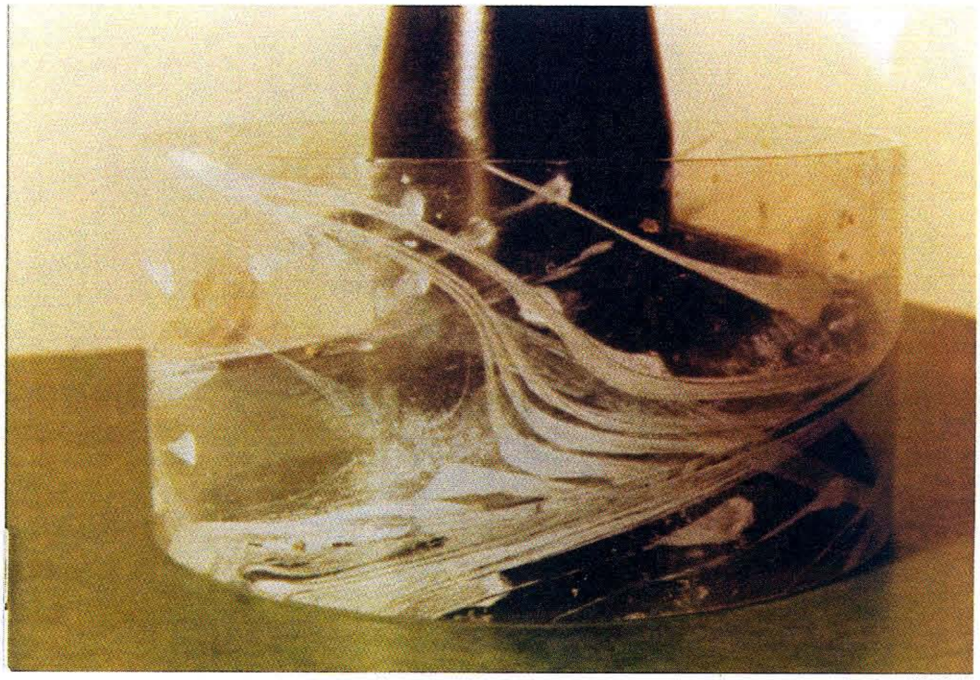

Figure 3.8a. Flow traces on the interior of the rotating shroud of the shrouded inducer at $\phi = 0.041$.

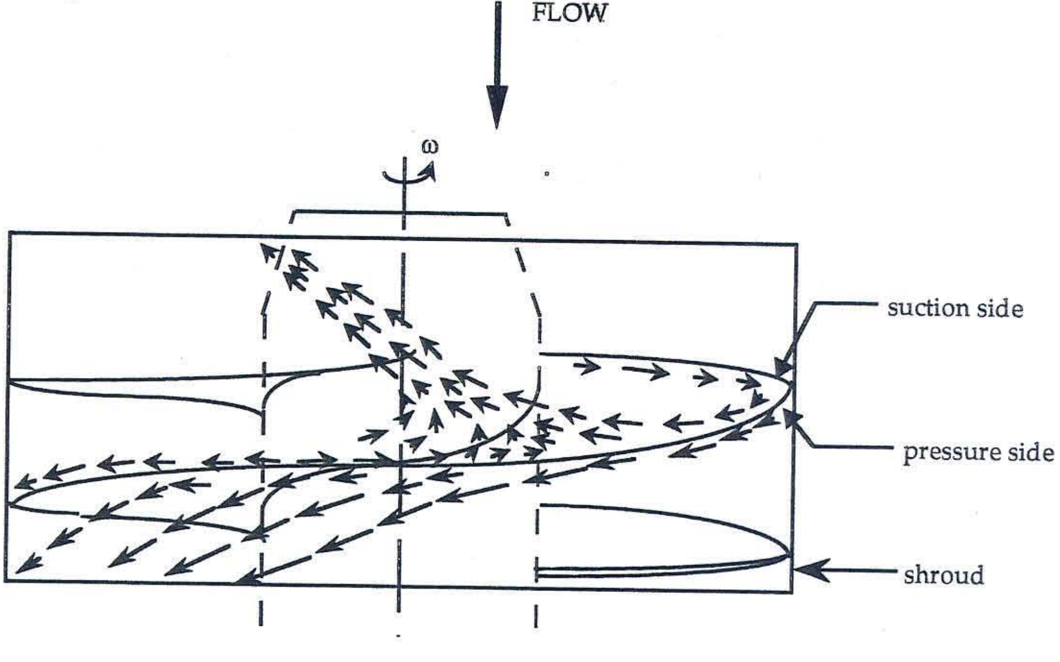

Figure 3.8b. Sketch showing the flow directions for figure 3.8a.

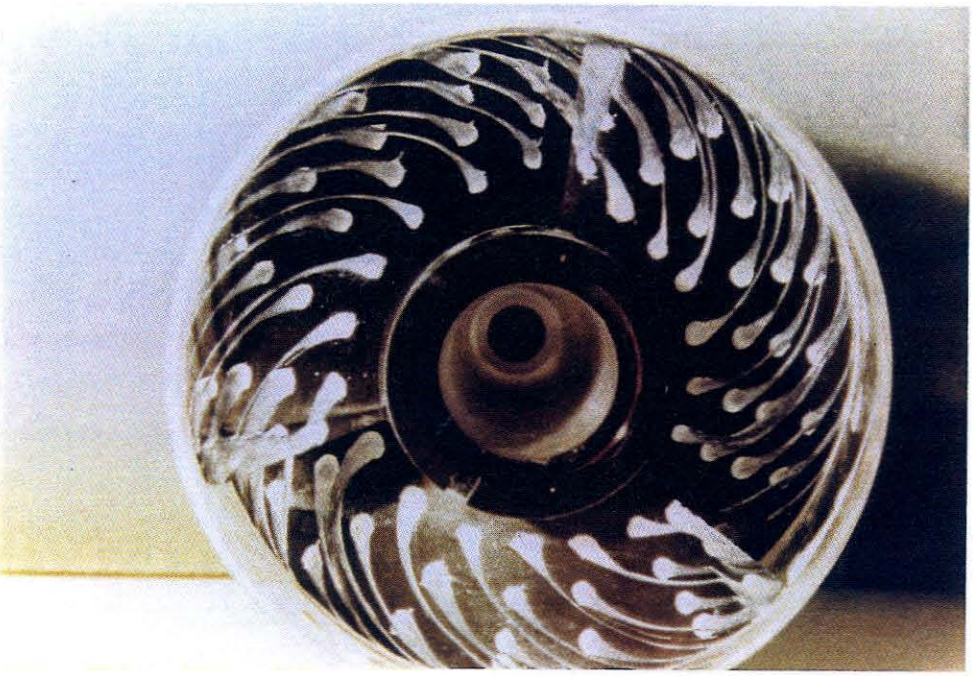

Figure 3.9. Flow on the pressure side of the shrouded inducer at $\phi = 0.041$.

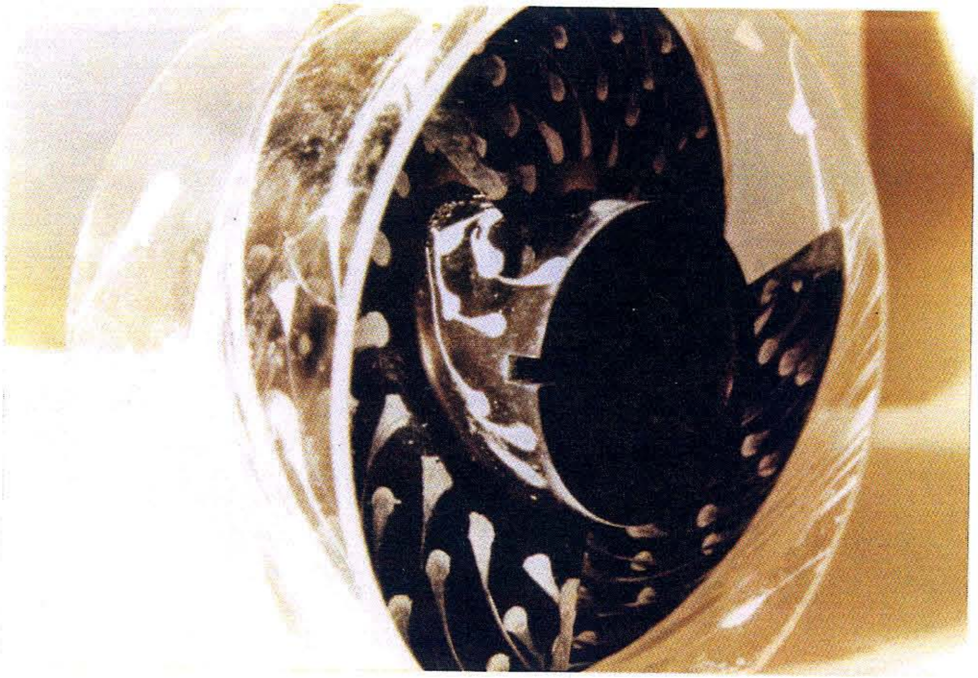

Figure 3.10. Downstream hub re-entry flow in the shrouded inducer at $\phi = 0.041$.

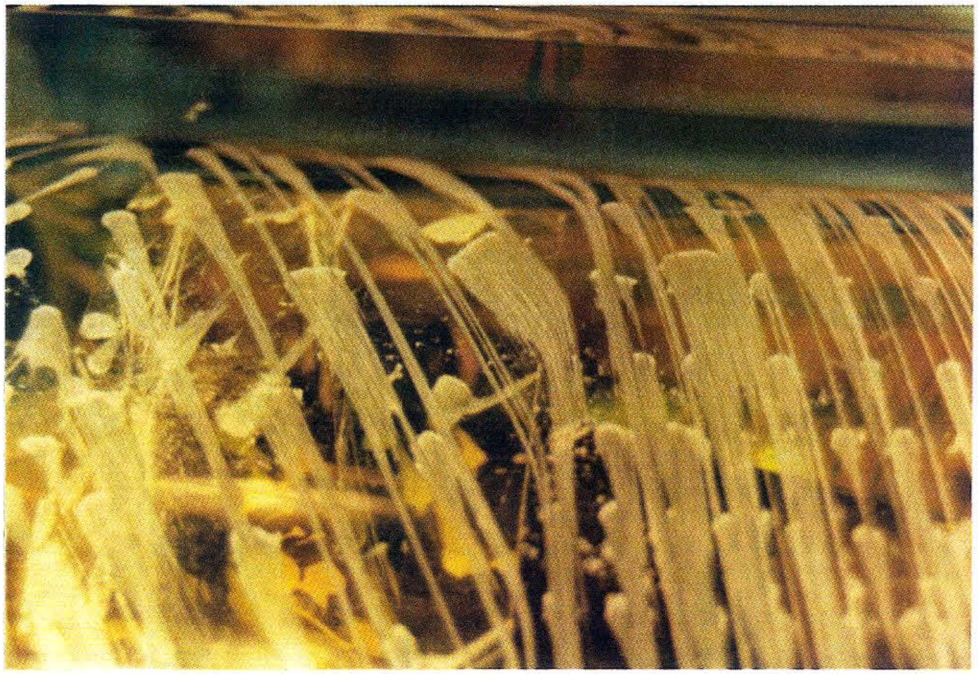

Figure 3.11. The leakage flow on the interior of the stationary housing of the shrouded inducer at $\phi = 0.041$.

CHAPTER 4

EXPERIMENTAL DATA FOR INDUCER ROTORDYNAMIC FORCES

The rotordynamic forces acting on inducer VII when it is whirled in a circular orbit have been investigated. As explained in chapter 1, the forces acting on the inducer consist of radial (or lateral) forces, and forces normal and tangential to the whirl orbit. It may be noted that some preliminary work in this chapter on inducer VII have also been presented earlier by Arndt and Franz (1986). This chapter provides a further detailed investigation of the forces on inducer VII and serves to confirm the previous findings. The results also provide reference data for further investigations on flow distortion and cavitation effects discussed in subsequent chapters.

4.1 ROTORDYNAMIC FORCE DATA

This section presents the results of the experiments conducted to measure the rotordynamic forces acting on inducer VII when it is whirled in a circular eccentric orbit at various whirl frequency ratios (i.e., whirl/shaft speed ratio, Ω/ω). The effects of varying the flow coefficients on these forces has also been investigated.

The experiments were conducted with the eccentricity (ε) of the circular whirl orbit set at 0.0254 cm (0.01 in.). Data were obtained at inducer rotational speeds of 2000 and 3000 rpm. The whirl frequency ratios were varied from -0.7 to +0.7 to cover a range of negative and positive whirl for the 2000 rpm tests.

The whirl frequency ratios varied from -0.55 to +0.55 for the 3000 rpm tests. The flow coefficients (ϕ) tested at 2000 rpm were 0.074, 0.059, 0.037, 0.015 and 0.0. The 3000 rpm tests were conducted at flow coefficients of 0.074 and 0.049.

The rotordynamic forces, F_n and F_t have been plotted as a function of the whirl frequency ratio (Ω/ω) in figures 4.1 and 4.2a respectively for the tests at 2000 rpm and the flow coefficients $\phi = 0.074$ and $\phi = 0.059$. It may be recalled from chapter 3 that the onset of upstream swirling backflow occurred at flow coefficients below $\phi \approx 0.070$ and that incipient downstream backflow was observed at $\phi < 0.060$. Thus the data in these figures represent the forces without backflow ($\phi = 0.074$) and with upstream backflow (and incipient re-entrant flow on the downstream hub at $\phi = 0.059$). It is observed from figure 4.1 that the characteristics of F_n with whirl frequency ratio change with a decrease in the flow coefficient (and the occurrence of reverse flows). F_n remains positive (destabilizing) at the lower flow coefficient ($\phi = 0.059$) for the range of negative whirl frequency ratios tested and shows a positive peak at $\Omega/\omega \approx +0.1$. The tangential force also shows a non-monotonic behavior with the whirl frequency ratio. For both the flow coefficients ($\phi = 0.074$ and $\phi = 0.059$), the tangential force shows multiple zero crossings and the occurrence of positive (destabilizing) peaks at positive whirl frequency ratios. A negative peak of F_t is seen at $\Omega/\omega \approx +0.1$ for $\phi = 0.059$, but the force remains destabilizing for $\Omega/\omega \geq +0.2$. F_t remains stabilizing for the entire range of negative whirl frequency ratios. In order to verify the repeatability of the data, experiments at all flow coefficients were repeated. One such repeat run data for the tangential force at $\phi = 0.059$ is shown in figure 4.2b, which confirms the non-monotonic variation of the tangential force with whirl frequency ratio.

Figures 4.3 and 4.4 show the rotordynamic forces on inducer VII for the same conditions of figures 4.1 and 4.2a but with lower flow coefficients, $\phi = 0.037$, 0.015 and 0.0. Thus the forces represented in this figure occur when the upstream backflow and the downstream re-entrant flow have strongly developed. It is interesting to note that at these flow coefficients, the normal forces are approximately the same at all whirl frequency ratios. The normal force shows a non-quadratic behavior with the whirl frequency ratio, especially at positive Ω/ω. F_n is mostly negative (hence stabilizing) for positive whirl, and becomes increasingly negative close to synchronous speeds. The tangential forces do not vary significantly with flow coefficient for negative whirl frequency ratios. For positive whirl, however, it is important to note that the magnitude of the destabilizing peak of F_t tends to be higher for lower flow coefficients. F_t also shows multiple zero crossings similar to that in figure 4.2a.

Figures 4.5 and 4.6 show the rotordynamic forces at a higher rotational speed and with flow coefficients without backflow ($\phi = 0.074$) and with upstream and downstream backflow ($\phi = 0.049$). At 3000 rpm the normal force remains negative over the entire range of positive whirl frequency ratios tested, but shows a destabilizing peak at $\Omega/\omega \approx +0.1$ for the lower flow coefficient $\phi = 0.049$. The tangential force is larger in magnitude (and stabilizing) for the lower flow coefficient over the entire range of negative whirl frequency ratios tested. For positive whirl, however, a large destabilizing peak is observed at $\Omega/\omega \approx +0.1$ for $\phi = 0.049$. An interesting feature of this plot is that while F_t shows a non-monotonic behavior, it remains positive (destabilizing) for the entire range of Ω/ω and shows no zero crossings.

Figures 4.7a and 4.7b show a comparison of the normal and tangential forces on inducer VII at 2000 rpm and 3000 rpm for a flow coefficient $\phi = 0.074$. It may be noted that the order of magnitude of the non-dimensionalized forces do not change with rotational speed. The peak in the tangential force at $\Omega/\omega \approx +0.4$ for 2000 rpm decreases in magnitude at the higher rotational speed. The variations in the magnitudes of the forces are possibly because of non-linearities such as those occurring due to viscous effects.

The results of these experiments as presented in figures 4.1 - 4.7 bring out several significant characteristics of the rotordynamic forces in axial flow inducers of the type used in these experiments and are summarized below. The data for the tangential force as reported previously in impeller force measurements by Jery et al. (1985) and Miskovish and Brennen (1992) show a linear behavior with whirl/shaft speed ratios. In the region of negative whirl frequency ratios, the tangential force on the inducer are stabilizing for all flow coefficients. Data for the inducer, however, shows a non-monotonic behavior, marked by multiple zero crossings of the force for positive whirl particularly after the onset of flow reversal. Thus the tangential force on the inducer has several regions of instability at off-design flows. In general, the multiple zero crossings increase with decreasing flow rates. Moreover, the tangential force data also shows one or more peaks in its magnitude in the region of positive whirl/shaft speed ratios. The magnitude of the largest peak is seen to be dependent on the flow coefficient. The magnitude of the destabilizing peak also tends to increase to its highest value as the flow coefficient is lowered ($\phi = 0.015$ at 2000 rpm). At a flow coefficient ϕ --> 0.0, this magnitude decreases. The magnitude of the largest peak is significant (compared to previous rotordynamic pump data) and could cause instabilities in the whirl. It may also be noted that the tangential forces tend to become destabilizing close to synchronous speeds (at low flow coefficients).

The normal force data also shows multiple zero crossings when plotted against the whirl frequency ratios. These zero crossings are in the region of positive Ω/ω. In the case of centrifugal pump impellers, the normal force usually shows a quadratic variation, as shown by Jery et al. (1985) and Miskovish and Brennen (1992). Rotordynamic shroud forces due to leakage flows in centrifugal pumps also show a quadratic behavior (Guinzburg 1992). The data obtained for inducers, however, does not show a similar behavior.

It may be recalled from chapter 1 that rotordynamic forces are typically characterized by stiffness, damping and inertia matrices. Implicit in this characterization is a quadratic behavior of the forces with whirl frequency ratio. However, as the data for inducers presented in this chapter indicates, the forces have to be approximated by higher order polynomials. Thus the representation of the components of the rotordynamic matrix $[A]$ does not hold for the inducer. Consequently, the generalized stiffness, damping and inertia matrices for the inducer cannot be determined. Rotordynamic analysis of the inducer must, therefore, include fluid-induced forces which are more general functions of the whirl frequency ratio.

4.2 STEADY (LATERAL) FORCE DATA

The lateral forces acting on inducer VII at various flow coefficients are presented in figures 4.8a and 4.9a and the corresponding angles are shown in figures 4.8b and 4.9b. The results show that the forces do not vary significantly with the whirl frequency ratio. Data is also obtained for the lateral force and force angles at zero whirl frequency when the inducer is located at different positions on the whirl orbit. The results are presented in figures 4.10a and 4.10b. In general, the magnitudes of these forces are found to be low and there are no significant effects of flow coefficient on these forces (the experiments were conducted with uniform upstream and downstream conditions, the importance of which is detailed in chapter 5).

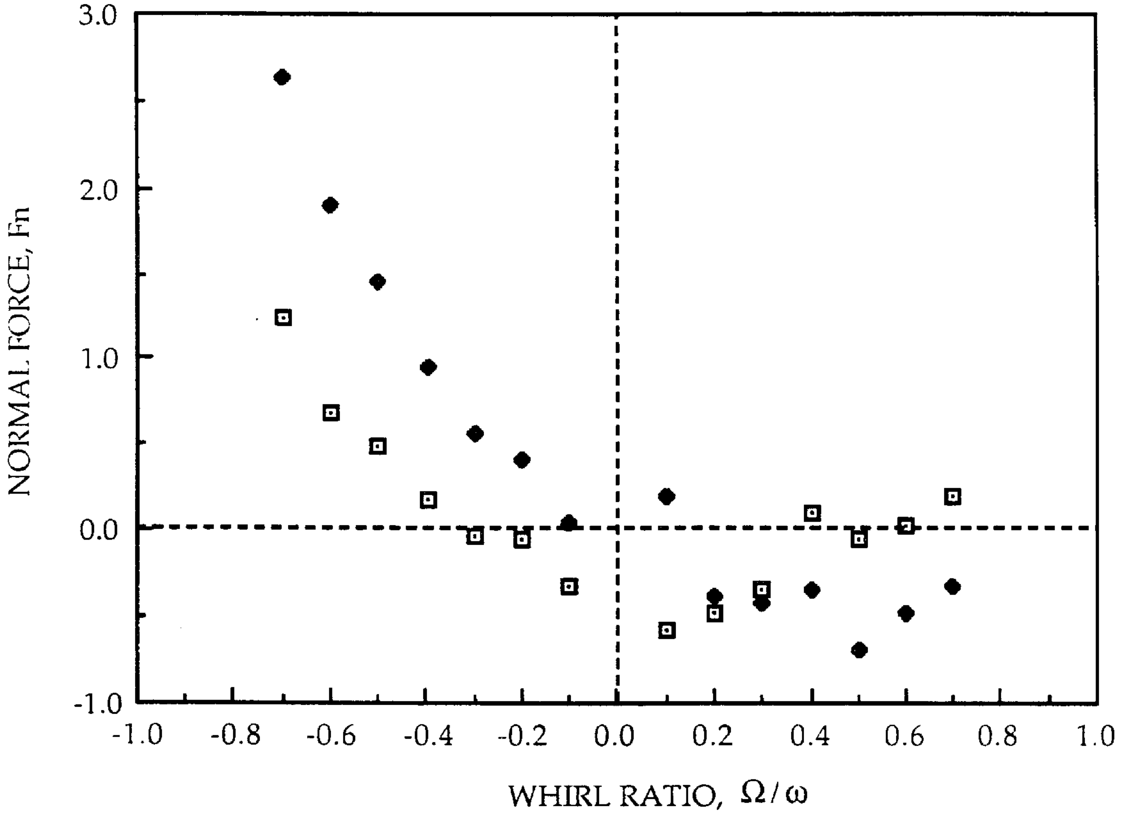

Figure 4.1. Non-dimensionalized normal force on inducer VII at various whirl frequency ratios (2000 rpm; ▣ - ϕ = 0.074; ◆ - ϕ = 0.059).

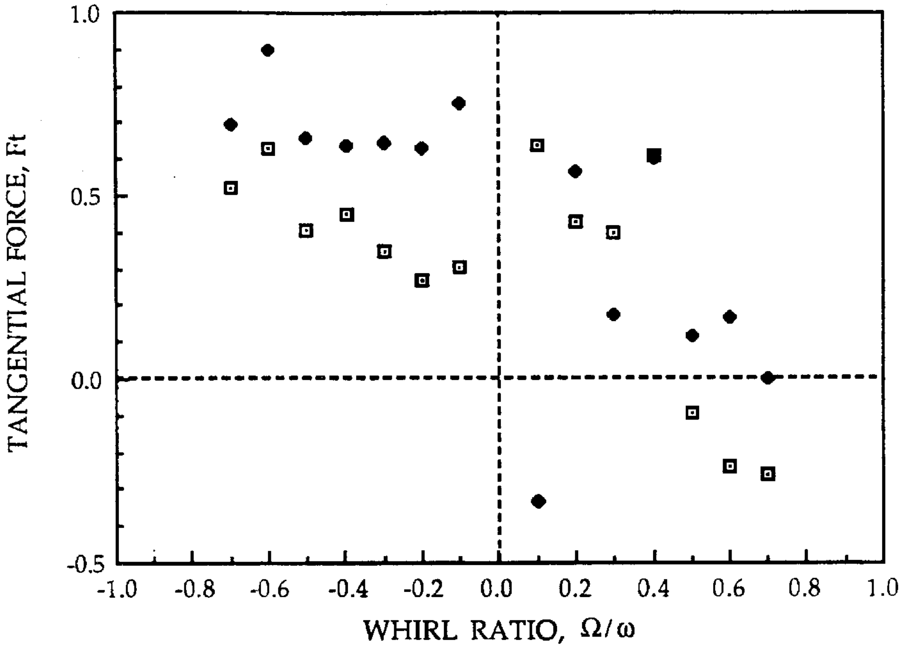

Figure 4.2a. Non-dimensionalized tangential force on inducer VII at various whirl frequency ratios (2000 rpm; ▣ - $\phi = 0.074$; ◆ - $\phi = 0.059$).

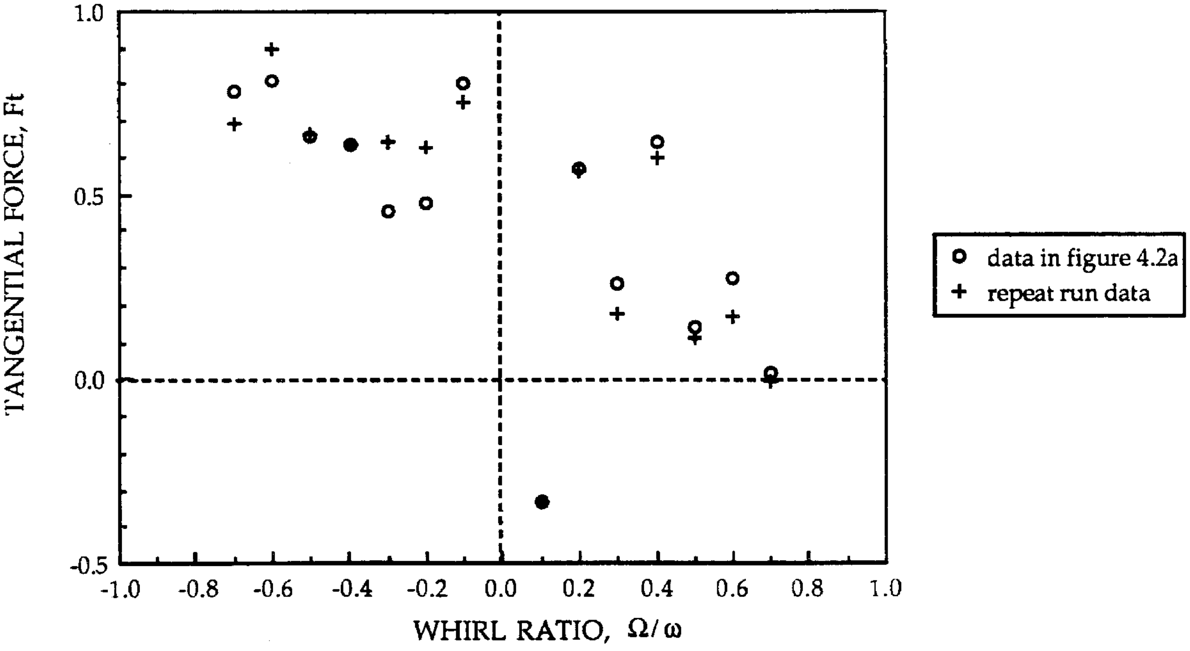

Figure 4.2b. Non-dimensionalized tangential force data for inducer VII for a typical repeat run at $\phi = 0.059$; 2000 rpm.

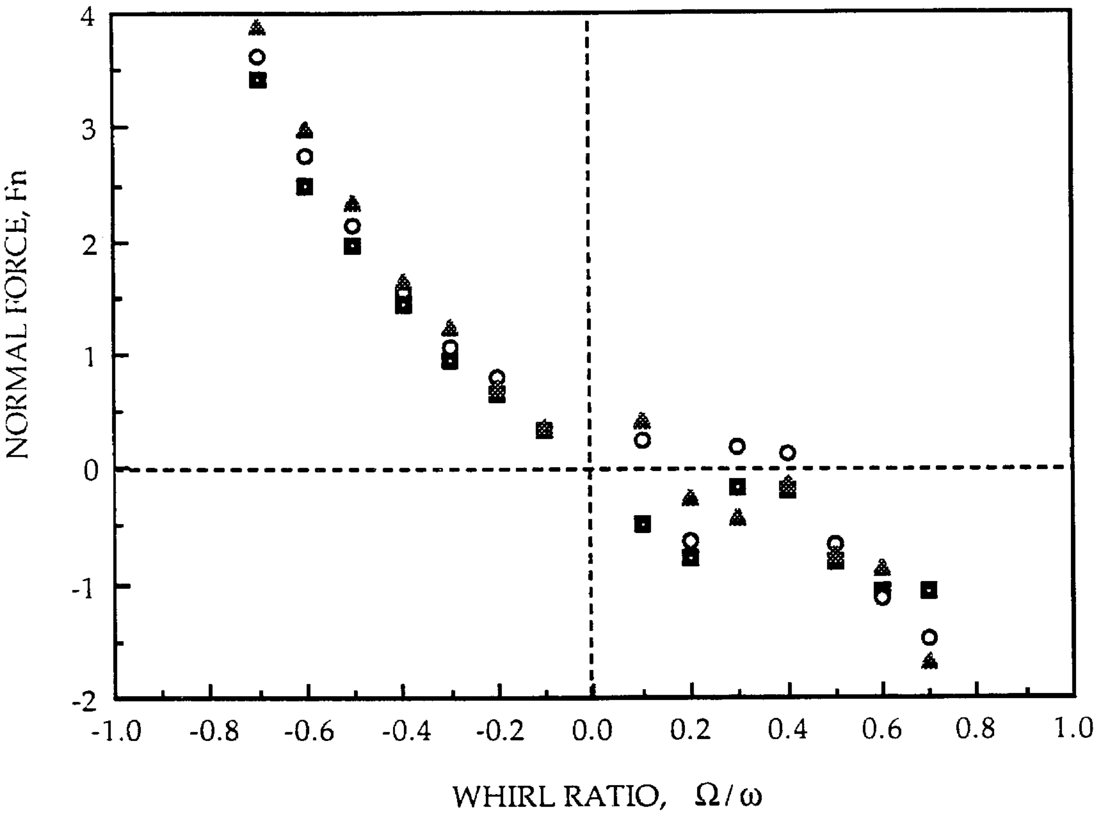

Figure 4.3. Non-dimensionalized normal force on inducer VII at 2000 rpm (■ - ϕ = 0.037; ○ - ϕ = 0.015; ▲ - ϕ = 0.0).

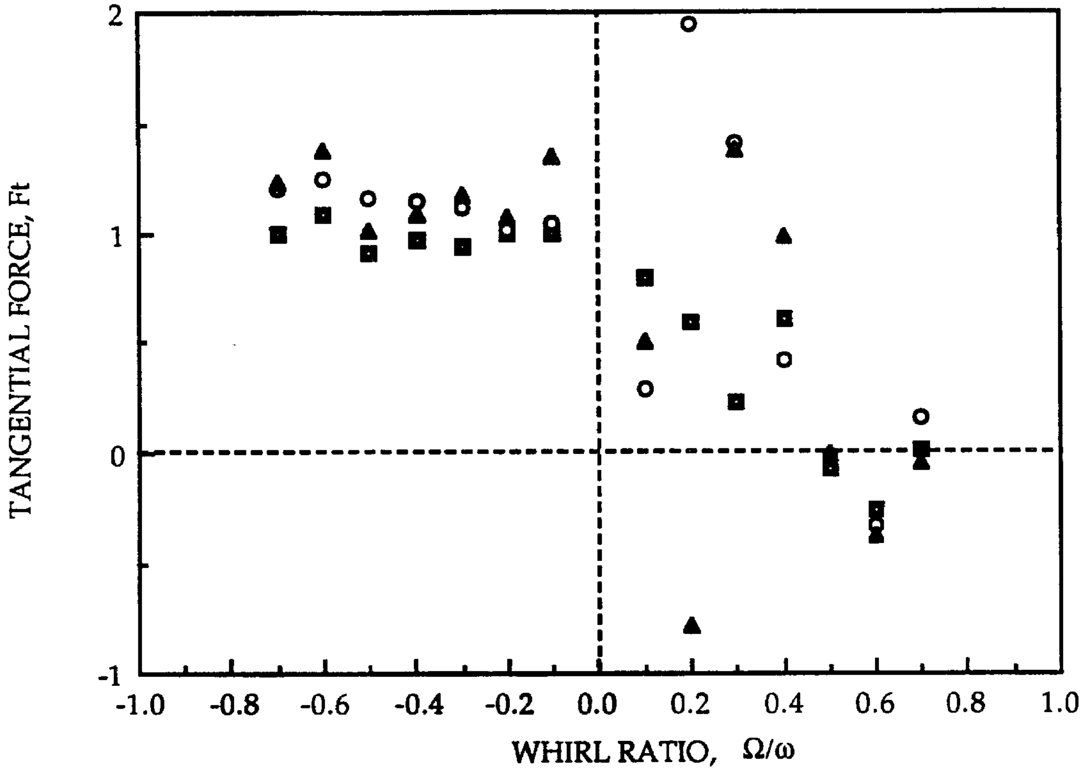

Figure 4.4. Non-dimensionalized tangential force on inducer VII at 2000 rpm (■ - ϕ = 0.037; ○ - ϕ = 0.015; ▲ - ϕ = 0.0).

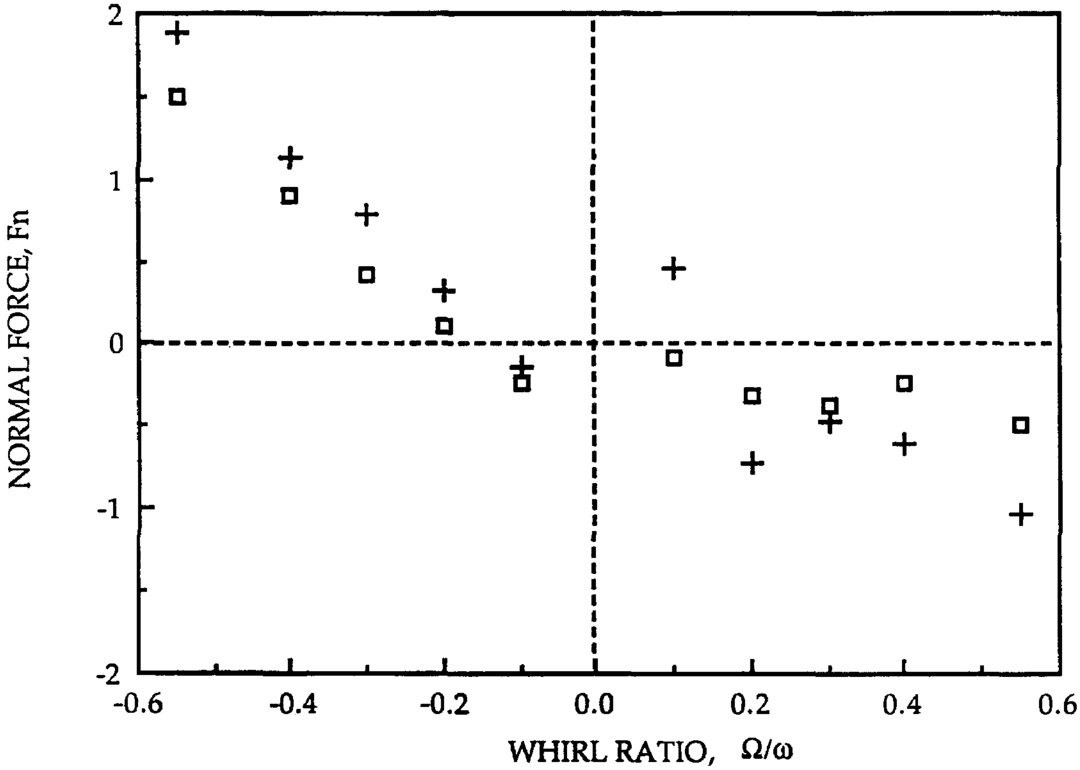

Figure 4.5. Non-dimensionalized normal force on inducer VII at 3000 rpm
(□ - ϕ = 0.074; + - ϕ = 0.049).

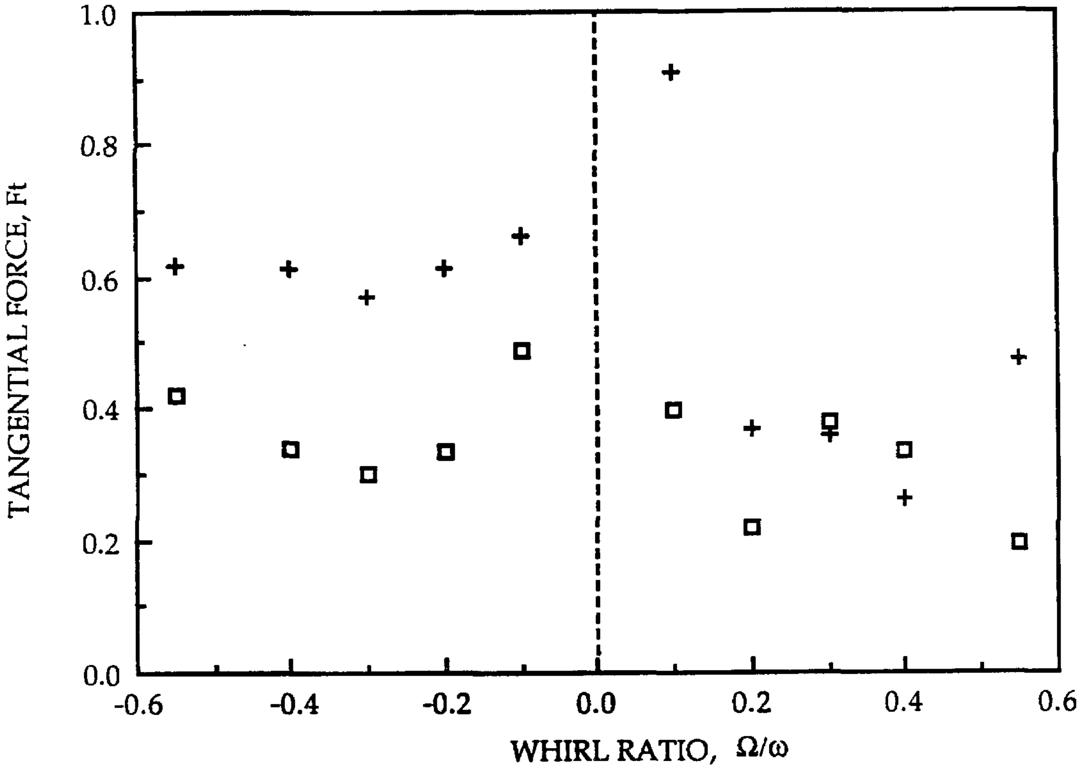

Figure 4.6. Non-dimensionalized tangential force on inducer VII at 3000 rpm (□ - ϕ = 0.074; + - ϕ = 0.049).

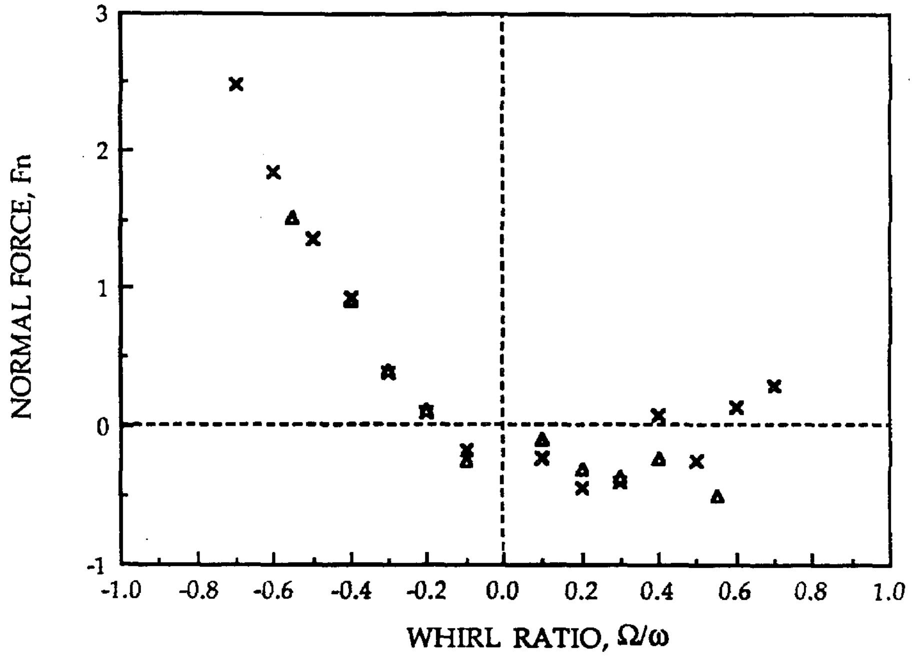

Figure 4.7a. Comparison of non-dimensionalized normal force on inducer VII at ϕ = 0.074 for different rotational speeds (× - 2000 rpm; ▲ - 3000 rpm).

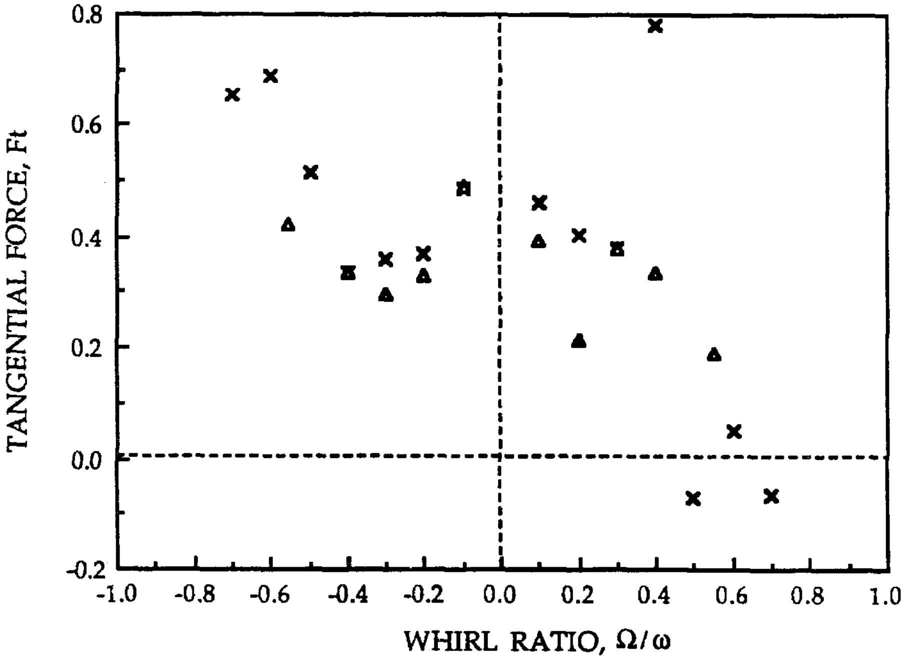

Figure 4.7b. Comparison of non-dimensionalized tangential force on inducer VII at ϕ = 0.074 for different rotational speeds (× - 2000 rpm; ▲ - 3000 rpm).

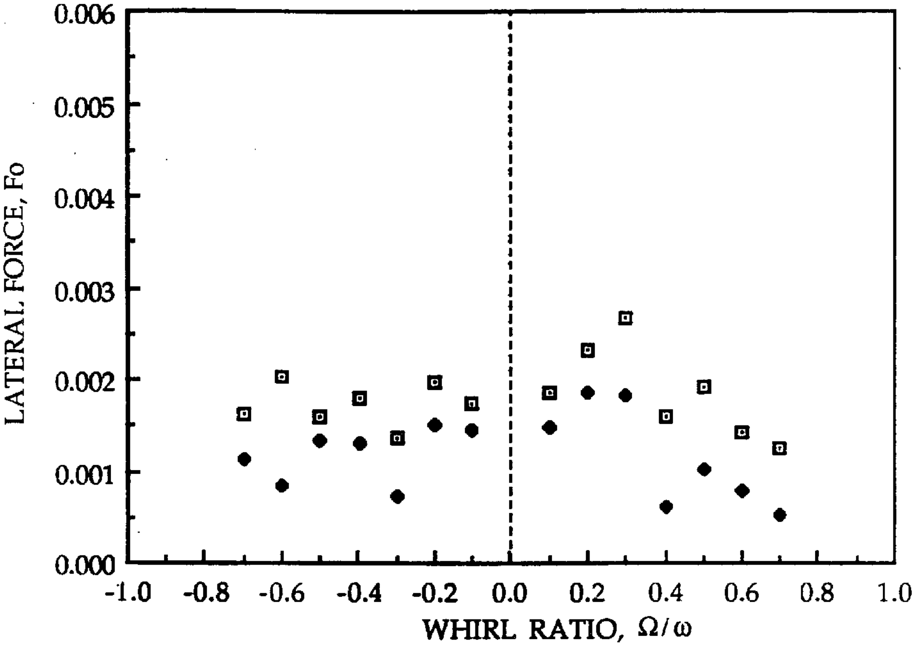

Figure 4.8a. Non-dimensionalized lateral force on inducer VII at 2000 rpm (▣ - ϕ = 0.074; ◆ - ϕ = 0.059).

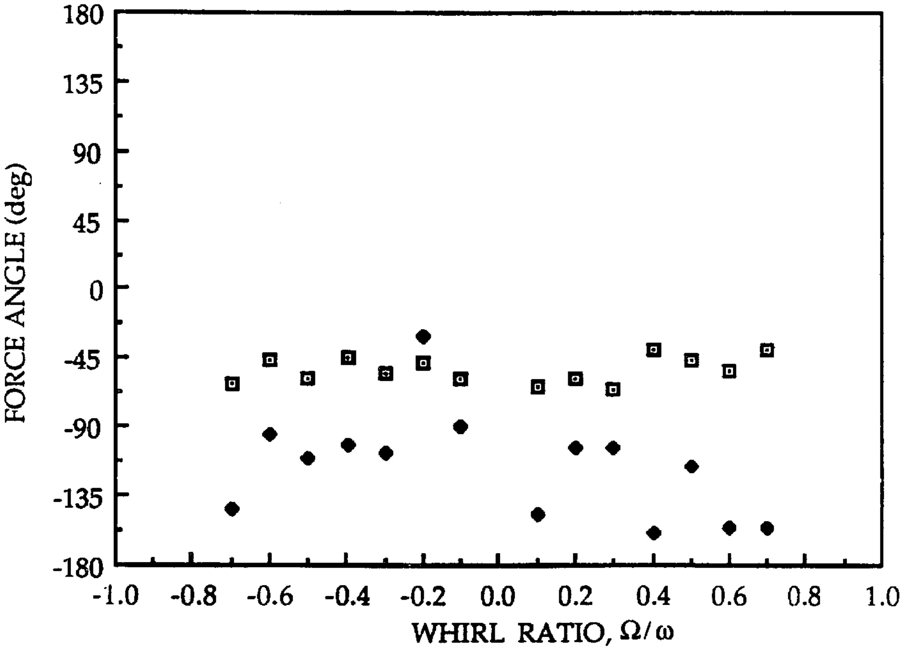

Figure 4.8b. Angle of the lateral force shown in figure 4.8a (▣ - ϕ = 0.074; ◆ - ϕ = 0.059).

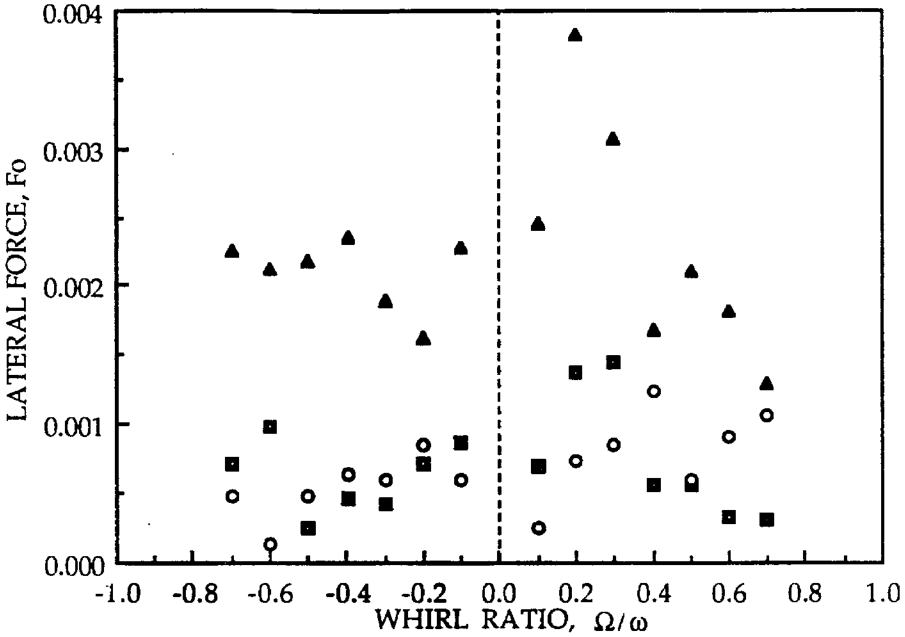

Figure 4.9a. Non-dimensionalized lateral force on inducer VII at 2000 rpm
(■ - $\phi = 0.037$; ○ - $\phi = 0.015$; ▲ - $\phi = 0.0$).

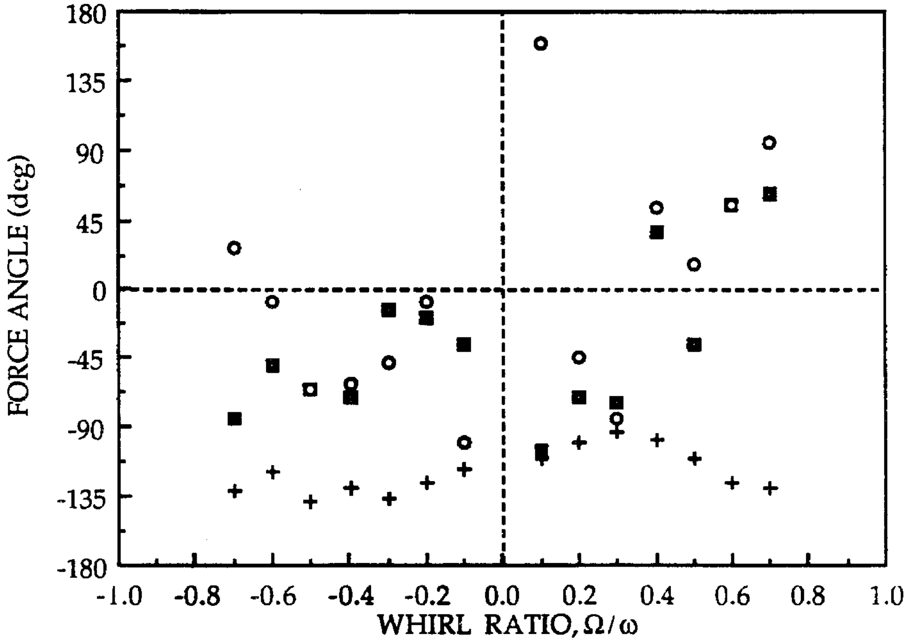

Figure 4.9b. Angle of the lateral force shown in figure 4.9a
(■ - $\phi = 0.037$; ○ - $\phi = 0.015$; + - $\phi = 0.0$).

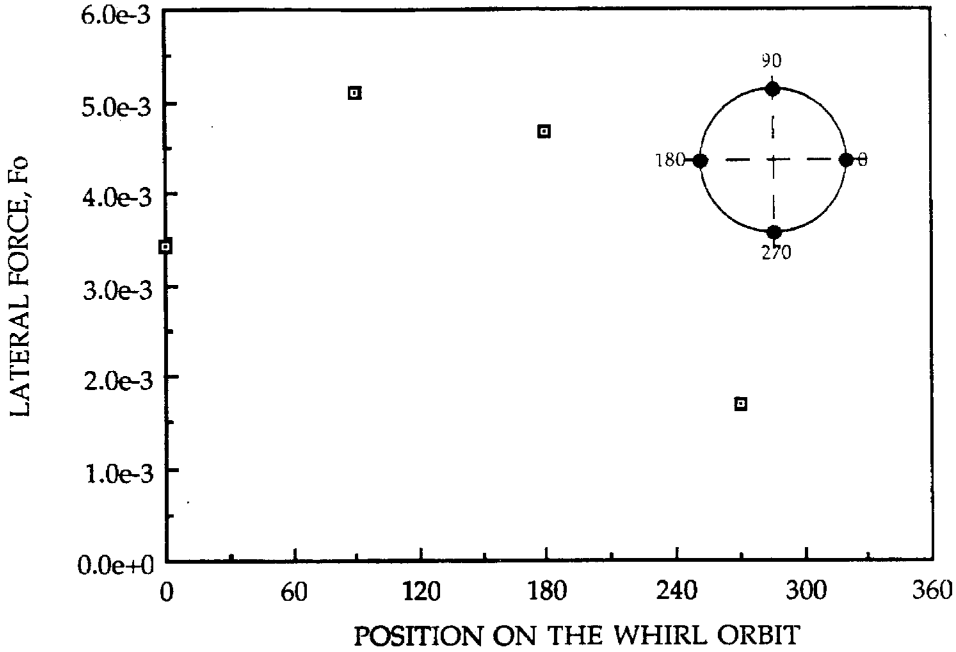

Figure 4.10a. Non-dimensionalized lateral force on inducer VII at 2000 rpm and $\phi = 0.074$ at various locations on the whirl orbit (zero whirl frequency).

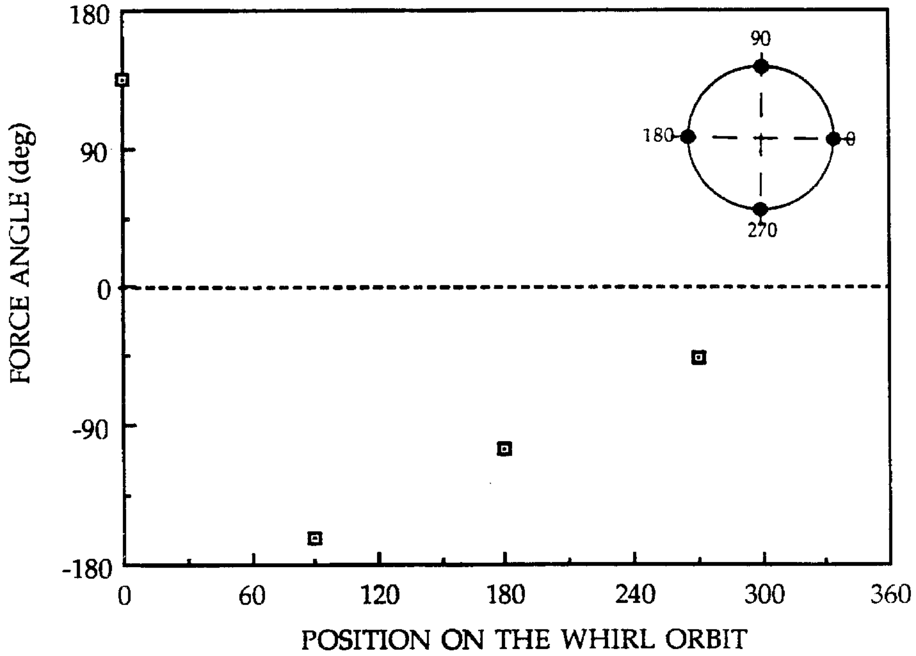

Figure 4.10b. Angle of the lateral force shown in figure 4.10a.

CHAPTER 5

FLOW DISTORTION EFFECTS

The effects of flow asymmetries on the lateral forces acting on the inducer have also been investigated. Experimental force data was obtained to study the effects of downstream and upstream flow distortions. The data also revealed the effect of off-design flows on the lateral force in the presence of downstream asymmetries in the system. It was also observed that the rotordynamic normal and tangential forces were not significantly affected by the upstream and downstream flow distortions. The data presented in this chapter are for non-cavitating conditions of the inducer. The inducer rotational speed was fixed at 2000 rpm for these tests.

5.1 EFFECT OF A DOWNSTREAM SYSTEM ASYMMETRY

The inducer installation in the RFTF was such that the flow from the discharge plane of the inducer entered a larger asymmetric housing. A cross-section of this downstream asymmetry, which is inherent to the system is shown in figure 2.3. The steady force, F_0, acting on the inducer was measured for several flow coefficients. The experiments were conducted with the eccentricity (ε) set to zero (no whirl). There were no upstream asymmetries in the system.

The results (figure 5.1a) show that the lateral force increases to large values at low flow coefficients ($\phi < 0.08$). The forces increase with a decrease in flow coefficient. The peak magnitude of the lateral force occurs at $\phi \approx 0.05$ for inducer IX and at $\phi \approx 0.04$ for inducer VII. The magnitude of the normalized force observed at low flow coefficients is significantly large, compared to the normalized force in centrifugal pumps reported by Jery (1986) and Franz (1989).

However, for flow coefficients close to design, the magnitude of these forces are observed to be very low. The angles at which these forces act are measured from the horizontal (X) axis of the reference frame (see figure 1.1). The angles are measured positive in an anti-clockwise sense. These angles are shown in figure 5.1b.

The results of the flow visualization experiments reported in chapter 3 show the range of flow coefficients (below design) at which flow reversals occur. It can, therefore, be inferred that the lateral force on the inducer increases when reverse flows occur. In particular, the reverse flows originating downstream have a significant effect on the lateral force (in the case of a downstream asymmetry). The reverse flow consists of high energy fluid (on which pumping work has been done). The asymmetric downstream condition creates an asymmetric reverse flow in the inducer, thereby causing a large lateral force.

5.1.1 EFFECT OF A UNIFORM DOWNSTREAM SCREEN

5.1.1a LATERAL FORCES

In order to create a uniform circumferential exit condition a cylindrical screen (with a 30% opening, see detail in chapter 2) was placed at the exit (see figure 2.1). The screen serves to reduce the tangential component of flow and provides a uniform circumferential resistance to the radial flow. The performance characteristics of inducer VII due to the downstream screen is presented in figure 5.2. The lateral force on the inducer after the imposition of this screen is plotted against flow coefficient for inducer IX in figure 5.3a and the angle at which the force acts is shown in figure 5.3b. The figure also shows a comparison of the forces with and without the downstream screen. The results show that the magnitude of the normal force (with downstream screen) is near zero at all flow coefficients tested. The results thus confirm that a negligible lateral force acts on an inducer placed symmetrically in the housing and with no upstream and downstream flow asymmetries.

5.1.1b ROTORDYNAMIC FORCES

The effect of the downstream screen on the rotordynamic forces have also been investigated. The inducer was placed in a circular whirl orbit and rotordynamic force data was obtained at various whirl frequency ratios. The normal and tangential forces obtained are plotted against the whirl frequency ratio in figures 5.4a and 5.4b respectively. The results show that the downstream asymmetry does not have any significant influence on the rotordynamic forces.

5.2 EFFECT OF UPSTREAM FLOW ASYMMETRIES

5.2.1 INLET SHEAR DUE TO HONEYCOMB SECTIONS

Preliminary work on the study of inlet modification effects were conducted using honeycomb sections placed upstream. Previous studies were conducted using similar screens to investigate the effects of such screens on inducer performance (Del Valle et al. 1990). These honeycomb sections were therefore used in the preliminary experiments as a starting point towards the understanding of the effects of an inlet shear on inducer forces. The velocity profile created by the honeycomb sections are shown in figure 5.5. The installation of these honeycombs has been described in section 2.4.1. The velocity profiles at the inlet without any flow distortion is shown in figure 5.6 for comparison. It may be noted that the velocity profiles were measured approximately $1^1/_2$ inducer diameters upstream. The measurements were taken along different radial locations in a vertical plane at the center of the pipe. The pipe diameter at this section was 11.68 cm. (compared to the inducer blade tip diameter of 10.12 cm.). The experiments were conducted with the eccentricity set to zero. The initial experiments were conducted at a flow coefficient ϕ = 0.041. The results are presented in figure 5.7. It may be noted that at the time these initial set of experiments were conducted, the effects of downstream asymmetry inherent to the system were as yet unknown. Consequently, the results also include forces due to the downstream asymmetry which are significant at this flow coefficient. Furthermore, the results show an increase in the magnitude of these forces with rotational speed which is not expected since the forces are non-dimensionalized with tip speed. The variations of the force with speed are probably due to the higher pressures of the downstream backflow at higher rotational speeds and due to Reynolds number effects on the tip clearance flow. These results are inconclusive regarding the effects of an inlet shear on the forces. Further experiments were conducted with stronger inlet shear flows and uniform downstream boundary conditions. These experiments are described in section 5.2.2 below.

5.2.2 INLET SHEAR DUE TO SCREENS

The effect of an inlet shear flow on the lateral and rotordynamic forces acting on inducer VII are presented in this section. For these experiments, the downstream screen was also used so that there were no effects of downstream asymmetry. The inlet shear flows were created using two screens, SC1 and SC2, the details of which are presented in chapter 2 and appendix A. In brief, screen SC1 was designed to create an approximately linear axial velocity profile with the velocity at one end of the pipe being 7.3 times that at the other end. Screen

SC2 was also designed to create a linear velocity profile, but to a lesser degree; the velocity at one end of the pipe was 3 times that at the other end. The screens were placed approximately four inducer diameters upstream in a manner described in chapter 2. The actual velocity profiles generated by these screens are shown in figure 5.8.

The axial velocity profiles shown in figure 5.8 are approximately linear. The velocity profile due to screen SC1 shows maximum velocity to be 6.5 times that of the minimum velocity along the linear profile. In the case of screen SC2, this maximum velocity on the linear part of the profile is 3 times that of the minimum velocity. Thus the profiles are in fact quite close to design. However, the boundary layer at the top of the pipe (near the maximum velocity of the profile) is quite large, especially in the case of screen SC2.

The lateral and steady forces on inducer VII due to each of these screens were measured at a flow coefficient $\phi = 0.074$ (i.e., without any upstream swirling backflow). The eccentricity (ε) was set at 0.0254 cm. and the inducer was whirled at several whirl frequencies. The steady (lateral) forces on the inducer due to screens SC1 and SC2 are shown in figure 5.9a and compared with the forces without distortions. Figure 5.9b shows the angle at which the force acts. The results show that the screen SC2 does not have any significant effect on the steady forces. However, screen SC1 does cause a significant increase in the steady force (≈3 times). These steady forces remain approximately constant with whirl frequency ratio. The rotordynamic normal and tangential forces on the inducer due to the screens have been plotted in figures 5.10a and 5.10b. The data shows that these inlet distortions do not have any significant effect on the rotordynamic forces.

5.2.3 EFFECT OF AN UPSTREAM BEND

In practical applications, an upstream bend often exists in the inlet ducting. The effect of a 180^{o} bend, placed approximately four inducer diameters upstream, on the lateral force on inducer VII has been investigated. The installation of the bend in the system is described in chapter 2. The eccentricity was set to zero (no whirl). Figure 5.11 shows the axial and the swirl velocity profiles caused by the bend. The velocity measurements were taken at the same location as before (see section 5.2.1).

The lateral forces acting on the inducer due to the bend are shown in figure 5.12a and compared with the forces without any distortions. The angle at which the forces act are shown in figure 5.12b. The results show that there are no significant forces on the inducer due to the bend. Compared to the axial velocity profile created by the screen SC1, the profile due to the bend does not represent a significant distortion (in terms of magnitude and rate of change with radius); thus a lower lateral force results. From these tests, it may be concluded that a 180^{o} bend placed 4 inducer diameters upstream does not cause a significant lateral force on an inducer.

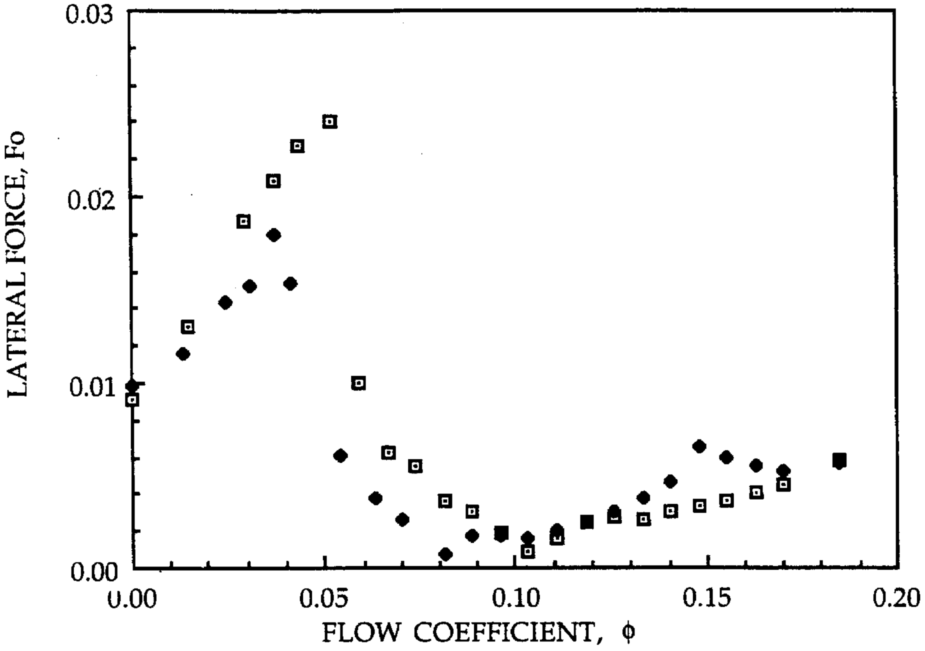

Figure 5.1a. The non-dimensionalized lateral force as a function of flow coefficient in the presence of the downstream asymmetry (◆ - inducer VII; ◘ - inducer IX).

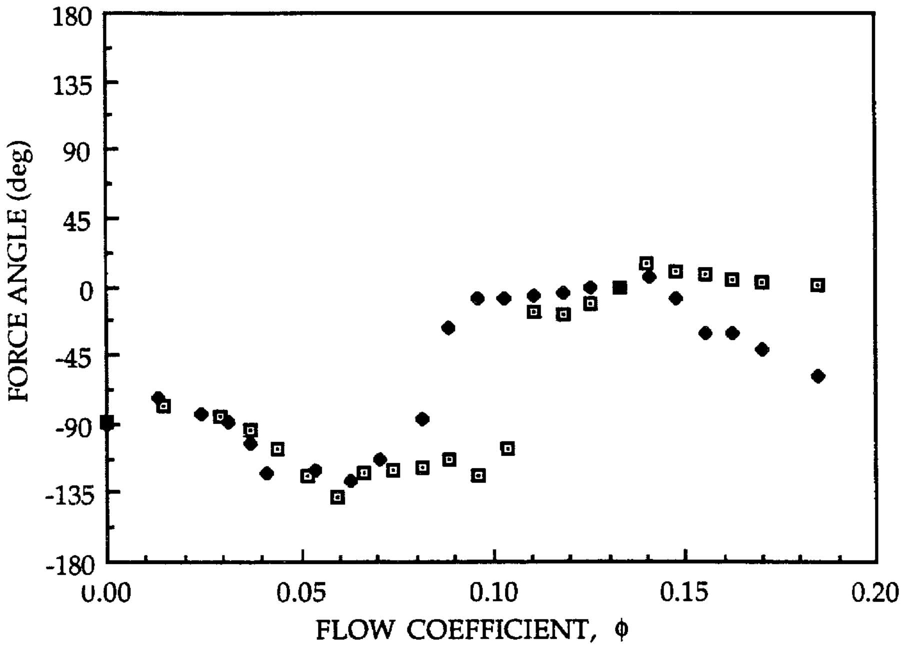

Figure 5.1b.Angle of the lateral force shown in figure 5.1a.
(◆ - inducer VII; ◘ - inducer IX).

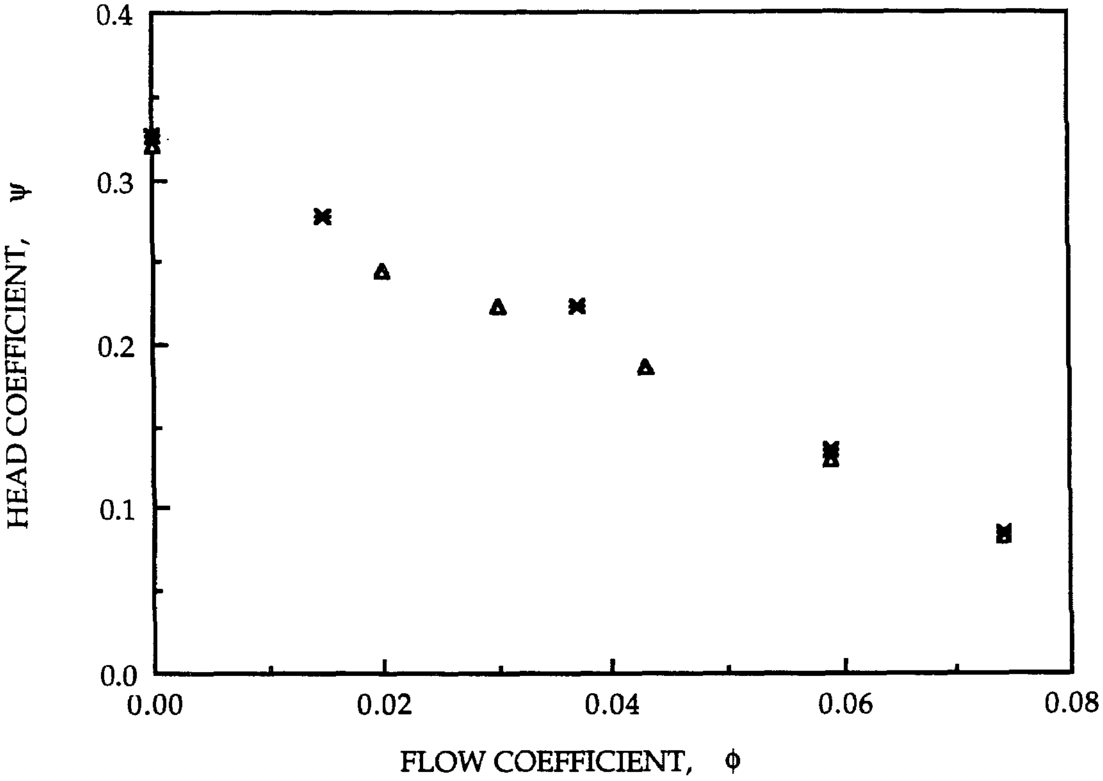

Figure 5.2. Performance characteristics of inducer VII at 2000 rpm (▲ -without screen; ✖ - with downstream screen).

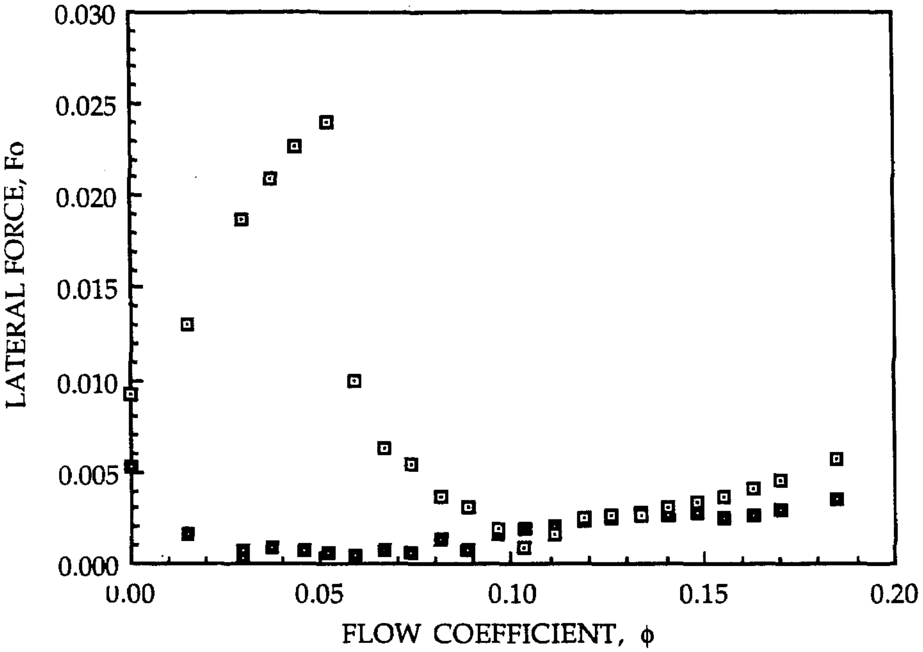

Fig. 5.3a. Effect of the downstream screen on the non-dimensionalized lateral force on inducer IX (▣ – with downstream asymmetry; ■ - with downstream screen).

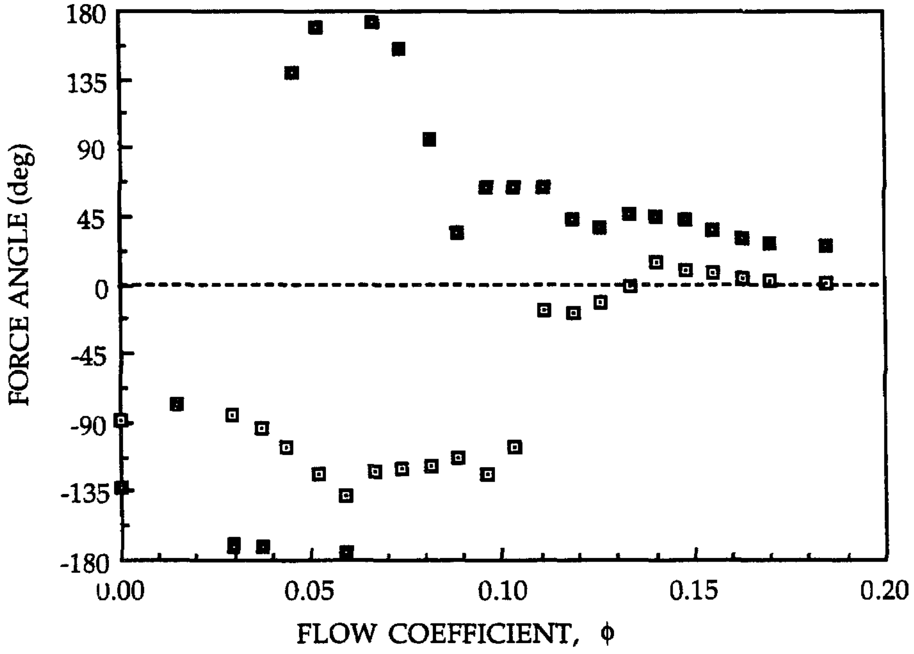

Figure 5.3b. Angle of the lateral force shown in figure 5.3a (▣ - with downstream asymmetry; ■ - with downstream screen).

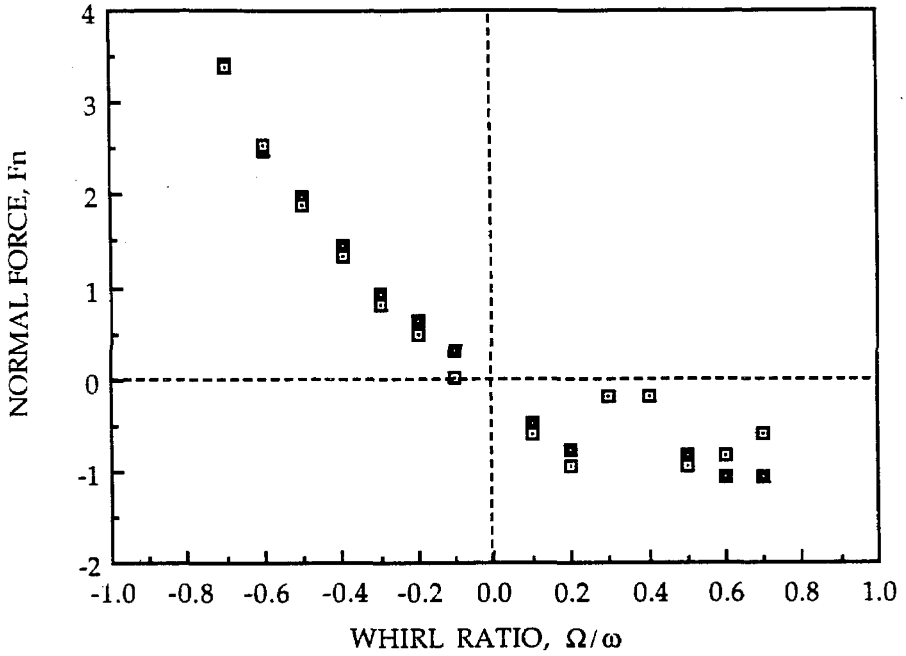

Figure 5.4a. Effect of the downstream screen on the non-dimensionalized normal force on inducer VII at a flow coefficient ϕ = 0.037
(▣ - with downstream asymmetry; ■ - with downstream screen).

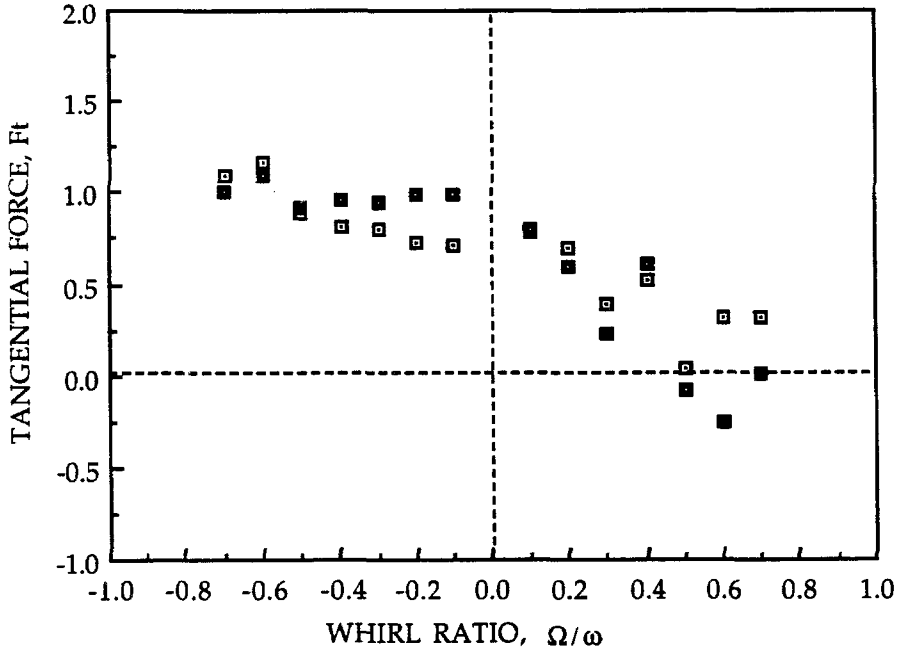

Figure 5.4b. Effect of the downstream screen on the non-dimensionalized tangential force on inducer VII at a flow coefficient ϕ = 0.037
(▣ - with downstream asymmetry; ■ - with downstream screen).

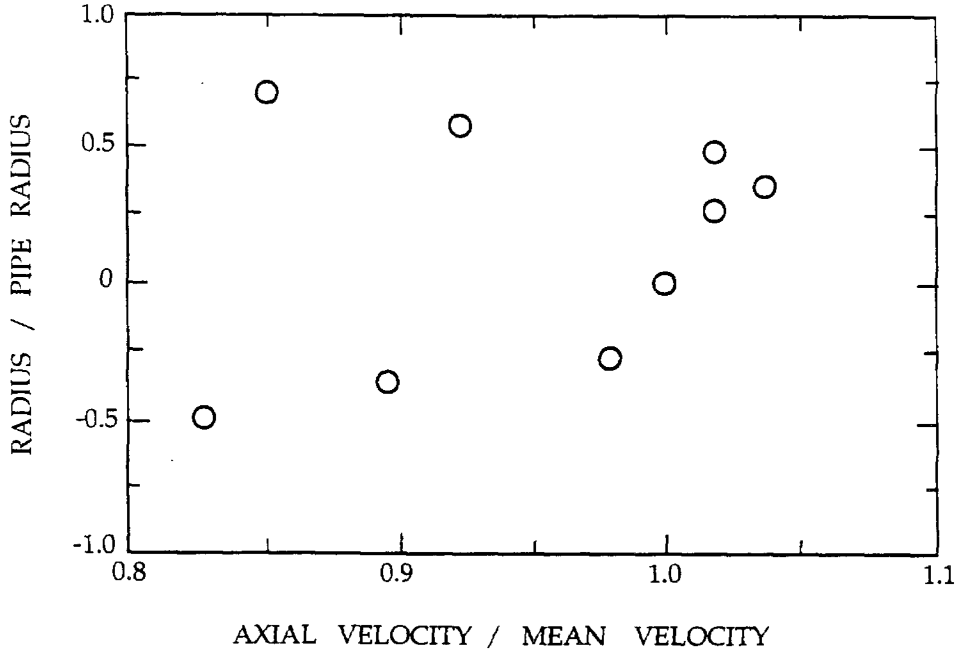

Figure 5.5. Axial velocity profile created by the honeycomb sections.

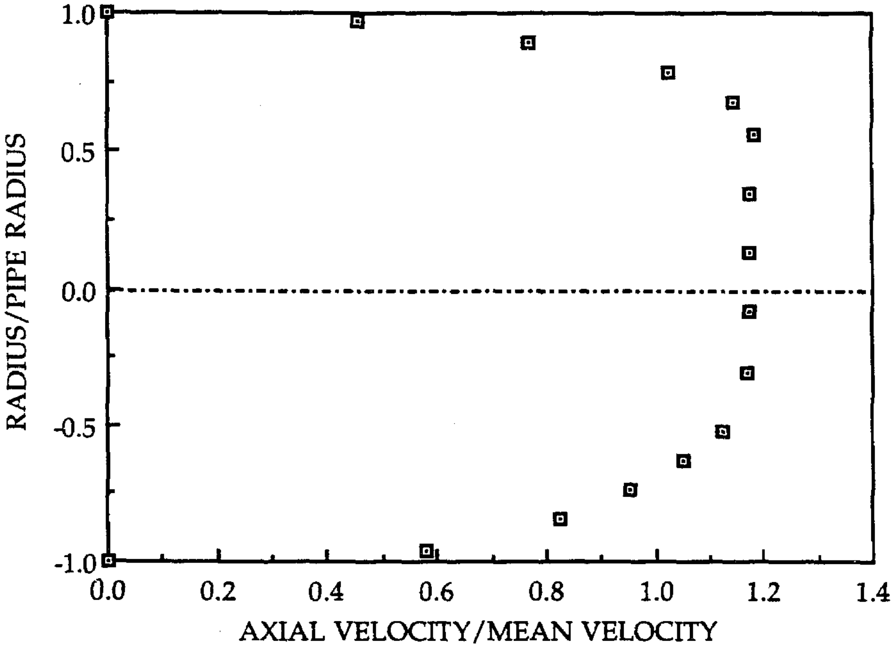

Figure 5.6. Axial velocity profile (upstream) without inlet distortions.

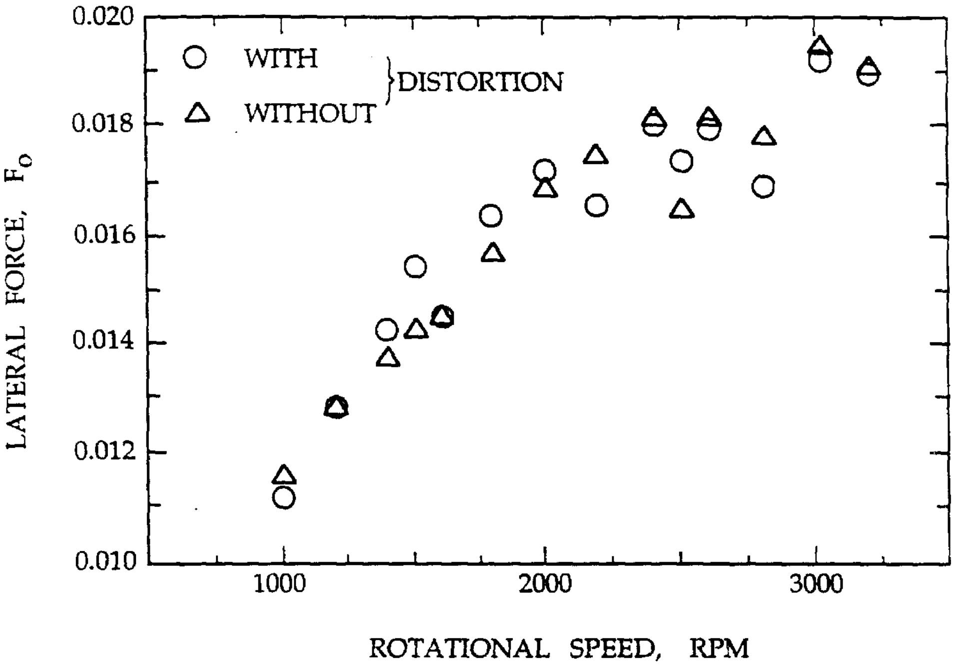

Figure 5.7. Non-dimensionalized lateral force on inducer VII at various rotational speeds and ϕ = 0.041.

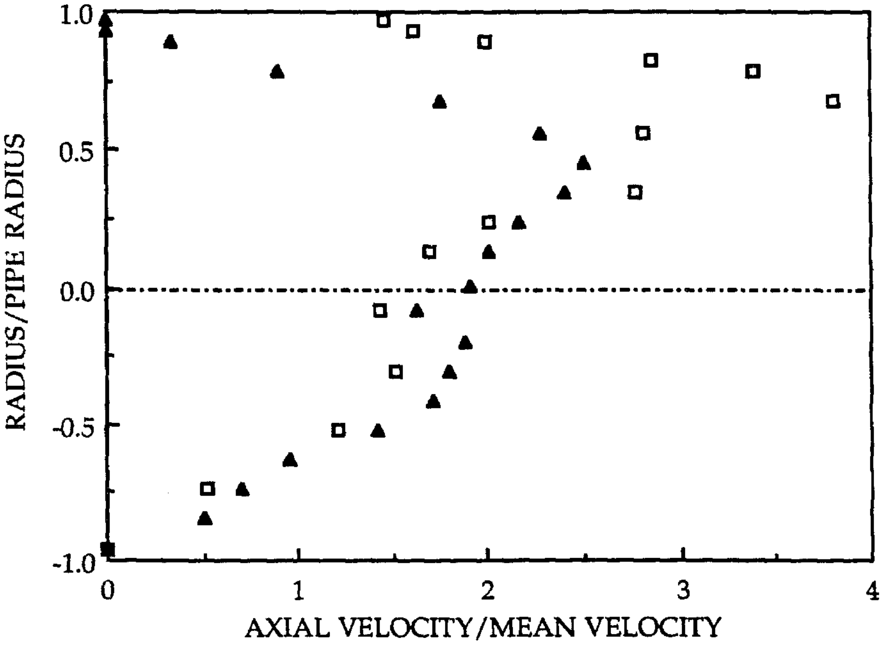

Figure 5.8. Axial velocity profiles due to screens SC1 and SC2 (◻ - SC1; ▲ - SC2).

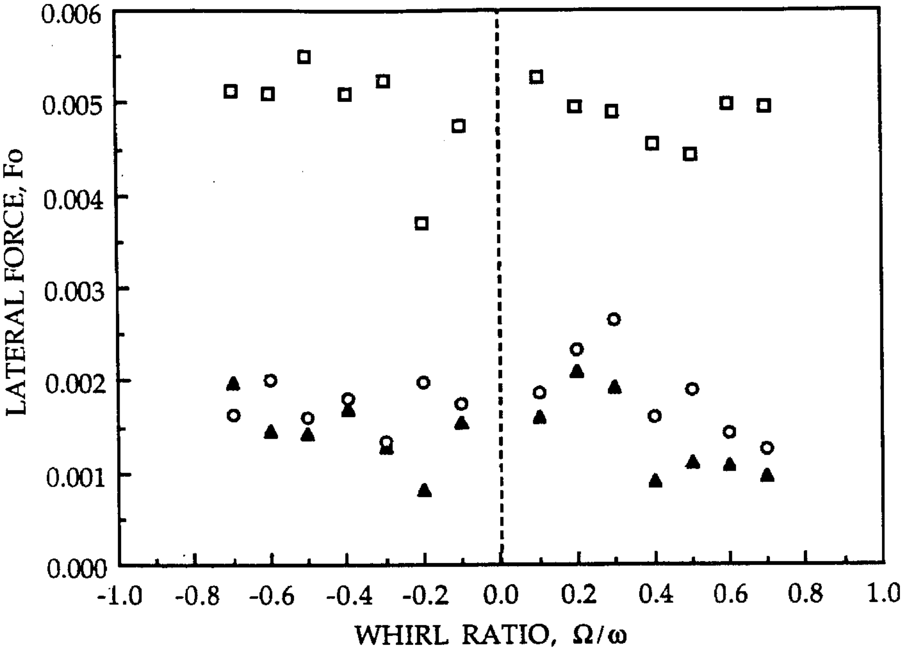

Figure 5.9a. The effect of inlet distortion screens SC1 and SC2 on the non-dimensionalized lateral force on inducer VII
(ϕ = 0.074; □ - SC1; ▲ - SC2; ○ - no distortion).

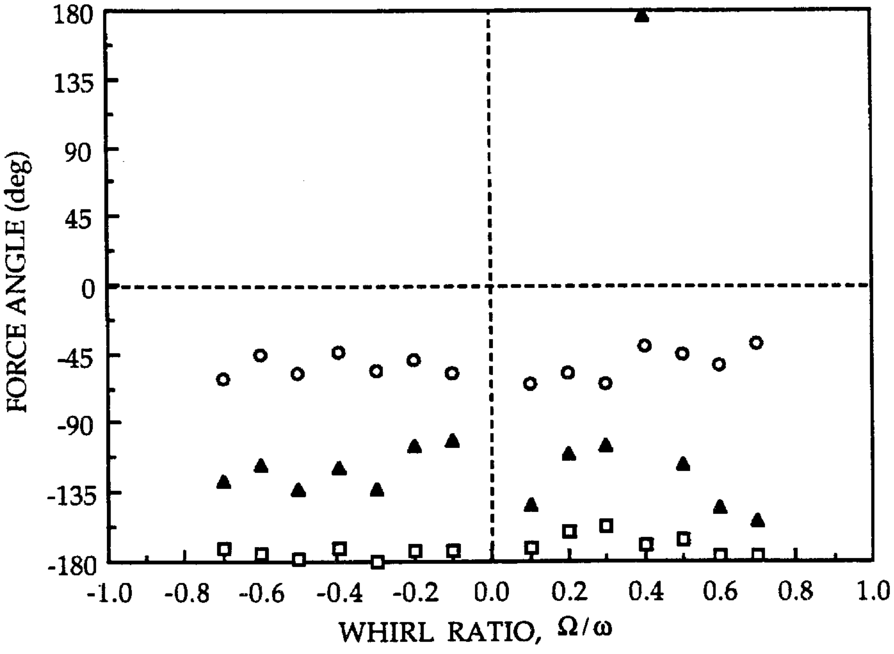

Figure 5.9B. Angle of the lateral force shown in figure 5.9a
(ϕ = 0.074; □ - SC1; ▲ SC2; ○ - no distortions).

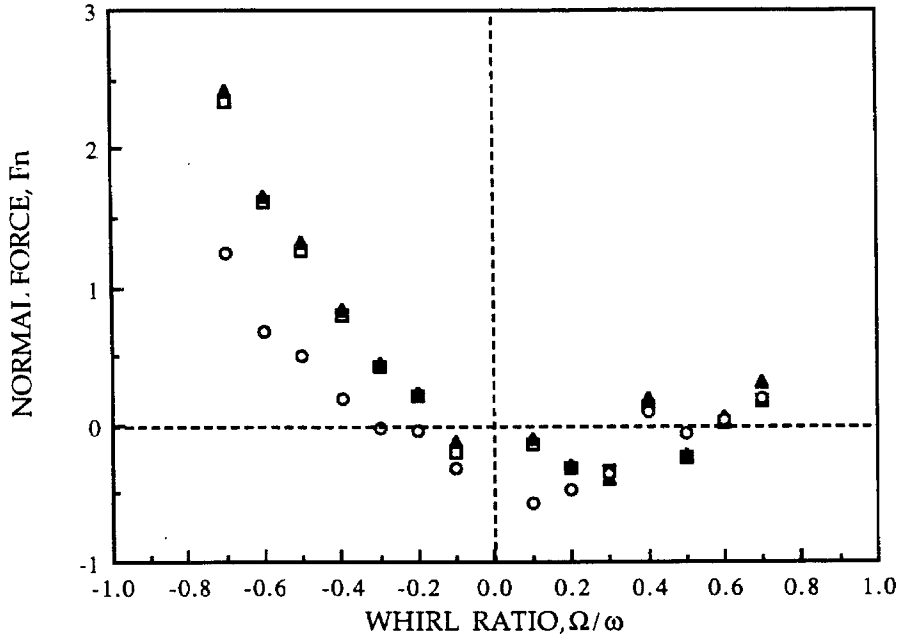

Figure 5.10a. The effect of the inlet distortion screens on the non-dimensionalized normal force on inducer VII (ϕ = 0.074; □ - SC1; ▲ - SC2; ○ - no distortions).

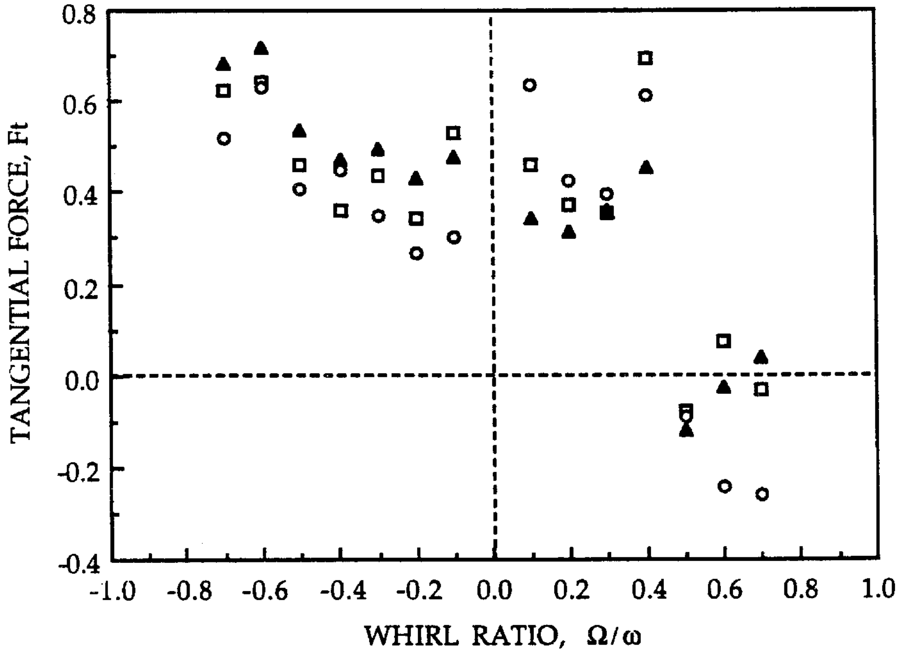

Figure 5.10b. The effect of the inlet distortion screens on the non-dimensionalized tangential force on inducer VII (ϕ = 0.074; □ - SC1; ▲ - SC2; ○ - no distortions).

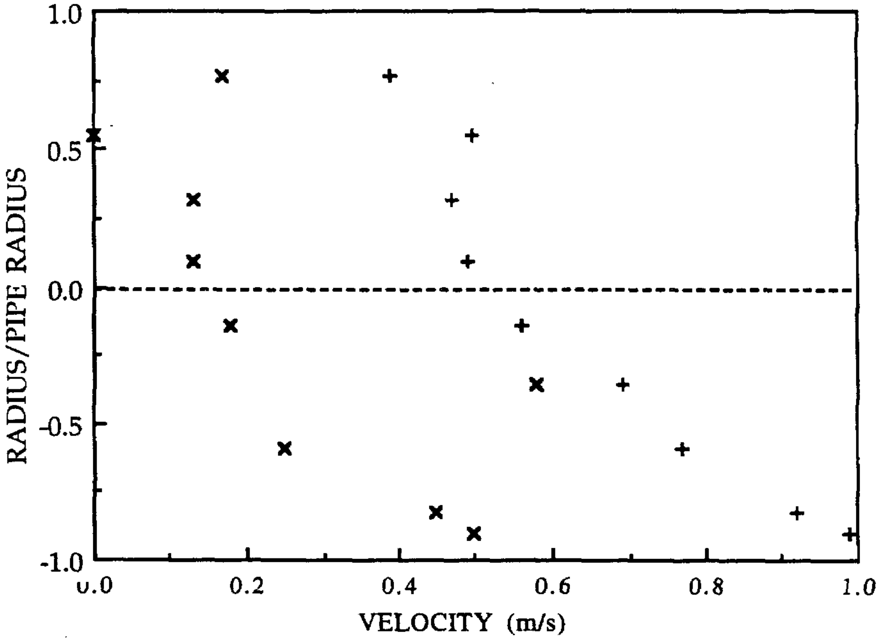

Figure 5.11. Velocity profiles due to upstream bend
(+ - axial; × - swirl).

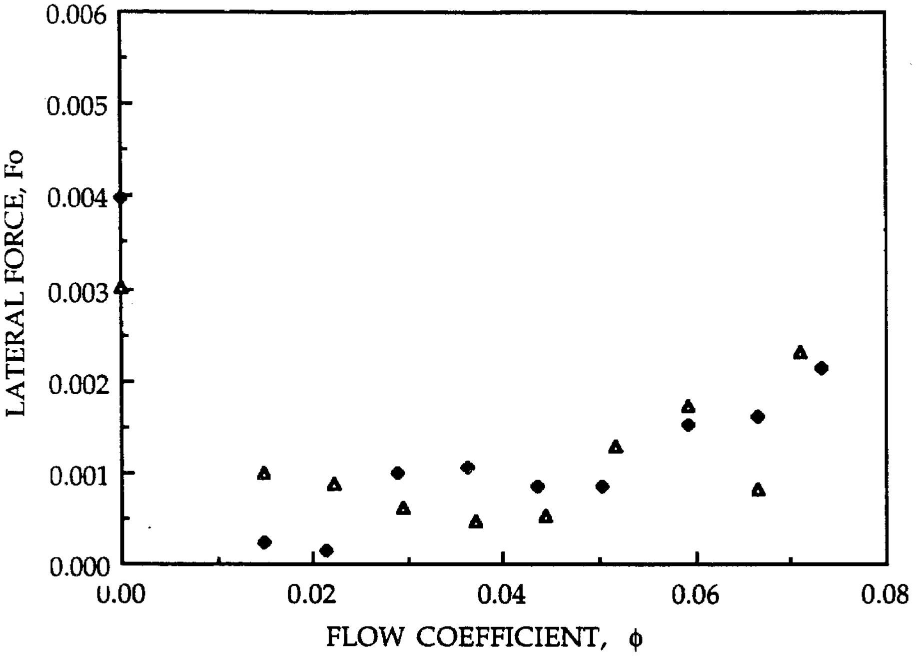

Figure 5.12a. Non-dimensionalized lateral force on inducer VII due to the upstream bend (2000 rpm; ▲ - with upstream bend; ◆ - no distortions).

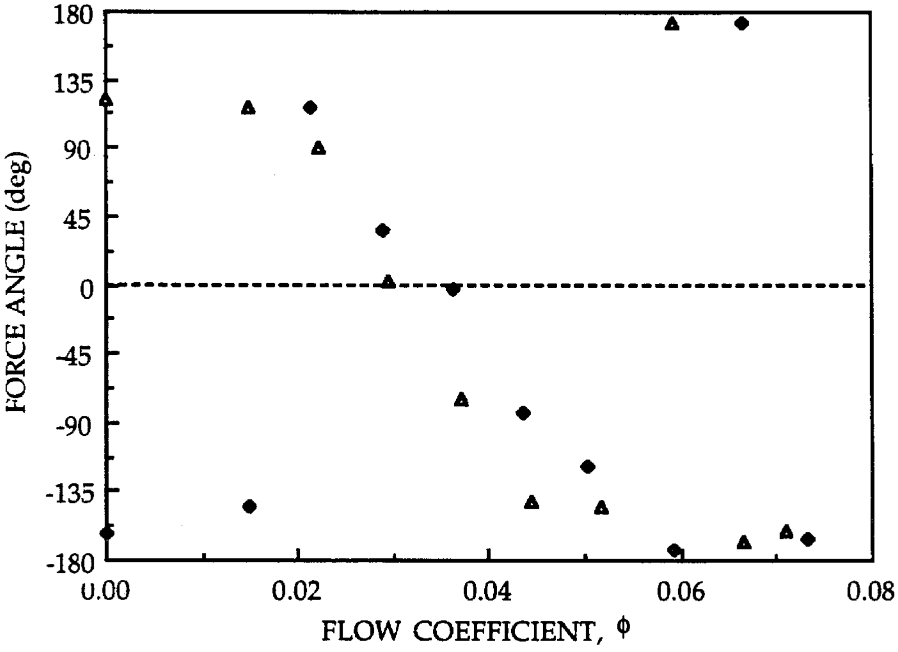

Figure 5.12b. Angle of the lateral forceshown in figure 5.12a (▲ - with upstream bend; ◆ - with no distortions).

CHAPTER 6

CAVITATION EFFECTS ON INDUCER FORCES

Inducers typically operate under cavitating conditions upstream of the main pump and are usually designed to collapse cavitation bubbles in the blade passages. The presence of cavitation bubbles can affect the performance of an inducer and in addition, the growth and collapse of cavitation bubbles can exert significant forces on the inducer. In this chapter, the effects of cavitation on the performance and rotordynamic and lateral forces on inducer VII have been presented.

The effects of cavitation were studied at two flow coefficients, $\phi = 0.074$ and $\phi = 0.049$. The specific flow coefficients were chosen in order to study the effects of flow reversals on the forces and to compare these with the forces at a flow coefficient for which no flow reversals are observed ($\phi = 0.074$). For the set of experiments presented in this chapter, the eccentricity is set at $\varepsilon = 0.0254$ cm. The experiments were conducted at a higher inducer rotational speed of 3000 rpm to achieve the desired level of cavitation than those used for the non-cavitating studies described in chapters 2, 3 and 4. The whirl speed was varied from -0.55 to +0.55 times the shaft speed. The cavitation experiments were conducted without the downstream screen (mentioned in chapter 5).

A conventional cavitation number, σ, is used to define the non-dimensional suction conditions:

$$\sigma = \frac{(p_i - p_v)}{\frac{1}{2}\rho u_2^2}$$

where p_i is the inlet static pressure, p_v is the vapor pressure (at the water temperature) and u_2 is the tip speed of the inducer. The results presented are for various cavitation numbers.

6.1 CAVITATION PERFORMANCE OF INDUCER VII

The cavitation characteristics of inducer VII are shown in figure 6.1 at ϕ = 0.074 and ϕ = 0.049 (3000 rpm). The head coefficient, ψ, defined as the ratio $\Delta p_t/(\rho u_2^2)$ where Δp_t refers to the change in the total pressure, is plotted against various values of σ at non-cavitating and cavitating conditions. In the case of ϕ = 0.074, it is seen that as the cavitation number is reduced from non-cavitating values, the head coefficient started decreasing at $\sigma = 0.147$. However, there was a slight increase in the head coefficient at $\sigma = 0.113$ followed by a continuous head breakdown below $\sigma = 0.106$. The head coefficient is approximately 0.081 under non-cavitating conditions and $\psi = 0.077$ at $\sigma = 0.106$ (which represents a 4.9% head loss). The cavitation characteristics at ϕ= 0.049 exhibit a similar behavior.

6.2 STEADY FORCES DUE TO CAVITATION

The results of the steady radial force measurements at ϕ = 0.074 are presented in figures 6.2a and 6.2b for various whirl/shaft speed ratios (-0.55 to +0.55). The steady forces remain constant for a given cavitation number over the range of whirl/shaft speed ratios, but decrease with cavitation number. It is observed that the non-cavitating steady forces are much larger than the steady forces with cavitation due to the presence of the downstream asymmetry inherent to the system (as explained in chapter 5).

Figure 6.3a shows the variation of the steady force for various whirl ratios at the flow coefficient of $\phi = 0.049$. Figure 6.3b shows the angle at which the lateral force acts. The results differ from those obtained for $\phi = 0.074$ in that *the cavitating forces are about the same magnitude as the non-cavitating forces.*

6.3 ROTORDYNAMIC FORCES DUE TO CAVITATION

The rotordynamic forces on the inducer were also obtained at various flow coefficients and cavitation numbers. The tangential force is plotted against whirl frequency ratio, Ω/ω, for $\phi = 0.074$ in figure 6.4. The significant result obtained is the occurrence of multiple zero crossings. There are some significant differences compared to the non-cavitating forces characteristics. One of these is that the tangential force remains negative in a significant region of negative whirl (it may be recalled that a negative tangential force in the negative whirl region is destabilizing). In fact for $\sigma = 0.106$ and $\phi = 0.074$, the tangential force does not reach a positive value in the negative whirl region (for the range of whirl/shaft speed ratios tested). Another feature of the tangential force is that it exhibits a positive peak in a range of positive whirl frequency ratio around at $\Omega/\omega \approx 0.2$. Such a peak is not observed in the non-cavitating tangential force at this flow coefficient (when there is no backflow). In fact, the magnitude of this peak increases in magnitude as the cavitation number is reduced. The location of the peak also tends to shift to lower whirl/shaft speed ratios. Thus, the extent and the manner in which the tangential forces become destabilizing depend on the extent to which the inducer cavitates. At larger positive whirl frequency ratios (especially for $\Omega/\omega > 0.4$), however, the tangential force is observed to become increasingly negative (and hence stabilizing) for decreasing cavitation numbers. Destabilizing tangential forces are generally observed from $\Omega/\omega = 0.0$ to $\Omega/\omega \approx 0.4$.

Figure 6.5 presents the corresponding results for a flow coefficient $\phi = 0.049$. The variations with whirl frequency ratio are very much similar to those at $\phi = 0.074$, especially in the occurrence of a positive, destabilizing peak around $\Omega/\omega \approx 0.2$. Multiple zero crossings are also evident. However, at this flow coefficient, the tangential force continues to be destabilizing at $\Omega/\omega = 0.55$ for a cavitation number $\sigma = 0.098$ unlike F_t at Ω/ω=0.55 for $\phi = 0.074$ (at the same cavitation number).

Figure 6.6 presents a comparison between the tangential forces at the two flow coefficients for $\sigma = 0.106$. Note that the magnitude of the tangential force clearly increases with a decrease in the flow coefficient. In the region of negative whirl however, the forces become more stabilizing (except for the region between $\Omega/\omega = -0.5$ and $\Omega/\omega \approx -0.3$). The peak in the force in the region of positive whirl increases in magnitude (by approximately 200%). The location of this peak also shifts from $\Omega/\omega = 0.3$ at $\phi = 0.074$ to $\Omega/\omega = 0.2$ at $\phi = 0.049$. Another important observation is that for higher positive whirl ratios ($\Omega/\omega > 0.5$), the tangential forces tend to become increasingly destabilizing for the lower flow coefficient (whereas they become stabilizing for the higher flow coefficient).

Similar data for cavitation number of 0.098 is shown in figure 6.7. Again a positive peak of the tangential force occurs at $\Omega/\omega = 0.3$. For the lower flow coefficient, the range of destabilizing tangential force decreases for negative whirl (approximately $-0.3< \Omega/\omega<-0.1$ at $\phi = 0.049$ compared to approximately $-0.4< \Omega/\omega<0.1$ at $\phi = 0.074$ for $\sigma = 0.098$).

The normal forces on the inducer at the flow coefficient of 0.074 have been plotted for different cavitation numbers in figure 6.8. It is observed that the normal forces do not vary significantly with cavitation number once cavitation has been established. However, compared to the non-cavitating data, large and increasingly positive (destabilizing) normal forces with increasing positive whirl frequency ratios are observed. Furthermore, the normal force in the presence of cavitation tends to be of a larger (negative) magnitude than the non-cavitating normal force for the range of whirl frequency ratios between -0.1 and +0.1. The characteristics of the normal force (with cavitation) in the region of negative whirl ($\Omega/\omega < -0.1$) tends to be similar to the non-cavitating normal force behavior.

Figure 6.9 presents similar data for the lower flow coefficient of 0.049. In this case the normal force behavior displays multiple zero crossings. A significant feature is the occurrence of a negative peak at all the cavitation numbers (including the non-cavitating case). It is also noted that the normal force decreases for $\Omega/\omega < -0.4$ and increases for $\Omega/\omega>+0.4$ with decreasing cavitation number.

The normal forces at a given cavitation number, $\sigma = 0.106$, and two flow coefficients are compared in figure 6.10. As in the case of the tangential forces, a decrease in the flow coefficient clearly causes changes in the normal force. The number of zero crossings increase with a decrease in the flow coefficient and an additional region of positive (destabilizing) force occurs around $\Omega/\omega = 0.1$. Another significant effect caused by decreasing the flow coefficient is the appearance of a negative peak in the normal force in a region of positive whirl; at $\phi = 0.049$, $\sigma = 0.106$ this peak occurs around $\Omega/\omega \approx 0.2$. It is also observed at lower flow coefficient that the normal force tends to remain negative over a longer range of positive whirl frequencies. A comparison similar to that of figure 6.10 is shown in figure 6.11, but at the lower cavitation number $\sigma = 0.098$. An increase in the number of zero crossings of the force is observed at the lower flow coefficient. A positive (destabilizing) peak appears at $\Omega/\omega \approx 0.1$ for the lower flow coefficient at this cavitation number and along with a negative peak at $\Omega/\omega \approx 0.2$.

The results presented in this chapter show that cavitation in an inducer can cause significant rotordynamic forces. The destabilizing rotordynamic effects may lead to failure of the device in which the inducer is being used. It is therefore important to gain a fundamental understanding of the nature of these forces, in order to facilitate changes in the design and/or operating conditions of the machine.

The effect of the geometry of inducers of this type on the cavitation performance have been reported previously (Acosta 1958). The mechanism of head breakdown has also been studied by researchers such as Jakobsen (1964).

The influence of the flow coefficient on non-cavitating steady forces has been reported earlier (chapters 4 and 5). It was shown that the presence of a downstream asymmetry causes significantly large steady forces due to the occurrence of a downstream flow reversal. The downstream reverse flow consists of high energy fluid (on which pumping work has already been done) and the asymmetry causes a net radial force. It was demonstrated that the imposition of a uniform downstream condition (with a perforated screen) led to a near zero lateral force on the inducer (Bhattacharyya et al. 1992). The current experiments with cavitation were conducted with the same downstream asymmetry which is inherent to the system. This is the cause of the large non-cavitating steady force seen in figures 5 and 6. However, it may be noted that the downstream reversal for ϕ = 0.074 is probably only incipient since previous flow visualization on the hub did not reveal re-entry flows on the hub (there was no observable upstream swirling backflow either). Furthermore, the occurrence of cavitation at this higher flow rate actually results in a lower net steady force. It may be speculated that this occurs because of the lower pumping work being done on the fluid because of cavitation. In the case of the lower flow coefficient, the steady force always remains high regardless of the extent of cavitation.

The unsteady force data suggests that flow reversals can also have significant consequences for rotordynamic forces. For non-cavitating flow the tangential forces are higher in magnitude at lower flow coefficients and are destabilizing for positive whirl at both flow coefficients. The non-cavitating tangential force, however shows a destabilizing peak for positive whirl at Ω/ω = +0.1 and a negative peak at Ω/ω = +0.2 for the lower flow coefficient. A similar observation was made on non-cavitating inducers by Arndt and Franz (1986). A more dramatic effect of the flow coefficient is observed in cavitating flow. In the case of the inducer tested, the effect of lowering the flow coefficient increased the region of destabilization (positive F_t) for positive whirl. Furthermore, the effect of a decreased flow did not change the location of the peak, but rather led to an increase in its magnitude. For negative whirl, the higher flow coefficient was more destabilizing. This is an interesting observation especially when the current results are compared to the data obtained previously by Karyeaclis et al. (1989)

on a four-bladed inducer (called the SEP inducer) with a hub which increases substantially between inlet and discharge. In the case of the SEP inducer, the tangential forces were less destabilizing for the lower coefficient for positive whirl frequencies, unlike the current results. Karyeaclis et al. (1989) argued that for a given cavitation number, larger forces could be expected at the higher flow coefficient because it is closer to the performance breakdown point. Those results were based on the limited amount of force data available at that time. The current results do not show the same trend; thus it appears that the *geometry* of the inducer has a significant effect on the rotordynamic forces. Further, the current results show a tangential force peak at $\Omega/\omega = +0.2$ rather than at $\Omega/\omega = +0.5$ observed for the SEP tests. In Karyeaclis et al. (1989) it was argued that the peak at $\Omega/\omega = +0.5$ was a sympathetic resonance with the fluid behind the inducer which rotates at half the shaft speed. In the current tests, however, the peak occurs at much less than half the shaft speed. In the case of the normal forces, the effect of a reduction in the flow coefficient was an increase in the number of positive and negative peaks. These differences in the characteristics of the rotordynamic forces with whirl frequencies under cavitating conditions probably stem from the differences in the internal flows and reverse flow patterns caused by the geometry differences in inducers.

The effect of cavitation on the tangential forces at a given flow coefficient is significant. It is observed that for decreasing cavitation numbers, the magnitude of the peak in the force at $\Omega/\omega = +0.2$ increases and becomes narrower. Thus the range of destabilizing forces decreases. This is the reverse of the trend to that observed by Karyeaclis et al. (1989) for the SEP inducer where larger forces were accompanied by larger instability regions. Also, in the case of the current inducer the tangential forces with increasing cavitation become increasingly stabilizing for negative whirl.

Another important observation is that the data for F_t and F_n as a function of Ω/ω do not exhibit the kind of quadratic functional behavior which is normally assumed in many rotordynamic models. Rather, as has been reported previously (Karyeaclis et al. 1989) much higher order polynomials would be required to approximate the forces. Thus the representation of the components of the rotordynamic matrix $[A]$ (as given in equation 4) does not hold for the cavitating inducer. Consequently, the generalized stiffness, damping and inertia matrices for the inducer cannot be determined. Instead, rotordynamic analysis of the inducer must include fluid-induced forces which are more general functions of the whirl frequency ratio.

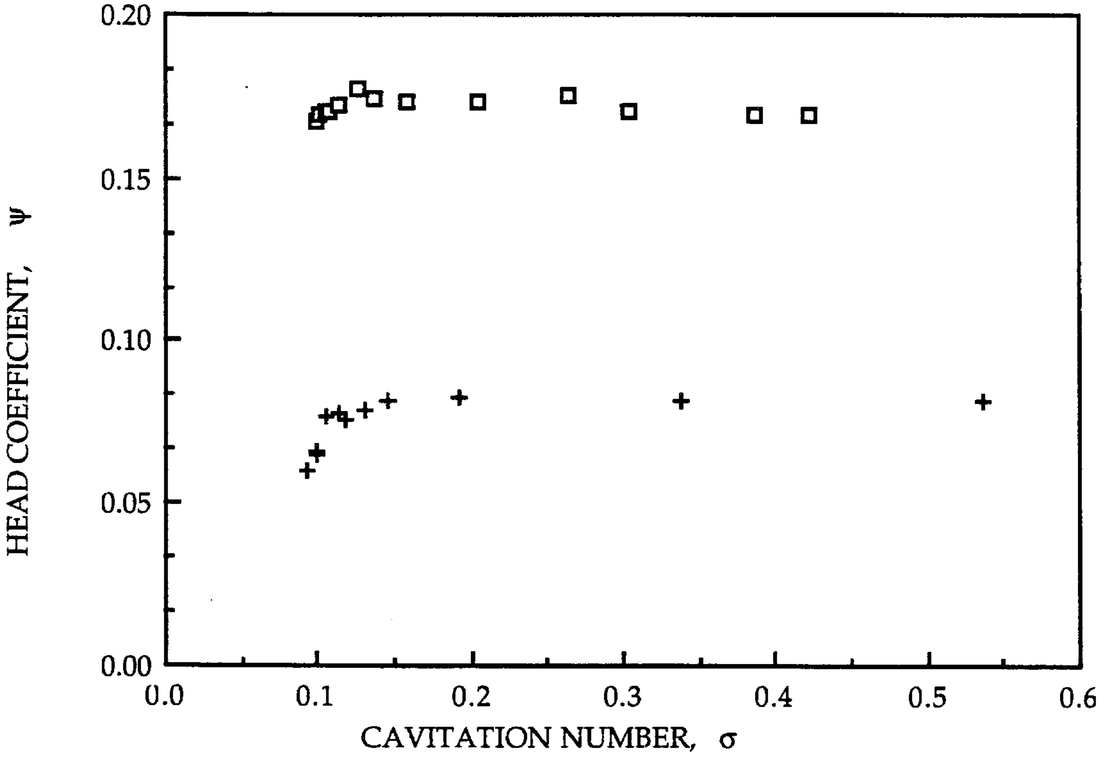

Figure 6.1. Cavitation performance of inducer VII at 3000 rpm (+ ϕ = 0.074; □ ϕ = 0.049).

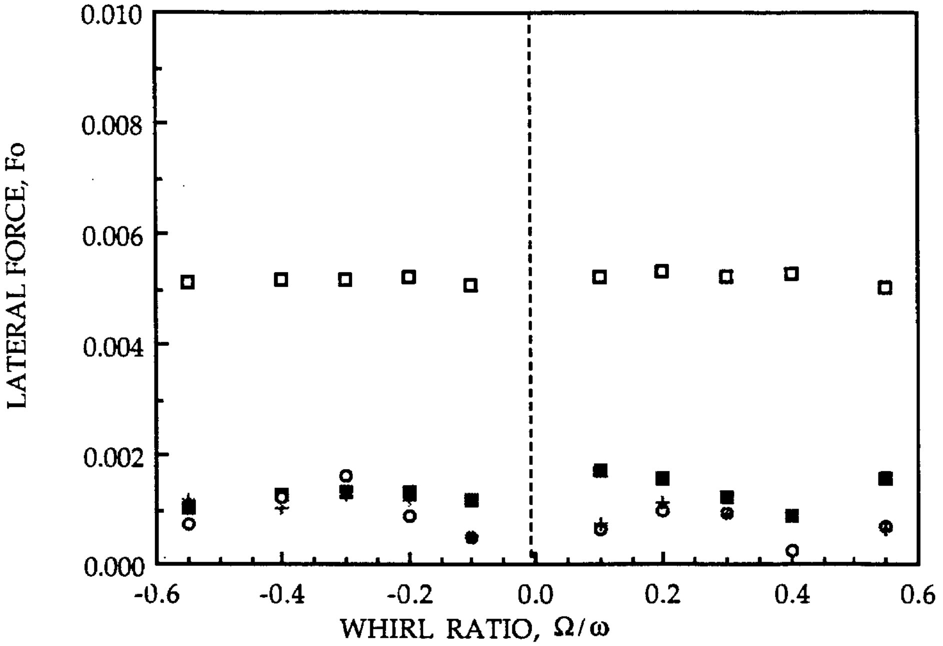

Figure 6.2a. Non-dimensionalized lateral force on inducer VII at a flow coefficient $\phi = 0.074$ for various cavitation numbers (□ - non-cavitating; ■ - $\sigma = 0.106$; ○ - $\sigma = 0.098$; + $\sigma = 0.093$).

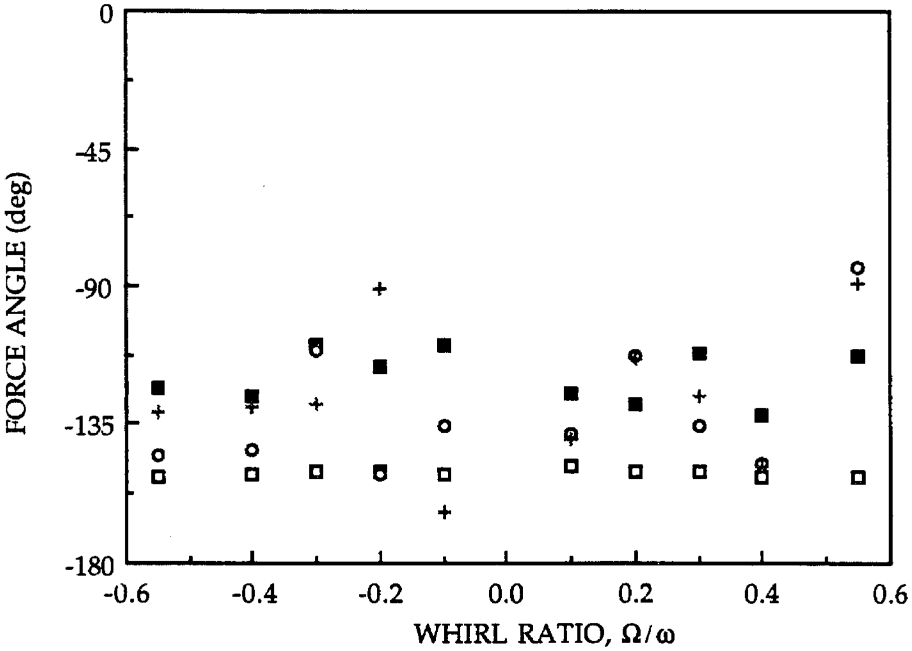

Figure 6.2b. Angle of the lateral force shown in figure 6.2a (□ - non-cavitating; ■ - $\sigma = 0.106$; ○ - $\sigma = 0.098$; + - $\sigma = 0.093$).

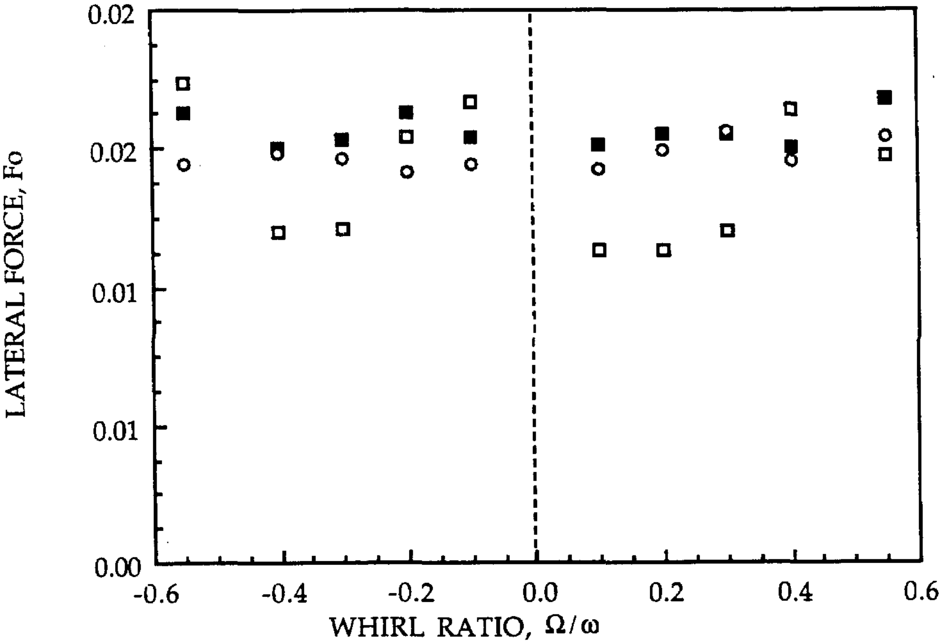

Figure 6.3a. Non-dimensionalized lateral force on inducer VII at a flow coefficient ϕ = 0.049 for various cavitation numbers
(□ - non-cavitating; ■ - $\sigma = 0.106$; ○ - $\sigma = 0.098$).

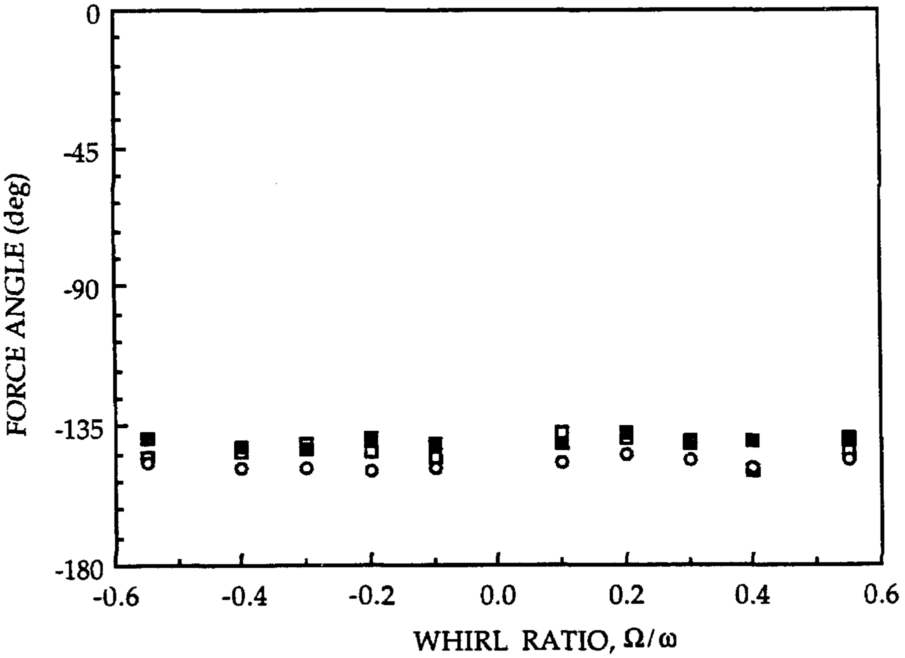

Figure 6.3b. Angle of the lateral force shown in figure 6.3a
(□ - non-cavitating; ■ - $\sigma = 0.106$; ○ - $\sigma = 0.098$).

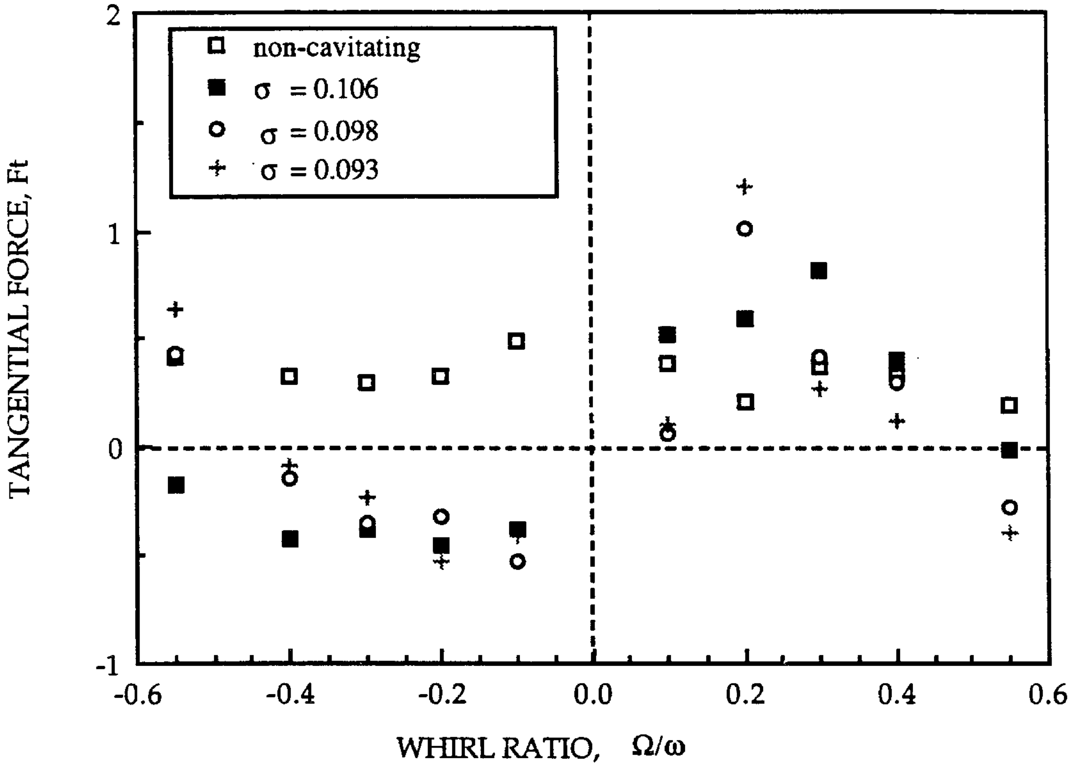

Figure 6.4. Non-dimensionalized tangential force on inducer VII at 3000 rpm and ϕ = 0.074 for various cavitation numbers.

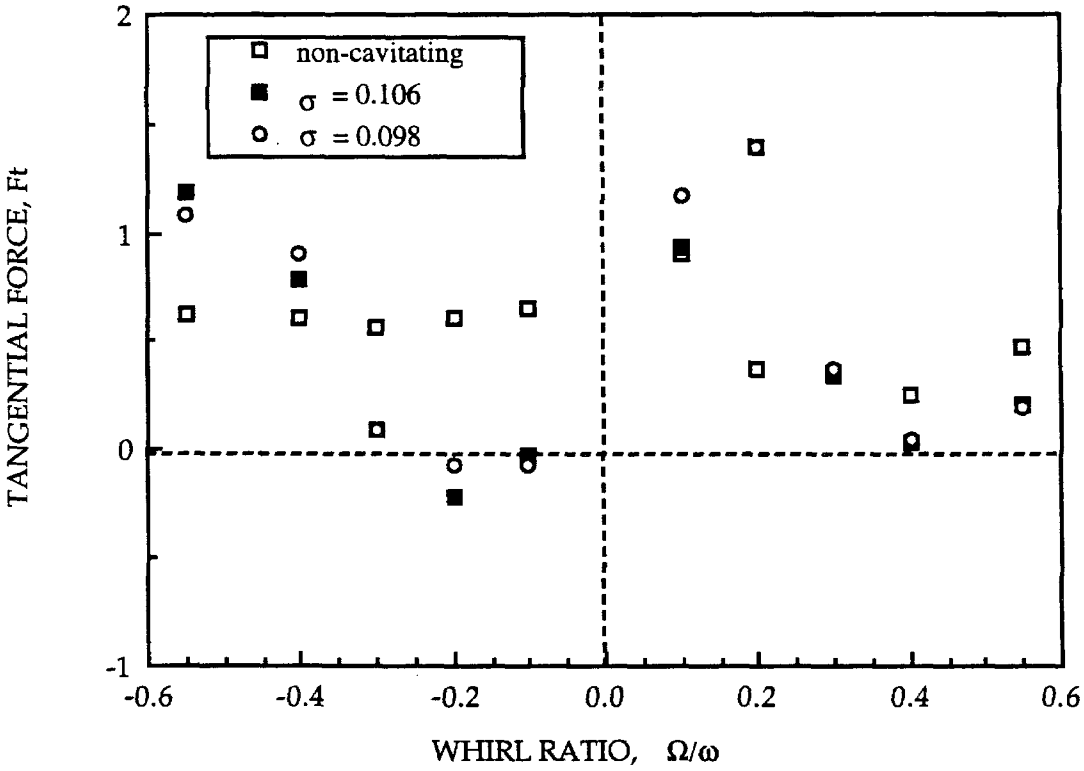

Figure 6.5. Non-dimensionalized tangential force on inducer VII at 3000 rpm and ϕ = 0.049 for various cavitation numbers.

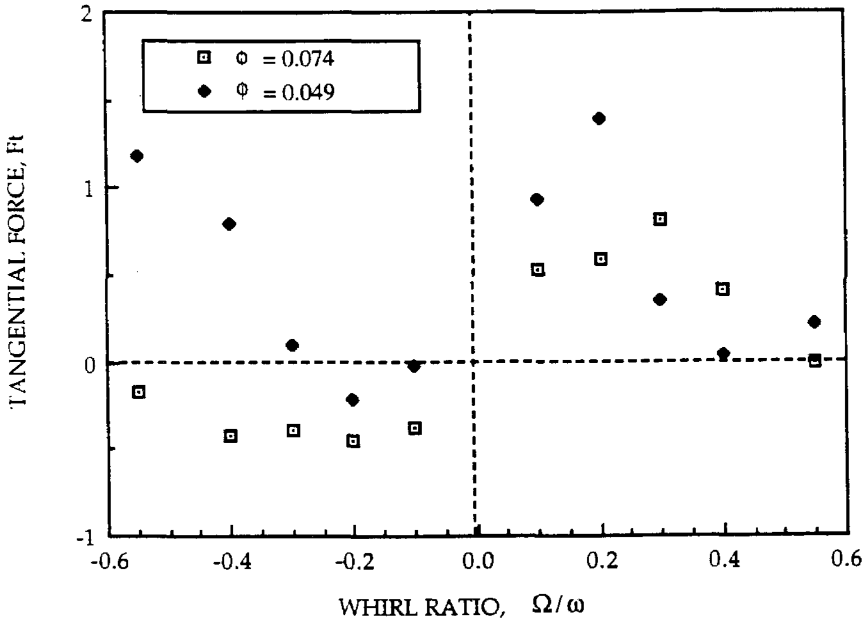

Figure 6.6. Comparison of the non-dimensionalized tangential force on inducer VII at 3000 rpm and cavitation number σ = 0.106 for the two flow coefficients.

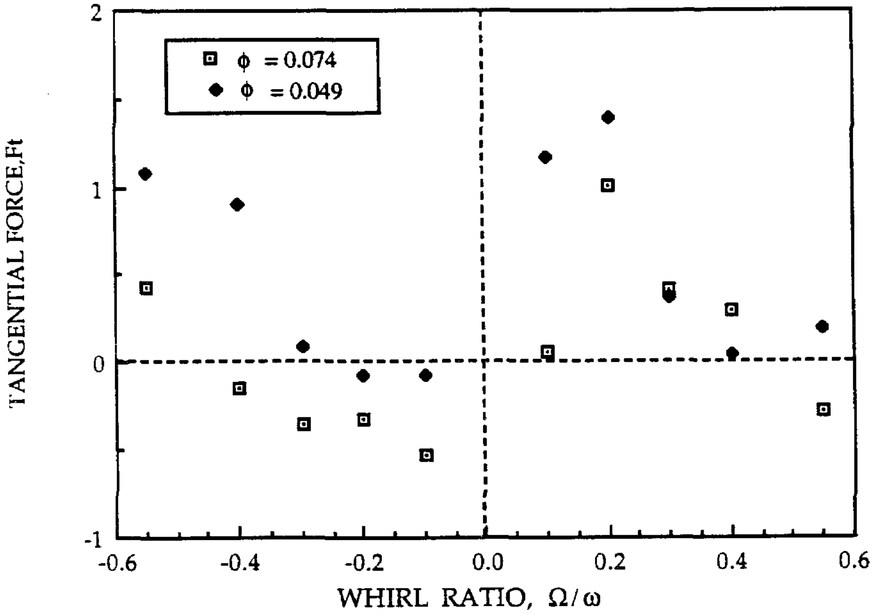

Figure 6.7. Comparison of the non-dimensionalized tangential force on inducer at a cavitation number σ = 0.098 for the two flow coefficients.

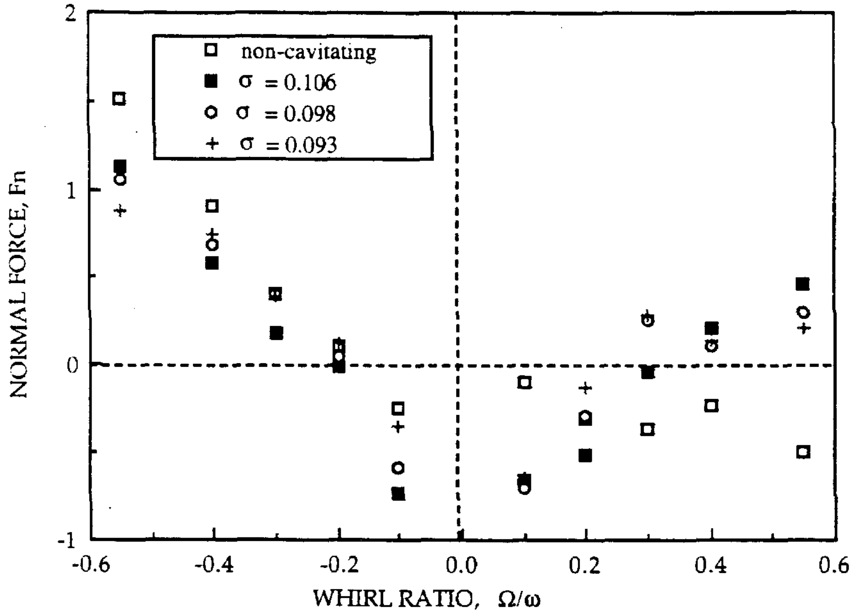

Figure 6.8. Non-dimensionalized normal force on inducer VII at 3000 rpm and ϕ = 0.074 for various cavitation numbers.

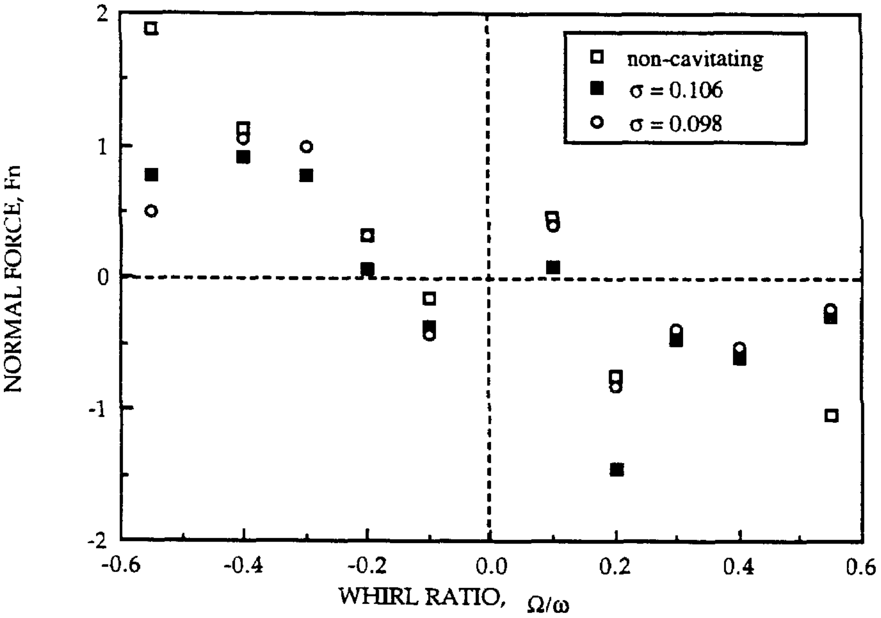

Figure 6.9. Non-dimensionalized normal force on inducer VII at 3000 rpm and ϕ = 0.049 for various cavitation numbers.

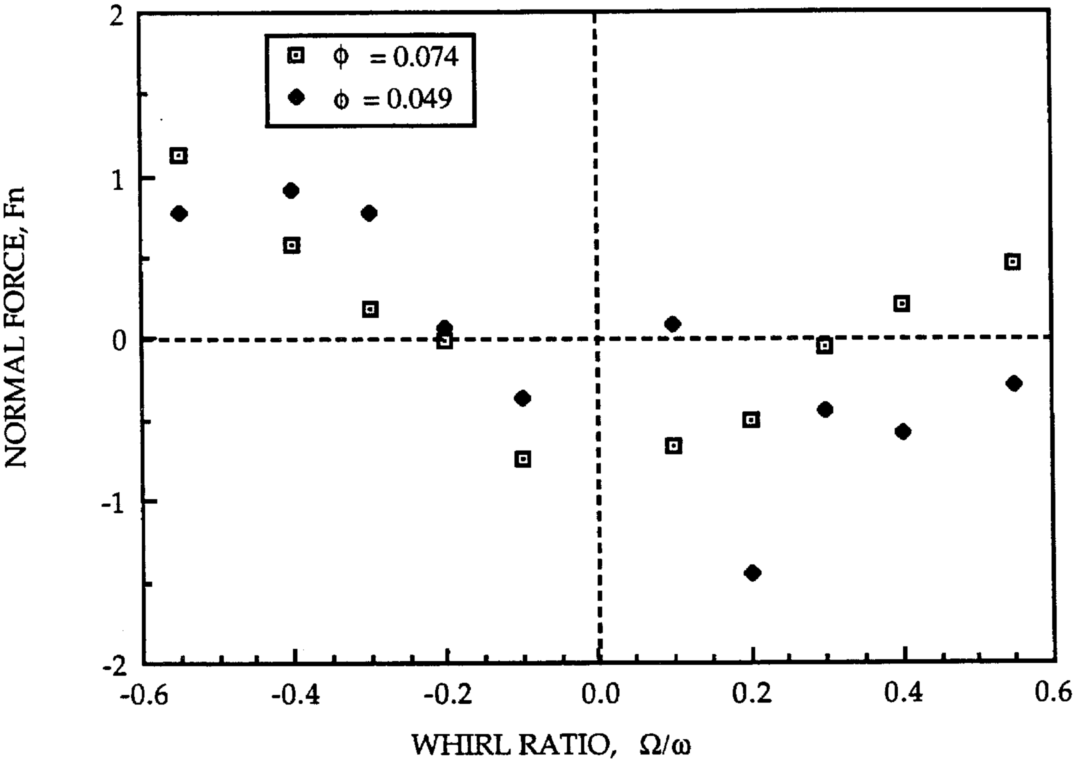

Figure 6.10. Comparison of the non-dimensionalized normal force at 3000 rpm and $\sigma = 0.106$ for the two flow coefficients.

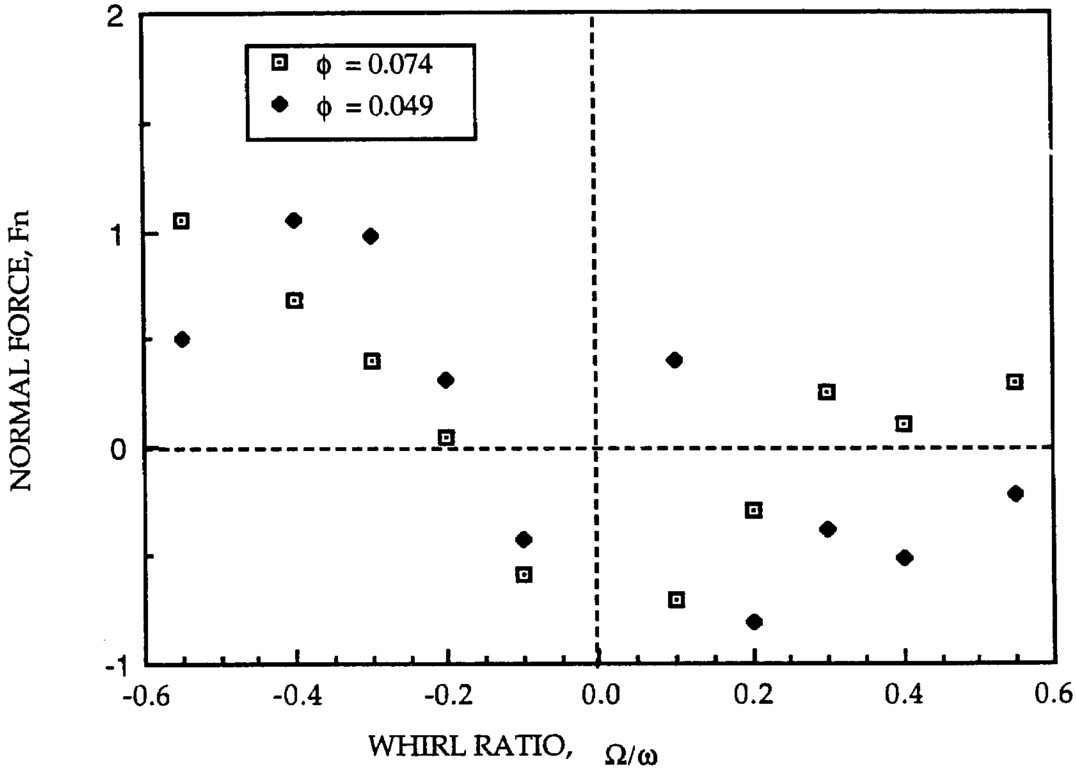

Figure 6.11. Comparison of the non-dimensionalized normal force at 3000 rpm and number $\sigma = 0.098$ for various flow coefficients.

CHAPTER 7

CONCLUSIONS

The internal flows and flow reversals have been studied in non-cavitating axial flow unshrouded and shrouded inducers using flow visualization techniques. In particular, the paint dot method proved to be an effective means for studying boundary layer flows on the blades, hub and housing. The results confirm the complexity and three-dimensionality of flows in these devices. The boundary layer flows on both the suction and the pressure sides of the blades show strong radial components of flow at flow coefficients below design. The flow in the blade boundary layer remains attached to the blade surface for unshrouded inducers at all flow coefficients tested. The boundary layer flow on the leading edge is found to be almost parallel to the leading edge itself at flow coefficients well below design. Limiting streamline angles are high near the leading edge. These angles are also high near the hub especially near the trailing edge and is accompanied by flow reversal downstream on the hub. These angles decrease close to the blade tip upon interaction with the annulus wall for unshrouded inducers and due to the shroud for shrouded inducers. It is also observed that the downstream hub re-entrant flow interacts with the upstream fluid in the blade passage area (at about mid-chord) which leads to separation of the flow and may give rise to vortices in the axial and tangential directions.

The origin of the upstream swirling backflow is at the discharge plane of the inducer for unshrouded inducers. As the experiments with the tufts confirm, the tip clearance leakage flow contributes to the upstream whirling backflow. For unshrouded inducers the radially outward flow near the blade tip mixes with the leakage flow and moves upstream. The location downstream where the hub re-entry flow originates could not be determined. The downstream re-entry flow is associated with very strong radial components of the flow on the trailing edge blade surfaces near the hub. No radially inward flows were observed at the off-design flows on the blade surfaces for both unshrouded and shrouded inducers.

The discharge-to-suction leakage exterior to the shroud for shrouded inducers originates at the downstream end of the rotating shroud. Flow reversal also occurs at the tip near the leading edge, and together with the leakage flow, constitutes the upstream backflow. In shrouded inducers, large radial blade boundary layer flows on the suction side occur near the hub close to the trailing edge along with re-entry of the hub boundary layer flow into the blade passage area at off-design conditions, similar to unshrouded inducers.

The fluid-induced forces on inducers were also measured under varying conditions of flow and whirl. It may be concluded from the results of the flow distortion experiments that downstream flow asymmetries cause a significant increase on inducer lateral forces on flow coefficients below design. The downstream re-entrant flow on the hub consists of high energy fluid. An asymmetric distribution of this reverse flow causes large lateral forces on the inducer.

An inlet disturbance of a strong shear flow can cause an increase in the magnitude of the lateral force on an inducer. However, relatively weak shear flows do not have a significant impact on these forces. A 180° bend placed more than four inducer diameters upstream also does not cause a significant lateral force on the inducer. Both upstream and downstream flow distortions do not cause any significant changes in the magnitude of the rotordynamic (normal and tangential) forces for various whirl frequency ratios.

The non-cavitating rotordynamic forces in an inducer are characterized by multiple zero crossings of the forces with whirl frequency ratio and by the occurrence of large destabilizing peaks at low flow coefficients. The rotordynamic forces do not exhibit a quadratic functional behavior and hence the conventional generalized stiffness, damping and inertia matrices cannot be determined. The theoretical estimation of the tangential force using actuator disk theory (Colding-Jorgensen 1992) were applied to predict the force on a non-whirling inducer (appendix B), and the results show that the predicted forces were significantly different, both in magnitude and direction, from the experimentally measured forces. Theoretical estimates of rotordynamic forces (such as the results of the actuator disk model) are as yet inadequate in accurately predicting these forces.

Cavitation has important consequences for fluid-induced rotordynamic forces generated by inducers. These forces can become destabilizing at both positive and negative whirl frequencies. With increasing levels of cavitation (i.e., lower cavitation numbers) the magnitudes of the destabilizing peaks increase. The internal flow patterns and flow reversals associated with reduced flow coefficients appear to have a significant bearing on these forces. The flow patterns are, in turn, dependent on the inducer geometry and the dependence of the forces on the extent of cavitation must be included in design considerations.

REFERENCES

Acosta, A.J., 1958. An Experimental Study of Cavitating Inducers. *Proceedings of 2nd Symposium on Naval Hydrodynamics,* Washington D.C., pp. 533-557.

Acosta, A.J., 1992. Flow in Inducer Pumps, An Aperçu. *Proceedings of the Fourth international Symposium on Transport Phenomena and Dynamics of Rotating Machinery,* Honolulu, Vol. A., pp. 1-13.

Adkins, D.R., and Brennen, C.E., 1988. Analyses of Hydrodynamic Radial Forces on Centrifugal Pump Impellers. *ASME J. Fluids Eng.,* Vol. 110, no. 1, pp. 20-28.

Agostinelli, A., Nobles D., and Mockridge, C.R., 1960. An Experimental Investigation of Radial Thrust in Centrifugal Pumps. *ASME J. Eng. for Power,* Vol. 82, pp. 120-126.

Alford, J.S., 1965. Protecting turbomachinery from Self-Excited Rotor Whirl. *ASME J. Eng. for Power,* Vol. 87, pp. 333-344.

Arndt, N., and Franz, R., 1986. Observations of Hydrodynamic Forces on Several Inducers Including the SSME LPOTP. *Calif. Inst. of Tech., Div. of Eng. and Appl. Sci., Report No. E249.3.*

Bhattacharyya, A., 1991. The Effect of Inlet Flow Modification on the Lateral Forces on an Inducer. *Proc. of the First ASME-JSME Fluids Eng. Conf.,* Portland, Oregon, June 23-27, 1991. FED-Vol. 119, pp. 31-34.

Bhattacharyya, A., Acosta, A.J., Brennen, C.E., and Caughey, T.K., 1992. The Formation of Backflow and its Consequences for Lateral Forces in Axial Flow Pump Impellers. *Abstracts of the ASME Fluids Engineering Conference,* R. Bajura, ed., Los Angeles, FED-Vol. 133, pp. 237-239.

Bhattacharyya, A., Acosta, A.J., Brennen, C.E., and Caughey, T.K., 1993. Observations on Off-Design Flows in Non-Cavitating Axial Flow Inducers. *Proc. of the Pumping Mach. Symp. at the ASME Fluids Eng. Conf.*, Washington D.C., June 20-24, 1993. FED-Vol. 154, pp. 135-141.

Biheller, H.J., 1965. Radial Force on the Impeller of Centrifugal Pumps with Volute, Semi-volute and Fully Concentric Casings. *ASME J. Eng. for Power,* July 1965, pp. 319-323.

Boccazzi, A., Perdichizzi, A., and Tabacco, U., 1990. Flow Field Investigation in a Low-Solidity Inducer by Laser-Doppler Velocimetry. *ASME J. of Turbomachinery,* Vol. 112, pp. 91-97.

Brennen, C.E., Acosta, A.J., and Caughey, T.K., 1986. Impeller Fluid Forces. *Proc. NASA Advanced Earth-to-Orbit Propulsion Technology Conference, Huntsville, AL, NASA Conf. Publ. 2436,* pp. 270-295.

Brennen, C.E., 1994. Hydrodynamics of Pumps. (To be published).

Chamieh, D.S., 1983. Forces on a Whirling Centrifugal Pump Impeller. *Ph.D. Thesis, Calif. Inst. of Tech., and Div. of Eng. and Appl. Sci. Report No. E249.2.*

Chamieh, D.S., Acosta, A.J., Brennen, C.E., and Caughey, T.K., 1985. Experimental Measurements of Hydrodynamic Radial Forces and Stiffness Matrices for a Centrifugal Pump-Impeller. *ASME J. of Fluids Eng.,* Vol. 107, no. 3, pp. 307-315.

Del Valle, J., Braisted, D.M., Brennen, C.E., 1990. The Effects of Inlet Flow Modification on Cavitating Inducer Performance. *Calif. Inst. of Tech., Div. of Eng. and Appl. Sci. Report No. E249.10.*

Del Valle, J., Braisted, D., M., and Brennen, C., E., 1991. The Effects of Inlet Flow Modification on Cavitating Inducer Performance. ASME *Journal of Turbomachinery,* Vol.114, pp.360-365.

Domm, H. and Hergt, P., 1970. Radial Forces on Impeller of Volute Casing Pumps. *Flow Research on Blading,* Dzung L.S. ed., Elsevier Publ. Co., The Netherlands, pp. 305-321.

Ehrich, F., 1957. Circumferential Inlet Distortions in Axial Flow Turbomachinery. *J. of the Aero. Sci.,* June, 1957, pp. 413-417.

Ehrich, F., and Childs, D., 1984. Self-Excited Vibration in High Performance Turbomachinery. *Mech. Eng.,* Vol. 106, no. 5, pp. 66-79.

Franz, R., and Arndt, N., 1986. Measurements of Hydrodynamic Forces on the Impeller of the HPTOP of the SSME. *Calif. Inst. of Tech., Div. of Eng. and Appl. Sci. Report No. E249.*

Franz, R., 1989. Experimental Investigation of the Effect of Cavitation on the Rotordynamic Forces on a Whirling Centrifugal Pump Impeller. *Ph.D. Thesis, Calif. Inst. of Tech., and Div. of Eng. and Appl. Sci. Report No. E249.8.*

Franz, R., Acosta, A.J., Brennen, C.E., and Caughey, T.K., 1989. The Rotordynamic Forces on a Centrifugal Pump Impeller in the Presence of Cavitation. *Proc. ASME Symp. Pumping Machinery,* FED-81, pp. 205-212.

Franz, R., Acosta, A.J., Brennen, C.E., and Caughey, T.K., 1989. The Rotordynamic Forces on a Centrifugal Pump Impeller in the Presence of Cavitation. *ASME J. Fluids Eng.,* Vol. 112, pp. 264-271.

Guinzburg, A., Brennen, C.E., Acosta, A.J., and Caughey, T.K., 1990. Measurements of Rotordynamic Shroud Forces on Centrifugal Pumps. *Proc. ASME Turbomachinery Forum,* FED-96, pp. 23-26.

Guinzburg, A., 1992. Rotordynamic Forces Generated by Discharge-To-Suction Leakage Flows in Centrifugal Pumps. *Ph.D. Thesis, Calif. Inst. of Tech., and Div. of Eng. and Appl. Sci. Report No. E249.14.*

Hergt, P. and Krieger, P. 1969. Radial Forces in Centrifugal Pumps with Guide Vanes. Proc. Inst. Mech Eng., Vol. 184, Part 3N, pp. 101-107.

Horlock, J.H., 1978. Actuator Disk Theory. McGraw-Hill.

Horlock, J.H., and Greitzer, E.M., 1983. Non Uniform Flows in Axial Compressors Due to Tip Clearance Variation. *Proc. Inst. of Mech. Eng.*, Vol. 1976. I. Mech. E. Sept. 1983.

Howard, J.H.G., Tropea, C., Almahroos, H.M.H., and Roeber, T.W., 1987, *Proceedings of the ASME-JSME Thermal Engineering Joint Conference*, P.J. Marto and I. Tanasawa, ed., Honolulu, Vol. 2, pp. 63-69.

Howard, J.H.G., Hutchinson B.R., and Broberg R.B., 1993. Flow Analysis in a Spiral Inducer Impeller. *Int. Turbine and Aeroengine Congress and Exposition*, 93-GT227, Cincinnati, Ohio, May 24-27, 1993.

Howard, J.H.G., and Atif A., 1993. Near-exit Flow Field Investigation in an Inducer including Laser-Doppler Velocimetry. *Int. J. Heat and Fluid Flow*, Vol. 14, No.1, March 1993.

Iverson, H.W., Rolling, R.E., and Carlson, J.J. 1960. Volute Pressure Distribution, Radial Force on the Impeller and Volute Mixing Losses of a Radial Flow Centrifugal Pump. ASME Journal of Engineering for Power, Vol. 82, No. 2, pp. 136-144.

Jakobsen, J.K., 1964. On the Mechanism of Head Breakdown in Cavitating Inducers. ASME *J. of Basic Eng.*, June 1964, pp. 291-305.

Jakobsen, J.K., 1971. Liquid Rocket Engine Turbopump Inducers. NASA Space Vehicle Design Criteria (Chemical Propulsion), R.B. Keller, ed., NASA SP-8052.

Janigro, A., and Ferrini, F., 1973. Recent Progress in Pump Research. VKI Lecture Series - 61, J. Chauvin, ed., von Karman Institute for Fluid Dynamics, Rhode-Saint-Genése, Belgium.

Jery, B., 1986. Experimental Study of Unsteady Hydrodynamic Force Matrices on Whirling Centrifugal Pump Impellers. *Ph.D. Thesis, Calif. Inst. of Tech.*

Kamijo, K.,, Shimura T., Watanabe M., 1977. An Experimental Investigation of Cavitating Inducer Instability. *Proc. of the ASME Winter Annual Meeting* , Atlanta, Georgia, 1977.

Karyeaclis, M.P., Miskovish, R.S., and Brennen, C.E., 1989. Rotordynamic Tests in Cavitation of the SEP Inducer. *Calif. Inst. of Tech., Div. of Eng. and Appl. Sci. Report no. E200.27.*

Katz, R., 1958. Performance of Axial Compressors with Asymmetric Inlet Flows. *Ph.D. Thesis, Calif. Inst. of Tech.*

Lakshminarayana, B., 1972. Visualization Study of Flow in Axial Flow Inducer. ASME *Journal of Basic Engineering*, pp. 777-787.

Lakshminarayana, B., 1978. On the Shear Pumping Effect in Rocket Pump Inducers. *Pumps,, Analysis, Design and Application*, Worthington Pump Inc., Polytechnic Institute of New York, pp. 49-68.

Lakshminarayana, B., 1982. Fluid Dynamics of Inducers - A Review. ASME *Journal of Fluids Engineering*, Vol. 104, pp. 411-427.

Rosenmann, W., 1965. Experimental Investigations of Hydrodynamically induced Shaft Forces With a Three Bladed Inducer. *Proc. ASME Symp. on Cavitation in Turbomachinery*, pp. 172-195.

Ross, C.C., and Banerian, G., 1956. Some Aspects of High-Suction-Specific-Speed Pump Inducers. Trans. ASME 78:1715 (1956).

Stepanoff, A.J., 1955. Turboblowers - Theory, Design, and Application of Centrifugal and Axial Flow Compressors and Fans. John Wiley and Sons, Inc., New York.

Tanaka, T., 1980. An Experimental Study of Backflow Phenomena in High Specific Speed Propeller Pump. *ASME paper* 80-FE-6.

Taylor, G.I., and Batchelor, G.K., 1949. The Effect of Wire Gauze on Small Disturbances in a Uniform Screen. *Quart. J. Mech. Appl. Math.*Vol 2, No.1.

Thomas, J.J., 1958. Instabile Eigenschwingungen von Turbinenlaufern angefacht durch die Spaltströmungen Stopfbüschen und Beschaufelungen, AEG Sonderdruck.

Toyokura, T., Kubota, N., 1965. Studies on the Improvement of High-Specific-Speed Pump Performance at Low Flow Rates. *Bulletin of JSME,* Vol.8, No.29, pp.78-88.

Toyokura, T., Kubota, N., 1968. Studies on Back-Flow Mechanism of Turbomachines: Part 1, Back-Flow Mechanism to the Suction Side of Axial-Flow Impeller Blades. *Bulletin of JSME,* Vol.11, No.43, pp.147-156.

Vance, J.M., 1988. Rotordynamics of Turbomachinery. John Wiley & Sons, Inc.

Vance, J.M., and Laudadio, F.J., 1982. Experimental Measurement of Alford's Force in Axial-Flow Turbomachinery, Rotordynamic Instability Problems of High Performance Turbomachinery. *NASA Conf. Publ. 2250,* pp. 260-273.

Vance, J.M., and Laudadio, F.J., 1984. Experimental Measurement of Alfords Force in Axial Flow Turbomachinery. *ASME IGTI Paper No. 1984-GT-140.*

Zhuang F., 1989. Experimental Investigation of the Hydrodynamic Forces on the Shroud of a Centrifugal Pump Impeller. *Calif. Inst. of Tech., Div. of Eng. and Appl. Sci. Report No. E249.9.*

APPENDIX A

THEORY FOR THE GENERATION OF SHEAR FLOW

A potential flow theory was used to design a screen which would generate a uniform shear flow. The shear flow was used to study flow distortion effects detailed in chapter 5. A modified version of the theory by Owen and Zienkiewicz (1957) for the production of shear flow in a wind tunnel was used. The theory is presented in this appendix.

Figure A.1 shows a flow through a screen which contains a distribution of holes such that a linear shear flow is obtained downstream of the screen. The velocity far upstream is assumed to be uniform and equal to V. *The flow profile* created by the screen is linear and given by:

$$v(y) = V + \lambda''(y-D_p/2) \qquad \text{(A.1)}$$

where v(y) is the axial velocity at a location (y) downstream of the screen, λ'' is a constant which determines the slope of the linear shear and D_p is the pipe diameter. The coordinate system is shown in figure A.1. The problem is solved as a two-dimensional one, by assuming a rectangular channel (of height D_p). It is also assumed that $\lambda'' D_p/V$ is so small that the departure of any streamline from a straight line is correspondingly small. A stream function can then be written as:

$$\begin{aligned} \Psi &= Vy + \Psi' && \text{for } x<0, \\ &= Vy + \frac{1}{2}\lambda''\left(y^2 - D_p y\right) + \Psi' && \text{for } x>0 \qquad \text{(A.2)} \end{aligned}$$

where Ψ' which is everywhere small compared to VD_p and tend to zero as $x \rightarrow \pm\infty$, satisfies $\nabla\Psi' = 0$. The boundary conditions for the problem are:

$$\frac{\partial\Psi'(x,0)}{\partial x} = \frac{\partial\Psi'(x,D_p)}{\partial x} = 0. \tag{A.3}$$

The solutions satisfying these boundary conditions are for all x are:

$$\frac{\Psi'}{VD_p} = \sum_{n=1}^{\infty} A_n e^{n\pi x/D_p} \sin\left(n\pi y / D_p\right) \qquad \text{for } x<0,$$

$$= \sum_{n=1}^{\infty} B_n e^{-n\pi x/D_p} \sin\left(n\pi y / D_p\right) \qquad \text{for } x>0. \tag{A.4}$$

(n is an integer: 1,2...)

The presence of the screen requires that (i) $\partial\Psi / \partial y$ is continuous through x=0, (ii) the velocity component $\partial\Psi / \partial x$ obeys a certain refraction condition across x=0, and (iii) the difference between the total pressures on a given streamline for large positive and negative values of x must be equal to the resistance per unit area imposed by the screen (Owen and Zienkiewicz 1957). In addition, the static pressures far upstream and downstream of the screen are assumed to be independent of y. From condition (i), the following relationship is obtained:

$$A_n - B_n = C_n \lambda D_p / V, \tag{A.5}$$

$$\text{where } \frac{1}{2} y(y - D_p) = D_p^2 \sum_{n=1}^{\infty} C_n \sin\left(n\pi y / D_p\right).$$

Due to the condition (ii), it is assumed that the y component of velocity changes by a factor α' in passing through the screen. Taylor and Batchelor (1949) showed that, for a uniform grid, this factor (α') is $1.1(1+K')^{-1/2}$ where K' is the resistance coefficient. For the purpose of the present analysis, the resistance of the screen is assumed to be graded slightly, so that α' may be considered to be the same value as that given by Taylor and Batchelor (1949). Therefore, if the resistance grading of the screen is represented by $K'=K_o[1+\varepsilon'(y)]$, such that ε' is small and $\int_0^{D_p} \varepsilon' \, dy = 0$,

$$\alpha' = \frac{1.1}{(1+K_o)^{1/2}} \left[1 - \frac{K_o \varepsilon'}{2(1+K_o)} \right] + O(\varepsilon'^2). \qquad (A.6)$$

The refraction condition (ii) can then be written as:

$$\sum_{n=1}^{\infty} nB_n \sin(n\pi y / D_p) + (a + b\varepsilon') \sum_{n=1}^{\infty} nA_n \sin(n\pi y / D_p) = 0,$$

and since A_n and B_n are $O(\lambda'' D_p / V)$, this reduces to:

$$B_n + aA_n = O(\lambda'' D_p \varepsilon' / V) \qquad (A.7)$$

where $a = 1.1(1+K_o)^{-1/2}$.

The total pressure drop at the screen may be expressed as:

$$p_u + \frac{1}{2}\rho V^2 - p_d - \frac{1}{2}\rho \left[V + \lambda'' \left(y_d - \frac{1}{2} D_p \right) \right]^2 = K' \frac{1}{2} \rho [v(0)]^2, \qquad (A.8)$$

where p_u and p_d are the static pressures far upstream and far downstream of the screen, and y_d is an ordinate downstream of a streamline which meets the screen at y_u. The relationship between the streamline ordinates follows from equation (A.2) as:

$$y_d = y_u + \Psi'(0, y_u)/V + O(\lambda'' \Psi' / V^2).$$

(A.9)

This implies that to the first-order in $\lambda''D_p/V$ and Ψ'/VD_p the x component of the velocity at the screen is given by:

$$v(0) = V + \lambda''\left(y_u - \frac{1}{2}D_p\right) + \frac{\partial\Psi'(0,y_u)}{\partial y}. \tag{A.10}$$

When equation (A.10) is combined with equation (A.8) we get:

$$\frac{p_u - p_d}{\frac{1}{2}\rho V^2} = K_o(1+\varepsilon') + 2\frac{\lambda''D_p}{V}(1+K_o)\left(\frac{y_u}{D_p} - \frac{1}{2}\right) + \frac{2K_o}{V}\frac{\partial\Psi'(0,y_u)}{\partial y}. \tag{A.11}$$

Since (p_u - p_d) is independent of y, the equation (A.11) can be resolved as:

$$\frac{p_u - p_d}{\frac{1}{2}\rho V^2} = K_o \tag{A.12}$$

and $$K_o\varepsilon' + 2\frac{\lambda''D_p}{V}(1+K_o)\left(\frac{y_u}{D_p} - \frac{1}{2}\right) + 2\frac{K_o}{V}\frac{\partial\Psi'(0,y_u)}{\partial y} = 0. \tag{A.13}$$

Equations (A.4), (A.5), and (A.7) yield:

$$\frac{\partial\Psi'(0,y_u)}{\partial y} = -\pi\lambda''D_p\frac{a}{(1+a)}\sum_{n=1}^{\infty} nC_n\cos\left(n\pi y / D_p\right) = -\lambda''D_p\frac{a}{(1+a)}\left(\frac{y_u}{D_p} - \frac{1}{2}\right). \tag{A.14}$$

It follows from equation (A.13) that:

$$\varepsilon'(y_u) = -2\frac{\lambda''D_p}{V}\left(\frac{1}{K_o} + \frac{1}{(1+a)}\right)\left(\frac{y_u}{D_p} - \frac{1}{2}\right). \tag{A.15}$$

The resistance distribution of the screen can therefore be obtained from equation (A.15).

It is now necessary to obtain a relationship between the hole spacing distribution of the screen and the resistance distribution in order to obtain a physically realizable screen. This is achieved by the following consideration.

Consider a two-dimensional flow through a screen with one small opening in a pipe flow as shown in figure A.2. The drag force (D_f) on the screen is then evaluated and the drag coefficient C_d is then obtained as:

$$C_d = \frac{D_f}{\frac{\rho}{2}V_j^2\left(A - A_j\right)} = \left(1 - \frac{A_j}{A}\right), \qquad \text{(A.16)}$$

where V_j is the flow velocity at the opening and A and A_j are the cross-sectional *areas of the pipe and opening respectively.* Since the total pressure gradient across the screen and the drag force are related as $\Delta p_t + D_f = 0$ *and since the* resistance of the screen is given by $K' = \frac{\Delta p_t}{\frac{\rho}{2}V^2}$, we finally obtain

$$K' = C_d \frac{\xi'}{(1-\xi')^2}, \qquad \text{(A.17)}$$

where ξ' is the fractional blockage area $(A-A_j)/A$. From equation (A.16), the drag coefficient can also be expressed in terms of the blockage as: $C_d = \xi'$. Therefore, we use the following equation to obtain a distribution of the blockage area (and hence a distribution of hole diameters) for a screen (to generate a linear shear flow of specified slope):

$$\frac{\xi'^2}{(1-\xi')^2} = K_o\left[1 - 2\frac{\lambda'' D_p}{V}\left(\frac{1}{K_o} + \frac{1}{(1+a)}\right)\left(\frac{y_u}{D_p} - \frac{1}{2}\right)\right] \qquad \text{(A.18)}$$

and the hole radii (R)are expressed in terms of the blockage as:

$$R'(y)=\sqrt{\frac{A}{\pi}\left[1-\xi'(y)\right]}. \qquad (A.19)$$

A screen with a distribution of holes (with varying radii along y) can thus be obtained to generate a linear shear flow. For the current experiments, two screens were used. Screen SC1 was designed with $K_o = 10.0$ and $\lambda'' D_p/V = 1.55$ and screen SC2 was designed with $K_o = 5.0$ and $\lambda'' D_p/V = 1.0$. As demonstrated by the results presented in chapter 5, this method turned out to be effective in generating such shear flows.

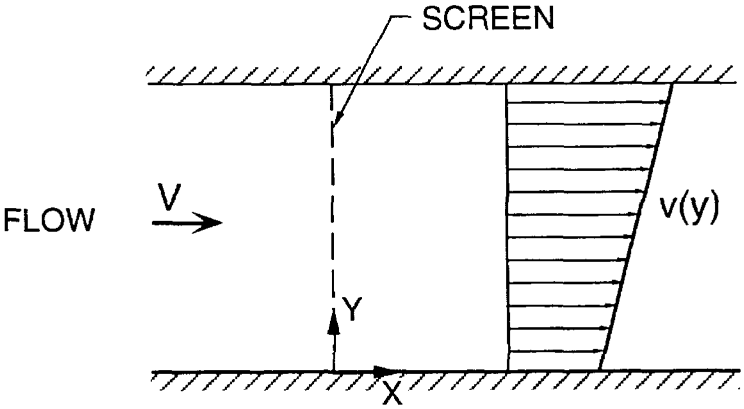

Figure A.1 Flow through a screen designed to produce a linear shear flow.

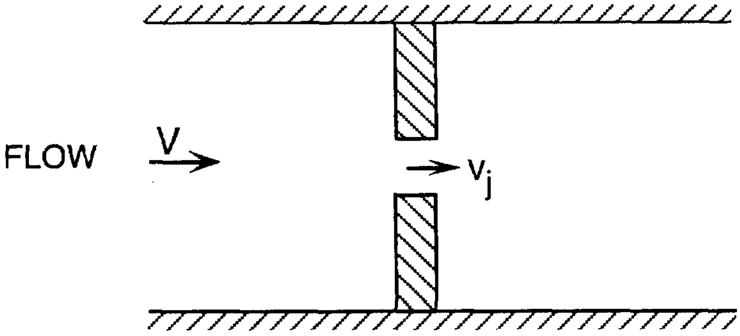

Figure A.2 Two dimensional flow through a screen with one opening in a pipe.

APPENDIX B

THEORETICAL CONSIDERATIONS

B.1. A SIMPLE HYDRAULIC CALCULATION

As a preliminary estimate of the net tangential force on an inducer, a simple hydraulic calculation is performed. This exercise would indicate the extent to which such a calculation succeeds in making an estimate of the tangential force. The calculation is performed on an inducer with a fixed eccentricity and no whirl. The net tangential force can then be evaluated by integrating the force on a single blade at a certain radius (r), over the rotor and the blade height as:

$$F_t = \int_{r_1}^{r_2} \int_{0}^{2\pi} \rho c_x \left(-c_x \tan \beta_2\right) \cos\theta r dr d\theta \tag{B.1}$$

where r_1, r_2 represent the hub and tip radii of the blade respectively, the term in parenthesis in the integrand ($-c_x \tan\beta_2$) represents the net change in the relative tangential velocity across the blade. c_x is the axial velocity and β_2 is the angle made by the relative velocity vector with the axial direction. θ is the angle over which the force is integrated around the rotor. The tangential velocity at the inlet is assumed to be zero. In the absence of inlet distortions, the axial velocity at the inlet can be expressed as a quadratic function of the radius (r') as:

$$c_x(r') = a - b\,(r'/R_p)^2 \tag{B.2}$$

where a, b are constants and R_p is the pipe radius at the inlet. The constants 'a' and 'b' obtained from the experimental measurement of the inlet velocity profile.

The radius (r') may be expressed in terms of the rotor blade radius (r), noting that the rotor is offset by the eccentricity (ε) from geometry:

$$r'^2 = r^2 + \varepsilon^2 + 2\, r\, \varepsilon \cos(\theta) \tag{B.3}$$

Substitution of equation (B.3) into (B.2) would give an expression for the axial velocity in terms of the blade radius (r). The integral in equation (B.1) can then be evaluated to obtain:

$$F_t = \rho \tan(\beta_2)(C - B) \tag{B.4}$$

$$\text{where } B = \frac{4b^2}{R_p^4}\left[\frac{\pi\varepsilon^3}{3}\left(r_2^3 - r_1^3\right) + \frac{\pi\varepsilon}{5}\left(r_2^5 - r_1^5\right)\right] \text{ and } C = \frac{4\pi ab\varepsilon}{R_p^2}\,\frac{\left(r_2^3 - r_1^3\right)}{3} \tag{B.5}$$

A comparison of this result with the experimentally measured tangential force is made for the following case:

$\beta_2 = 81^\circ$ (i.e. inducer VII); $\phi = 0.074$; $a = 0.77036$; $b = 0.40257$; $r_1 = 0.0202$ m; $r_2 = 0.0506$ m; $R_p = 0.0584$ m; $\varepsilon = 2.54$ e -04.

The tangential force on the rotor is then obtained and normalized in the manner described earlier. The normalized force is obtained as: $F_t = 0.0257$. The experimentally measured normalized force (obtained from chapter 4) was found to be: $F_t = 0.469$.

Thus it is seen that the force obtained from the hydraulic calculation predicts a force in the same direction as the measured force (i.e. both positive), but significantly underestimates the magnitude of the actual force. The measured *tangential force is about 25 times larger than the predicted tangential force.* The difference is probably due to neglecting the effects of flow redistribution along the azimuthal direction and blade span, static pressure distribution in the azimuthal direction, and internal and secondary flow effects.

B.2. ESTIMATION OF TANGENTIAL FORCE USING ACTUATOR DISK THEORY

The tangential force on an offset inducer (no whirl) is also estimated using the actuator disk theory of Colding-Jorgensen (1992). The details of the theory were presented in chapter 1. In this section, the final result of the theory will be applied to the case of inducer VII to estimate the tangential force as a function of flow coefficient at 2000 rpm

The actuator disk theory established the non-dimensionalized cross-coupled stiffness coefficient (and the tangential force) as a function of flow coefficient and blade angles. The theory was developed for an axial flow compressor, but can also be applied to estimate the tangential force on an inducer, noting that the compressibility term (Q_1) in equation 1.35 can be substituted by the product of the efficiency and the Euler work (equation 1.28). In the case of an inducer, the circumferential velocity at the inlet may assumed to be zero (when there is no upstream swirl component or backflow). The blade angle is substituted as $\beta_2 = -81^0$ in the sense used by Colding-Jorgensen (1992). The tangential force as obtained by the theory (section 1.4.1b) is given by:

$$F_T = \frac{\lambda\pi\varepsilon}{\bar{\eta}}\rho l u_2^2 r_2 \sin\beta_2\left[1+\phi^2\left(1+2\tan^2\beta_2\right)+\phi\left(3\tan\beta_2+\cot\beta_2\right)\right] \tag{B.6}$$

This theoretical tangential force is normalized in the same manner as the experimental data presented in chapter 4 and plotted against the flow coefficient at 2000 rpm for inducer VII in figure B.1. For the purposes of this calculation, the value of the efficiency (derived from the performance curve, figure 5.2) is substituted for each flow coefficient. The parameter λ. can be non-dimensionalized as $\lambda^*=\lambda.r_2$. Thus, $\lambda^* = \partial\eta / \partial\left(\frac{\delta}{r_2}\right)$. Typically, $\lambda^* \approx 1$ (Stepanoff 1955). It may be pointed out that $\lambda=2$ as suggested by Colding-Jorgensen (1992) for compressors is misleading since λ is a dimensional quantity. Hence, the value of λ. for the current calculations is assumed to be $1/r_2$. Figure B.1 shows the theoretically estimated force and compares it with the experimental data obtained from the current research. The graph (figure B.1) shows the range of flow coefficients over which the normalized tangential force is predicted to remain positive (i.e., in the direction of inducer rotation). The experimental values of the tangential force for no whirl were obtained by linear interpolation of the data presented in figures 4.2 and 4.4 for $\Omega/\omega = 0.0$. The experimental results show that the tangential force remains positive for all flow coefficients tested (in the range $\phi = 0.0$ to $\phi = 0.074$). The theoretical tangential force, however, is negative over the tested range of flow coefficients. The magnitudes of the measured forces are also significantly larger. For example, the theoretically estimated force at $\phi = 0.074$ is $F_t = -0.0399$ and the experimentally measured value is $F_t = 0.469$ (which is about 12 times larger than the theoretically estimated force). The maximum value of the force predicted by the theory is $F_t \approx 0.2$, which is the same order of magnitude as the measured forces.

There could be several reasons for the discrepancy between the experimental and measured values of the tangential force at the flow coefficients tested. Application of the theory must allow for blockage effects which make the actual flow coefficient higher than the measured value; doing so would shift the value of ϕ to the right (figure B.1) and would hence change the magnitude and direction of the predicted force. It would also be more appropriate to evaluate the forces at the root mean square radius rather than the tip radius, in order to obtain a better estimate of the forces. Further, at flow coefficients below design, there are significant effects of upstream backflow which cause a large swirl component at the inlet, thereby making it necessary to use an inlet velocity angle $\bar{\alpha}_1 \neq 0$. The theory does not take into account the effects of the flow across the entire blade span and the asymmetries of the static pressure distribution in the azimuthal direction. Internal flow effects and the flow in the tip clearance region have also been neglected. In terms of the maximum tangential force predicted, the order of magnitude of the estimated force is the same as that of the experimentally measured force.

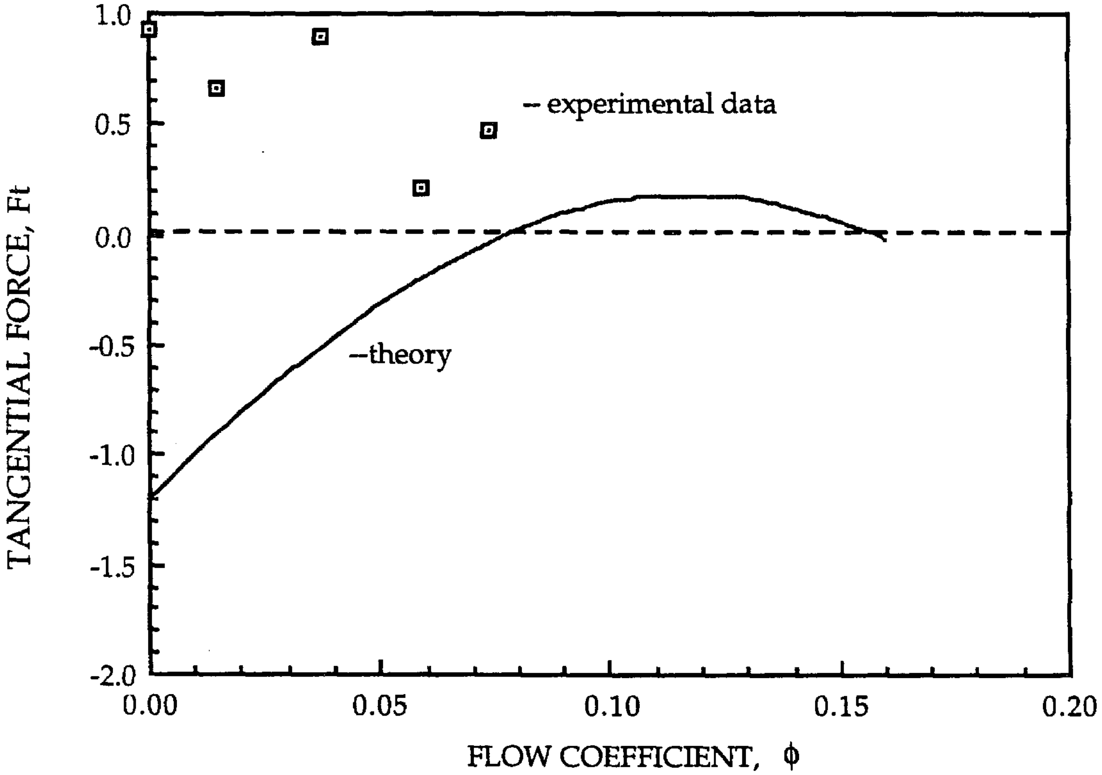

Figure B.1. Comparison of the normalized tangential force as a function of flow coefficient between experiment and actuator disk theory (from Colding-Jorgensen 1992) for inducer VII.

APPENDIX C

STATIC PRESSURE DISTRIBUTION DUE TO DOWNSTREAM ASYMMETRY

It was shown in chapter 5 that a downstream system asymmetry causes a significant lateral force on the inducer, especially at low flow coefficients. The imposition of a uniform downstream condition (due to the screen with 30 percent opening) had significantly reduced these forces. In this appendix, the static pressure distribution on the stationary housing of inducer VII are presented. Measurements were made at various circumferential locations, approximately one half inducer diameter downstream. The static pressures were made using $^1/_8$ inch pressure taps that were connected to a rack of manometers (using water as the manometric liquid). The measurements were made at six circumferential locations, at 60 degree intervals starting from the 30 degree position (using the horizontal X axis as reference; as shown in figure 1.1). The measurements were taken with a zero eccentricity of the rotor at a rotational speed of 2000 rpm.

The results of the static pressure measurements are presented in figures C.1a and C.1b. The pressures are presented using the pressure tap at the 30 degree position as a reference and have been non-dimensionalized by ρu_2^2. Figure C.1a shows that in the presence of the downstream asymmetry, there is a significant variation of the static pressure, especially near the 270 degree position. In addition, the magnitudes of the pressure variation are larger at low flow coefficients, especially at $\phi = 0.015$. Thus the results show a highly asymmetric distribution of static pressure on the housing, as can be expected to occur due to the downstream asymmetry. Upon installation of the downstream screen a more uniform static pressure distribution results. These results are shown in figure C.1b. It is also observed from these figures that the occurrence of the downstream re-entry flow is associated with a significant variation of the downstream static pressures on the housing.

The pressure data presented in figures C.1a and C.1b can be integrated using a discrete Fourier transform in order to obtain a net lateral force on the inducer. The normalized lateral force obtained upon performing such an integration of the static pressures is presented in figure C.2. The figure shows an increase in the lateral force at low flow coefficients in the presence of the downstream asymmetry. However, when compared to the results presented in chapter 5, the magnitude of the peak force measured by the dynamometer is an order of magnitude higher than the force obtained from the static pressure distributions. Also, the peak magnitude of the lateral force (from static pressure measurements) is obtained at a flow coefficient lower than the flow coefficient of the peak lateral force obtained by the dynamometer measurements. These discrepancies between the dynamometer force measurements and the forces obtained by static pressure measurements are probably due to effects of internal flows in the blade passages. Further, the axial variation of the static pressures and blockage effects have not been taken into account in the calculation of the force from the static pressure measurements. These results demonstrate the importance of internal flows and flow reversal effects on the lateral force acting on an inducer.

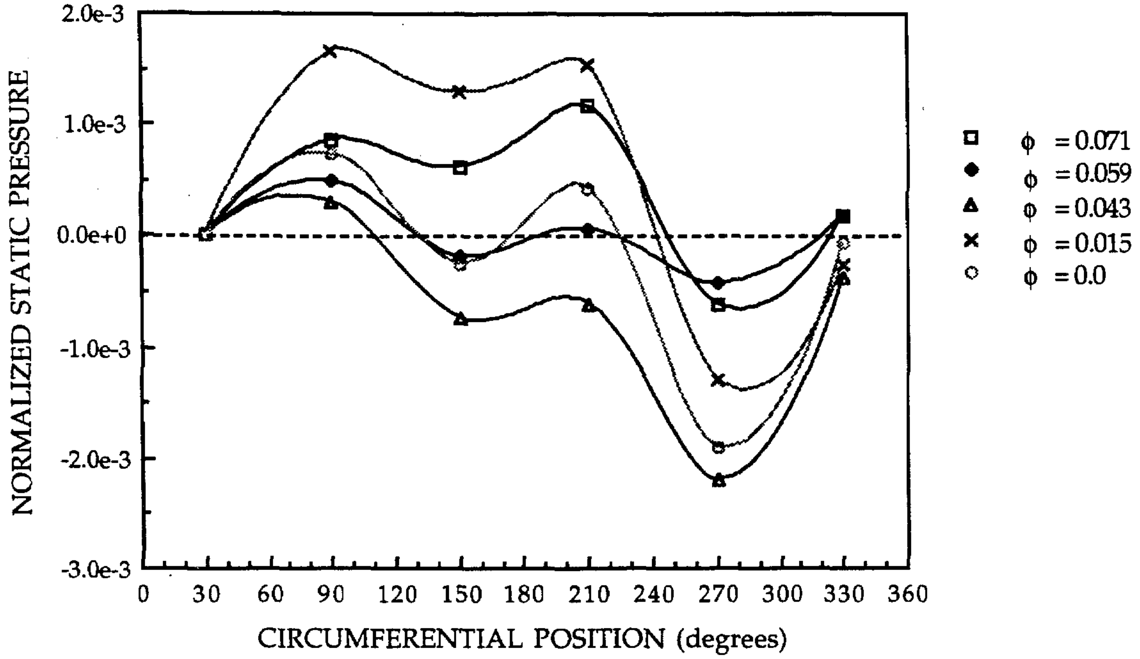

Figure C.1a. The variation of the non-dimensionalized downstream static pressure on the housing of inducer VII in the presence of downstream system asymmetry (measured relative to the 30 deg. position at 2000 rpm).

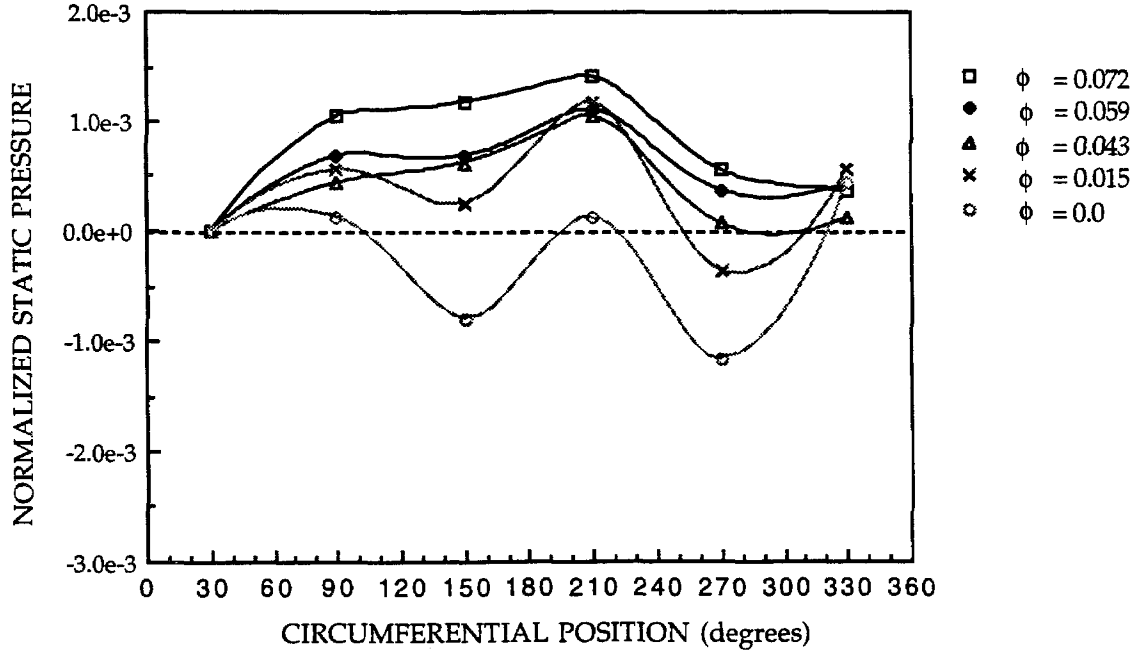

Figure C.1b. The variation of non-dimensionalized downstream static pressure on the housing of inducer VII with the downstream screen installed (measured relative to the 30 deg. position at 2000 rpm).

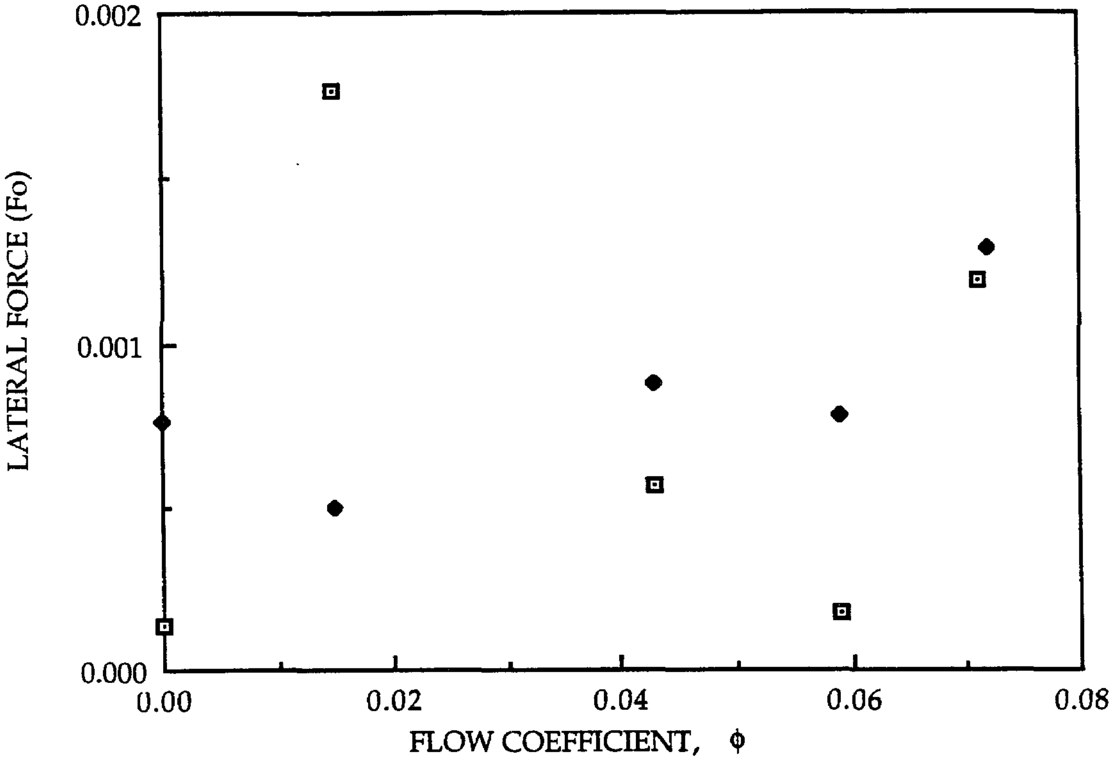

Figure C.2. Comparison of the normalized lateral force on inducer VII at 2000 rpm due to the downstream asymmetry and due to the downstream screen, as obtained from the static pressures of figure C.1 (▣ - with downstream asymmetry; ◆ - with downstream screen).